POLITECNICO DI MILANO

School of Industrial Engineering and Information

Master of Science in Material Engineering and Nanotechnology

Modified Bombyx mori silk fibers characterization

Advisor: **Prof. Pasquale Vena**

Advisor: **Prof. Matteo Tommasini**

Assistant supervisor: **Prof. Siew Lok Toh**

Graduation thesis of:

Marco Rudilosso ID N° 802401

Academic Year 2013/2014

Acknowledgments:

I WANT TO THANK TO MY FAMILY THAT SUPPORTED ME IN ALL OF MY CHOICES.

MY TUTOR PROFESSOR PASQUALE VENA WHO GAVE ME THE OPPORTUNITY

TO GO TO SINGAPORE AND GAVE ME ALL THE SUPPORT I NEEDED.

I THANK PROFESSOR SIEW LOK TOH , FROM NATIONIONAL UNIVERSITY OF SINGAPORE,

WHO GAVE ME THE POSSIBILITY TO SPEND A PERIOD IN HIS TISSUE REPAIR LAB.

SPECIAL THANKS TO ALBERTO CORRIAS, NOT ONLY A GOOD MENTOR IN SINGAPORE

BUT ALSO A VERY GOOD FRIEND.

MY BEST FLATMATE KERSTIN WHICH WHOM I SHARED UNFORGETTABLE EXPERIENCE.

SPECIAL THANKS TO TWO SPECIAL GERMAN FRIENDS, STEFFEN AND DOMINIK

WHICH WHOM I SHARED MOST DANGEROUS AND FUNNY MOMENTS IN SINGAPORE.

SPECIAL THANKS TO ALL MY COLLEAGUES FROM POLITECNICO, ESPECIALLY:

ANTONIO (NAMED BOSS) AND VALERIO SQUARE (NAMED BOSS) BEST SICILIAN FRIENDS.

GOTTE, WHICH WHOM I SHARED ALL MY STUDY LIFE AND THE PASSION FOR EXCIMER LASER.

PHRA, FILIPPO, NICHOLAS, MILENA, LUDOVICO, BEST CLASSMATES AND FRIENDS

OF LAST TWO YEARS.

MARCO

MODIFIED BOMBYX MORI SILK FIBERS CHARACTERIZATION

ABSTRACT

In this work a physical, chemical and mechanical characterization of silk fibers has been carried out with particular regards to the effect of doping on the secondary structure. In particular, three different doping agent were used, respectively I_2, $CaCl_2$ and KBr. FTIR and XRD analyses have shown that doping decreases crystallinity fraction and crystal size in silk fibers; this has been attributed to partial degradation of β-sheets and transformation to amorphous random coil structures. A qualitative ionic conductivity model was proposed to justify increase of current flowing in iodinated fibers under the effect of temperature and relative humidity. Increase in toughness and decrease in maximum strength as obtained through uniaxial tensile tests support assumptions on structural change of silk fibroin after the treatments. Thermal degradation of doped samples respect to unmodified one was studied by DSC and confirmed lower crystallinity fraction.

INTRODUCTION

Silkworm silk fibroin (SF) is a typical natural biopolymer produced by two major species of silkworms, domestic and wild Bombyx mori (B. mori), and has been highly valued as a textile fiber for thousands of years. Silk fibers are 10-20 μm in diameter and consists of core protein (fibroin) covered by a coating layer (sericin) that glues core fibers together. Silk is an ideal candidate for biomedical applications because of combined biocompatibility, strength and toughness, which is mainly due to its antiparallel crystalline β-pleated structure; on the contrary non-crystalline regions are often described as mix of α-helices and amorphous, poorly orientated, randomly coiled sections of the peptide that usually contributes to the flexibility of the material. Both β-sheets and α-helix are stabilized by the hydrogen bonding.

In this work, a full physical, chemical and mechanical characterization of silk fibers is carried out in view of potential use of such a peculiar material in stretchable/flexible electronic devices for biomedical applications; silk structure is naturally an insulator biopolymer but it is reasonable to suppose a close correlation between secondary structure and a potential electrical current flowing through the matrix. In order to achieve reasonable electric/electronic performances, a proper modification of the silk structure and the full knowledge of the role played by doping agent are mandatory.

This work has shown that chemical and physical modification on silk backbone can be achieved with envisioned application of this material in many potential biomedial applications, such as sensing or regenerative medicine. Morover new engineering fields might take advantage of the peculiar properties of silk fibers, including photonics, optics and microelectronics.

MATERIALS AND METHODS

Degumming and fiber modification

Degumming of silk is the first step to remove the outergummy layer of sericin, whose properties are not desired: for this purpose we used sodium carbonate (Na_2CO_3) and a surfactant (sodium dodecyl sulfate, SDS) in aqueous solution at 100°C.

Three doping agents were used to modify silk structure: i) iodine in chunks, ii) calcium chloride ($CaCl_2$) and iii) potassium bromide (KBr) in aqueous solution at different concentration and different time of exposure.

Figure 1. Silk fiber during iodine vapor treatment. After 3 hours (left), after 5 hours (middle), after 26 hours (24 hours at room T and another 2 hours at 70° inside a woven) (right).

Table 1 summarizes all different level of doping, where lightly I_2 doping condition was done by placing neat silk fibers together with solid I_2 chunks for 24 hours at room temperature whereas in heavily I_2 doping, silk fibers were further exposed to I_2 vapor at 70 °C for 2 h (total 26 hours) (Fig. 1).

KBr doped	$CaCl_2$ doped	Iodine doped
KBr 0,5M (10 min)	$CaCl_2$ 0,5M (10 min)	I_2 lightly doped
KBr 1 M (10 min)	$CaCl_2$ 1 M (10 min)	I_2 heavly doped
KBr 1,5 M (10min)	$CaCl_2$ 1,5 M (10min)	
KBr 1,5 M (120min)	$CaCl_2$ 1,5 M (120min)	

Table 1. Different doping agent concentration and time of exposure used

Structural characterization

Fourier transform infrared (FTIR) spectra of the silk samples were recorded with a Bruker IFS 125HR spectrometer (NUS, Singapore) and data were treated by means of Origin Lab 8.0. Peak deconvolution and curve fitting was performed on Amide I and II of the spectrum, and the following formula was used to calculate β-sheets percentage fraction,

$$\beta sheet\,[\%] = \frac{A_\beta}{(A_\beta + A_\alpha)}\, x\, 100$$

where A_β is the crystalline integrated area whereas A_α is the amorphous one.

X-ray diffraction was recorded at room temperature from 5° to 90° at a scanning speed of 0.02/s with a Rigaku-D/Max-2550PC diffractometer (Tissue Repair Lab, NUS Singapore) with Ni-filtered Cu-K_α radiation at a wavelength of 0,1371 nm. The operating voltage and current were 40 kV and 30 mA, respectively.

Silk II structure percentage (X_c) was calculated after deconvolution using the following formula,

$$X_c[\%] = \left[1 - \frac{S_I}{S_I + S_{II}}\right] x\, 100$$

Where S_I is the Silk I crystalline integrated area (that corresponds to the sum of the areas under Silk I peaks) and S_{II} is the Silk II crystalline integrated area (that correspond to the sum of the areas under Silk II peaks).

Crystallite size in one direction was calculated based on the peak width approach: the peak width varies with 2θ as cosθ following Sherrer equation:

$$L = \frac{0.89\lambda}{FWHM cos\theta}$$

Where K=0,89 is the Sherrer constant, L is the crystallite size and FWHM is the Full Width at Half Maximum the width of the diffraction peak.

Electrical characterization

In order to characterize the electrical response under different humidity and temperature conditions, samples were mounted in two-terminal configurations with carbon paste inside a control environment chamber (Fig. 2) that was equipped with a pressure-independent humidity sensor. The sample and humidity sensor were mounted side-by-side in the middle chamber. The left chamber was connected to the water reservoir, and the right chamber was connected to a vacuum pump.

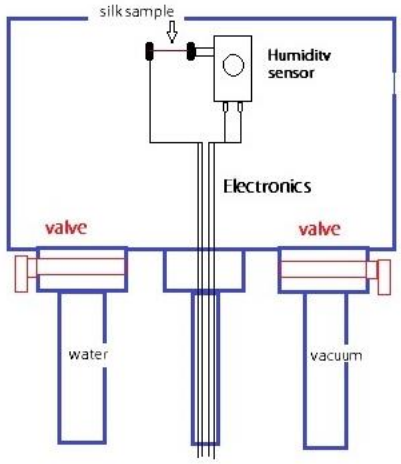

Figure 2: scheme of the humidity chamber

Mechanical characterization

Mechanical tests were carried on Instron Tester 5900. Silk fibers were first fixed onto a paper frame using double sided tape. Then the paper frame was clamped onto the Micro Tester; the paper frame was cut off before the mechanical test. The force resolution was 0.5% of indicated load, the position resolution is 0.02 µm, and strain rate is 50% per minute; the whole tests were performed at 23 °C and RH of 60%. The length of each sample was 3±0,1 cm.

Thermal characterization

Thermal characterization was carried out by using a Perkin Elmer DSC7 machine with a scanning rate of 10K/min from -10°C to 400°C; samples with masses of about 5 mg each were encapsulated in Al pans with a special instrument. The DSC equipment was calibrated for empty cell baseline, and with aluminum for heat flow and temperature. Al reference standard was used for calibration of the heat capacity through a run method.

RESULTS AND DISCUSSION

Secondary structure analysis

FTIR and XRD analysis revealed structural change in all three doped samples: doping at 70 °C (heavily I_2 doping) caused a major decrease in the fraction of β-sheets from 59% to 49% as indicated by the intensity decrease of the 1497 cm^{-1} peak (in Amide II) and 1618 cm^{-1} (in Amide I) bands. The intensity decrease in the β-sheet bands and the increase in the α- helix bands indicated that some of the β-sheets were destabilized and transformed into α-helices or random coils. The peak at 1649 cm-1 (α-helix) of the neat sample moved to 1658 cm-1 in the heavily iodinated one and this is a clear evidence of this transformation (Fig.3)

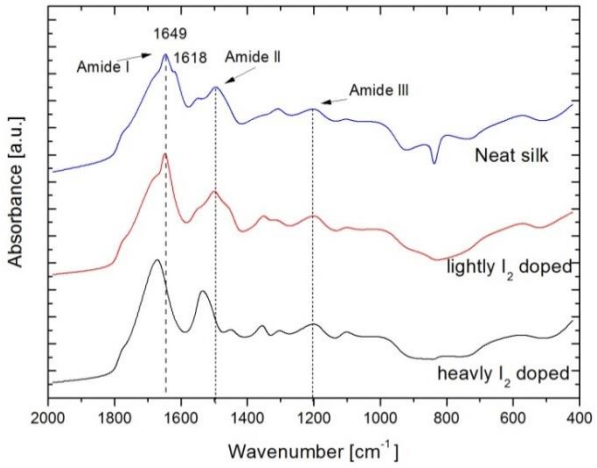

Figure 3.FTIR spectrum of iodinated silk fiber; comparison between neat, lightly and heavily I_2 doped silk fiber in the range of 2000-400 cm^{-1}

Similar modifications were found in salt doped silk spectra where the intensity of the peak at 1618 cm^{-1} in the Amide I (β-sheet) progressively decreases in intensity from neat to high concentration doped samples. This trend is confirmed in the Amide III, where the shoulder peak at 1260 cm^{-1} (C=N stretch) decreased, whereas the peak at 1229 cm^{-1} increased; the former was assigned to β-sheet, and the latter was assigned to random coil.

It is likely that during the treatments, iodine (in forms of polyiodide ions I_3^- and I_5^-) and ions coming from salts coordinate with polar later groups of the peptide chain destroying the secondary bonds between α-helices and β-sheets.

Evidence of this partial transformation has been obtained by XRD diffraction profile by which Silk I and Silk II crystalline structure

were studied: B. mori silk has been known to adopt two crystal structures named silk I (α-form, type II β-turn), and silk II (β-pleated sheet); the corresponding d-spacings for silk I and II are as follows (in nanometers): 0.98 (II), 0.74 (I), 0.56 (I), 0.48 (II), 0.44 (I), 0.43 (II), 0.41 (I), 0.36 (I), 0.32 (I), 0.28 (I). In Fig. 4 relative diffraction angles (2θ) are shown (red vertical lines refer to Silk II structure).

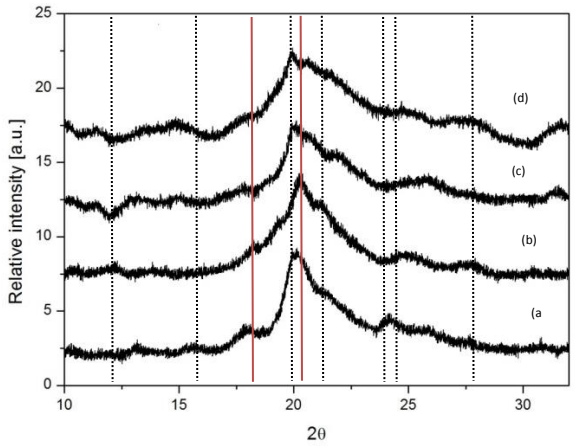

Figure 4. XRD Diffraction profile of neat degummed (a), heavily I_2 doped (b), 1,5M $CaCl_2$ 2h doped (c) and 1,5M KBr 2h doped (d) silk fibers. Red vertical lines are related to Silk II structure diffraction angles.

Silk I and Silk II peak intensity reduces with iodinization. This is an indication that I_2 destroyed secondary bonds between helices and sheets thus creating amorphous phases. This is more evident in $CaCl_2$ modified sample where almost all the peaks related to α-form decrease in intensity (2θ= 11,81°, 15,62°, 21,38° , 24,4° , 24,73°) and this is due to the destruction of secondary H-bond by calcium ions; a similar diffraction profile is seen for KBr doped fiber but the differences in the peaks at 2θ = 11,81° and 21,38° respect to $CaCl_2$ ones, point us that destruction of secondary bonds is less likely in this case;

Conductivity measurements

Conductivity measurements revealed a strict dependence of current intensity on temperature and relative humidity. No current was detected at low level of T (<20°C) and RH (<35%) for neat sample whereas after doping an increase and an early activation of conductivity was revealed. While for salt doped sample increase in conductivity is only one order of magnitude, maximum increment respect to neat silk was shown by iodinated sample whose conductivity reaches 10^{-3} S/cm at a fixed temperature value (50°C) (Fig.6). Differences between heavily and lightly samples indicates that β-sheets fraction affects charge carrier diffusion by acting as barriers to the circolation.

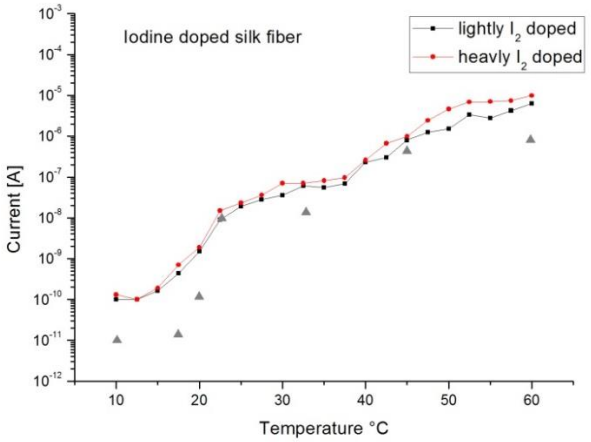

Figure 5. Current response of iodinated silk fiber against temperature at fixed room RH value (scatter triangles refer to neat sample values)

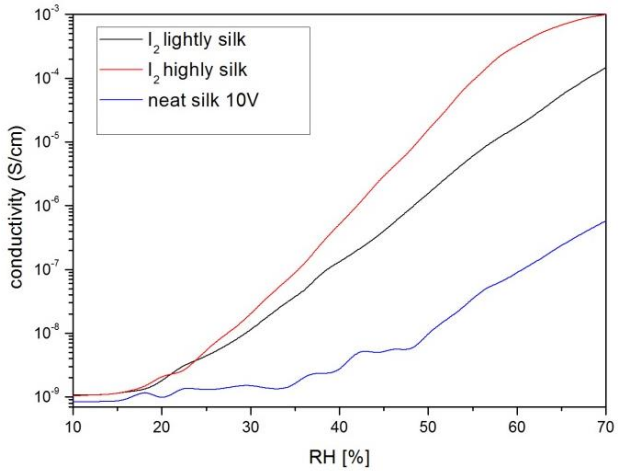

Figure 6. Conductivity response of iodinated silk fiber against RH at fixed T value (blue line refers to neat sample response).

Early activation of current is shown both for iodine and salt doped fibers and both for T and RH increment; figure 5 shows that even at low temperature ionic current is triggered.

Qualitative ionic conductivity model was proposed with ions-water complex formation

and thermal activated diffusion through silk matrix.

Mechanical behavior

The strength of silk is attributed to the compacted β-sheet structures which add resistance to the tensile force applied. Modification in size and crystalline fraction has a great effect on mechanical behavior, for this reason uniaxial tensile tests have been proposed with the purpose to quantify the effect of structural change of doped silk on elastic modulus, fiber strength and toughness.

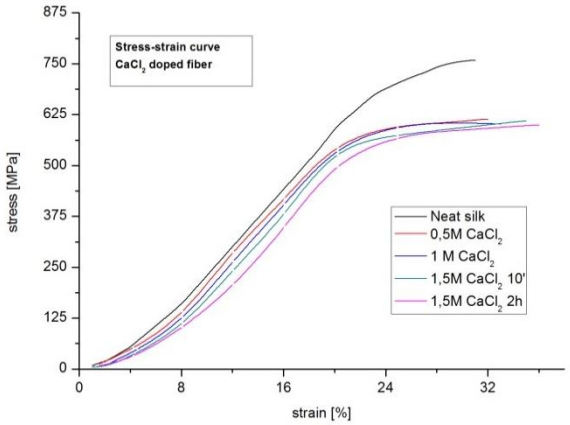

Figure 7. $CaCl_2$ doped silk fiber stress-strain plot.

All doped samples show lower breaking stress and higher elongation up to fracture whereas toughness is progressively higher by increasing doping level. $CaCl_2$ treated sample shows reduction of stiffness in the final region of stress-strain plot: high reduction in weight (32,11%) recorded after calcium salt treatment suggests the creation of microporous structure into the matrix and coalescence of pores at high level of stress caused decrease in strenght. For all the others doped samples reduction in stiffness is attributable to lower crystalline fraction and lower crystallite size.

Thermal degradation

DSC confirmed all the assumptions made regarding structure modification, showing how degradation peak changed with doping and doping concentration; Figure 8 shows DSC curves of $CaCl_2$ treated sample in which have been highlighted respectively bounded water evaporation temperature (T_{ev}) that exceeds boiling water temperature (100°C) as indication of the presence of ions in the matrix, T_h that is referred to the weakening of hydrogen bonds within helices and sheets, and degradation temperature T_d that is referred to thermal degradation of silk matrix.

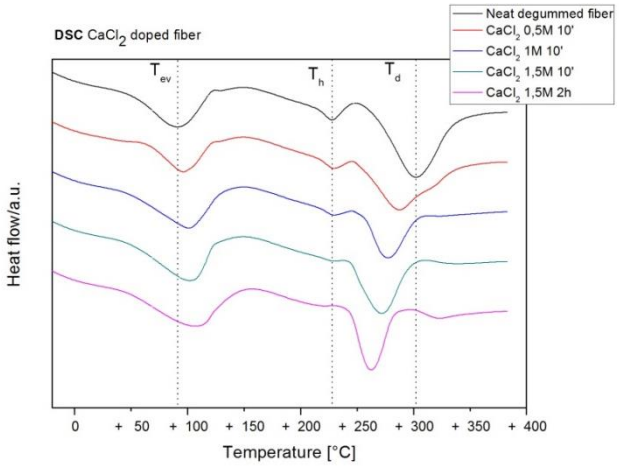

Figure 8. DSC curves of $CaCl_2$ doped silk fibers at different doping concentration; vertical line are related to founded temperatures of neat degummed silk fiber.

It is evident how lower crystalline fraction shifted degradation temperature to lower values and made T_h peak less evident as indication that most of secondary bonds were destroyed by doping agent.

CONCLUSION

Understanding of secondary protein structure role on silk properties is the starting point to achieve improved performances of silk based materials. The results of this work have shown that properties like ionic conduction, degradation and mechanical performances can be tailored through suitable ionic doping.

Even though values of conductivity are not yet comparable to those of well-studied semiconducting polymers such as PANI or PPS:PEDOT they represent a good achievement; however, further efforts will be required to achieve even better improvements in this regards.

Until now there have been many studies concerning the functionalization of silk, but scarce efforts have been made to use it as a conductive element, with multiple implication on unconventional areas such as sensors, microelectronics, smart textiles.

Results from versatile chemistry used in this work do not exhaust possible modification but revealed that iodine is a good candidate for electronic properties enhancements.

CARATTERIZZAZIONE DI FIBRE DI SETA BOMBYX MORI DOPATE

ABSTRACT

In questo lavoro viene effettuata un'analisi fisica, chimica e meccanica di fibre di seta B. mori, con particolare attenzione all'effetto di tre diversi agenti dopanti (I_2, $CaCl_2$ e KBr) sulla struttura secondaria della fibroina; L'analisi FTIR e XRD rivela che le fibre dopate presentano una minore fase cristallina ed una minore dimensione dei cristalliti, dovuta ad una destabilizzazione delle β-lamelle e alla trasformazione in conformazione amorfa random coil. Un modello qualitativo di conduzione ionica è stato proposto per motivare l'incremento di corrente all'aumento di temperatura e umidità relativa osservato nelle fibre iodate. L'incremento di tenacità e la riduzione dello sforzo massimo a rottura, studiati con test di trazione monoassiali, confermano le ipotesi sull'alterazione della struttura della fibroina di seta a seguito dei trattamenti. La degradazione termica dei diversi campioni è stata studiata con DSC, e conferma la minor percentuale di fase cristallina delle fibre dopate rispetto a quelle native.

INTRODUZIONE

La fibroina della seta (SF) è un tipico biopolimero naturale prodotto da due specie principali di bachi da seta, Bombyx mori domestico e selvatico, ed è stato molto apprezzato come fibra tessile per migliaia di anni. Le microfibrille di seta sono 10-20 micron di diametro e constano di una proteine nucleo (fibroina) coperta da una proteina di rivestimento (sericina) che agisce da collante. La seta è un candidato ideale per molte applicazioni biomediche grazie alla combinazione tra tenacità biocompatibilità e resistenza, dovuta principalmente alle β-lamelle antiparallele cristalline; la fase amorfa, costituita da α-eliche non orientate e random coil, contribuisce di solito alla flessibilità del materiale. Sia le β-lamelle che le e α-eliche sono stabilizzate dai legami ad idrogeno.

In questo lavoro viene proposta una completa caratterizzazione fisica, chimica e meccanica delle fibre di seta in vista di un potenziale uso di questo specifico materiale in dispositivi ad elettronica flexible e stretchable.

La seta è un polimero isolante ma è ragionevole supporre una stretta correlazione tra struttura secondaria e la possibile diffusione di corrente ionica in presenza di umidità; con l'intento di ottenere ragionevoli performace elettriche/elettroniche, una corretta modifica della struttura della seta e un'accurata comprensione del ruolo dell'agente dopante è obbligatoria; questo studio mostra come diverse modifiche della struttura possano essere ottenute con diverse concentrazione di dopante ed oltre ad applicazioni in campo biomedico e medicina rigenerativa, nuovi campi dell'ingegneria, come la sensoristica, la fotonica e l'ottica potrebbero sfruttare le peculiarità e le proprietà delle fibre di seta.

MATERIALI E METODI

Degumming e doping della seta

Il degumming della seta ha l'obbiettivo principale di rimuovere lo strato esterno di sericina le cui proprietà non sono di particolare rilevanza; a questo scopo è stato usato carbonato di sodio (Na_2CO_3) ed un tensioattivo (sodium dodecyl sulfate, SDS) in soluzione acquosa a 100°C.

La struttura della seta è stata modificata con tre diversi agenti dopanti, rispettivamente i) dicloruro di calcio ($CaCl_2$), ii) bromuro di potassio (KBr) in soluzione acquosa e iii) iodio puro in pezzi, a diverse concentrazioni molari e diversi tempi di esposizione della fibra.

Figura 1. Fibre di seta durante il trattamento ai vapori di iodio. Dopo 3 ore (sinistra), dopo 5 ore (centro), dopo 26 ore (24 ore a 25°C e altre 2 ore a 70°C in un forno) (destra).

La Tabella 1 riassume i diversi livelli di doping e i tempi di esposizione, nella fattispecie la condizione I_2 lightly è ottenuta ponendo insieme le fibre con iodio in pezzi per 24 ore a 25°C, mentre per la condizione I_2 heavily le fibre sono state esposte ai vapori per altre 2 ore a 70°C (26 ore totali) (Fig.1).

KBr doped	$CaCl_2$ doped	Iodine doped
KBr 0,5M (10 min)	$CaCl_2$ 0,5M (10 min)	I_2 lightly doped
KBr 1 M (10 min)	$CaCl_2$ 1 M (10 min)	I_2 heavly doped
KBr 1,5 M (10min)	$CaCl_2$ 1,5 M (10min)	
KBr 1,5 M (120min)	$CaCl_2$ 1,5 M (120min)	

Tabella 1. Diversi livelli di doping utilizzati e tempi di esposizione al dopante.

Caratterizzazione strutturale

Gli spettri dei campioni da spettroscopia infrarossa a trasformata di Fourier (FTIR) sono stati ottenuti con uno spettrometro Bruker IFS 125HR (NUS, Singapore) e analizzati usando il software Origin Lab 8.0. Il curve fitting e la deconvoluzione dei picchi è stata eseguita sulle ammidi primarie e secondarie dello spettro, ed in seguito si è utilizzata la seguente equazione per derivare la frazione percentuale di β-lamelle,

$$\beta sheet\ [\%] = \frac{A_\beta}{(A_\beta + A_\alpha)}\ x\ 100$$

dove A_β è la somma integrata delle aree dei picchi cristallini, mentre A_α è relativa ai picchi amorfi.

La diffrazione a raggi X è stata eseguita a temperatura ambiente da 5° a 90° ad una velocità di scansione di 0.02°/s con un diffrattometro Rigaku-D/Max-2550PC (Tissue Repair Lab, NUS Singapore) con filtro al Nickel e radiazione Cu-K_α ad una lunghezza d'onda di 0,1371 nm. Il voltaggio operante è di 40kV e la corrente di 30 mA.
La frazione percentuale di Silk II (X_c) calcolata a seguito di deconvoluzione dei picchi è stata derivata con la seguente equazione:

$$X_c[\%] = \left[1 - \frac{S_I}{S_I + S_{II}}\right] x\ 100$$

Dove S_I è la somma integrata delle aree dei picchi relativi alla struttura cristallina Silk I mentre S_{II} si riferisce alle aree della struttura Silk II.
La dimensione dei cristalliti lungo una direzione è stata calcolata con l'approccio della larghezza a metà altezza dei picchi, seguendo l'equazione di Sherrer:

$$L = \frac{0.89\lambda}{FWHMcos\theta}$$

dove K=0,89 è la costante di Sherrer, L è la dimensione dei cristalliti e FWHM è la larghezza a metà altezza dei picchi di diffrazione Silk II (β-lamelle).

Caratterizzazione elettrica

Per caratterizzare la risposta elettrica a diverse condizione di temperatura e umidità relativa, i campioni sono stati montata in configurazione a due terminali con pasta di carbonio all'interno di una camera ad ambiente controllato (Fig. 2) dotata di un sensore di umidità e di pressione indipendenti. Il sensore di umidità ed il campione sono stati montati fianco a fianco nella camera centrale. La camera sinistra era collegato al serbatoio d'acqua, quella di destra è stata collegata ad una pompa a vuoto.

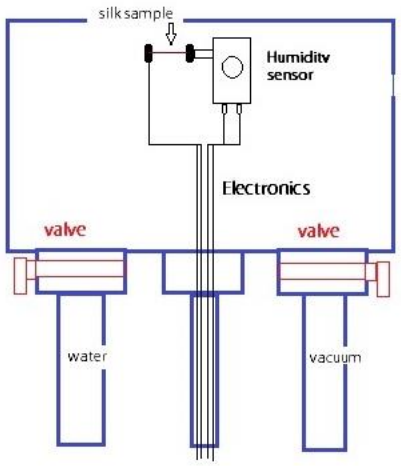

Figure 2: schema della camera ad ambiente controllato

Caratterizzazione meccanica

I test meccanici in trazione monoassiale sono stati effettuati con una Instrom Tester 5900 (NUS, Singapore). Le fibre di seta sono state inizialmente fissate su di una cornice di carta con nastro biadesivo e la stessa cornice è stata agganciata ai morsetti dopo aver tagliato i lati; la risoluzione della forza era 0,5% del carico indicato, la risoluzione dell'allungamento 0,02 micron, e velocità di deformazione era del 50% per minuto; le intere prove sono state eseguite a 23°C e RH del 60%. La lunghezza media dei campioni era 3±0,1 cm.

Caratterizzazione termica

L'analisi termica è stata effettuata una Perkin Elmer DSC7 ad un rate di scansione di 10K/min da -10 a 400°C; i campioni, con massa media di 5 mg ciascuno, sono stati incapsulati in crogioli di alluminio e saldati a freddo. La macchina è stata calibrata a cella vuota e successivamente con alluminio per determinare il flusso termico e la temperatura.

RISULTATI E DISCUSSIONE

Analisi della struttura secondaria

L'analisi FTIR a XRD ha rivelato cambiamenti nella struttura secondaria delle fibre trattate con iodio e sali: il doping a 70°C con iodio (heavily I_2 doping) ha causato il maggior decremento della frazione cristallina β-lamelle da 59% a 49% come indicato dalla diminuzione dell'intensità dei picchi a 1497 cm^{-1} (in Ammide II) e 1618 cm^{-1} (Ammide I). Questa diminuzione e l'aumento in bande α-eliche indica che parte dei cristalliti viene destabilizzata e trasformata in α-eliche o random coil. Il picco a 1649 cm^{-1} (α-eliche) del campione nativo viene spostato a 1658 cm^{-1} nel campione trattato con iodio e questa è una chiara evidenza di questa trasformazione (Fig. 3).

Simili cambiamenti sono stati rilevati negli spettri dei campioni trattati con sali dove l'intensità del picco a 1618 cm^{-1} diminuisce progressivamente in intensità passando dal campione non trattato a quelli ad alto livelli di doping. Questa tendenza è evidenziata anche nell'Ammide III dove il picco a 1260 cm^{-1} (legame C=N) diminuisce in intensità mentre il picco a 1229 cm^{-1} cresce. Il primo è legato alle β-lamelle, il secondo al random coil.

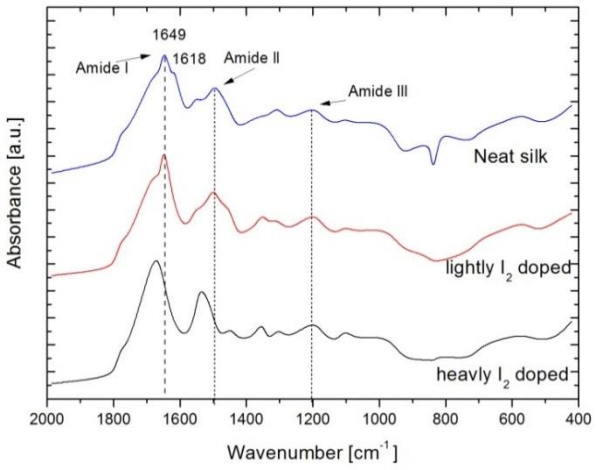

Figura 3. Spettro FTIR della seta trattata con iodio; confronti tra seta nativa, lightly e heavily I_2 nel range tra 400 e 2000 cm^{-1}.

È probabile che lo iodio (in forma di anioni I_3^- I_5^-) e gli ioni provenienti dai sali si coordinano con gruppi polari della catena peptidica distruggendo i legami ad idrogeno.

La prova di questa parziale trasformazione della struttura è stata confrontata con diffrazione XRD con il quale sono stati studiate le strutture cristalline Silk I e Silk II: la fibroina B. mori adotta infatti due strutture cristalline denominate Silk I (α-eliche, β-turn di tipo II) , e Silk II (β-lamelle); il corrispondente d-spacing per Silk I e II è il seguente (in nanometri): 0.98

(II), 0.74 (I), 0,56 (I), 0.48 (II), 0.44 (I), 0.43 (II), 0.41 (I), 0.36 (I), 0.32 (I), 0.28 (I). In Fig. 4 I relativi angoli di diffrazione (2θ) sono mostrati (le linee verticali rosse si riferiscono alla struttura Silk II).

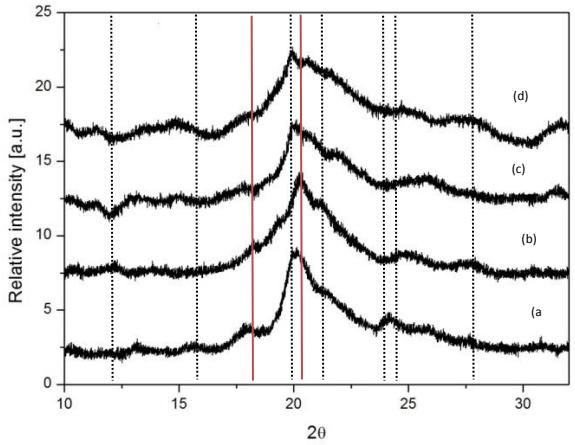

Figura 4.Profili di diffrazione XRD di fibra native (a) heavily I_2 (b) 1,5M $CaCl_2$ (c) 1,5M KBr 2h (d)2. Le linee verticali rosse si riferiscono alla struttura cristallina Silk II

L'intensità dei picchi Silk I e II si riduce a seguito del trattamento con iodio; questo indica che le molecole convertono α-eliche e β-lamelle in random coil. Questo è molto evidente nel campione trattato con $CaCl_2$ dove quasi tutti i picchi legati alla struttura Silk I decrescono in intensità (2θ= 11,81°, 15,62° , 21,38° , 24,4° , 24,73°) soprattutto a causa della coordinazione dei cationi calcio con i gruppi laterali, a discapito dei legami idrogeno; simile risulta il profilo del campione trattato con KBr ma la differenza tra I picchi a 2θ = 11,81° e 21,38° rispetto al precedente campione indica che la distruzione dei legami secondari è meno evidente in questo caso.

Misura di conduttività

Le misure di conduttività dimostrano un stretta dipendenza dell'intensità di corrente dalla temperature e dall'umidità relative. Non viene rilevata corrente per valori bassi di T (<20°C) o di RH (<35%) per la seta nativa, mentre a seguito del doping si assiste ad un incremento di conduttività ed un'attivazione della stessa per valori inferiori di RH e T.

Mentre per i campioni dopati con sali l'incremento di conduttività rispetto alla fibra nativa è di un ordine di grandezza, il maggior aumento viene osservato per la seta iodinata, la cui conduttività raggiunge 10^{-3} S/cm a T fissa (50°C) (Fig.6). Le differenze tra la curva dei campioni heavily e lightly I_2 suggerisce che la frazione e la dimensione dei cristalliti ostacola il passaggio di portatori di carica ionici agendo da barriere alla diffusione; la presenza di anioni ha comunque un contributo maggiore sull'aumento di corrente.

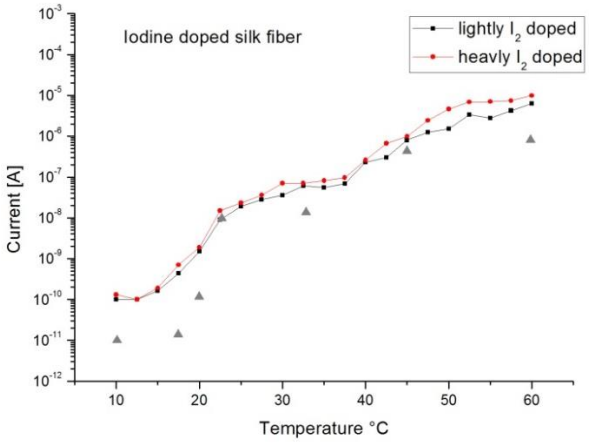

Figure 5. Risposta in corrente dei campioni dopati con iodio all'aumento di temperatura. I triangoli si riferiscono ai valori della fibra nativa.

Il passaggio di corrente viene attivato per T e RH minori anche nei campioni dopati con sali la cui concentrazione influisce progressivamente sulla conduttività, aumentandola.

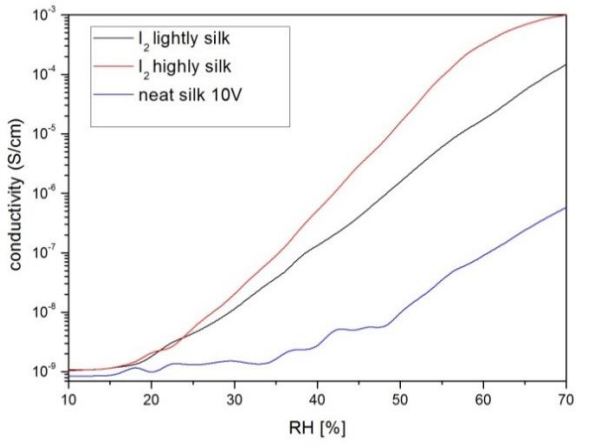

Figura 6. Risposta in conduttività dei campioni dopati con iodio e confronto con la risposta della seta nativa all'aumentare dell'umidità relativa.

Comportamento meccanico

La durezza della seta è legata alle strutture compatte β-lamelle che incrementano la resistenza alla forza di trazione applicata. L'alterazione della dimensione e della frazione percentuale di cristalliti ha un grande effetto sul comportamento meccanico; i test a trazione monoassiali sono stati effettuati con lo scopo di determinare il modulo elastico, la durezza, l'elongazione a rottura e la tenacità dei diversi campioni.

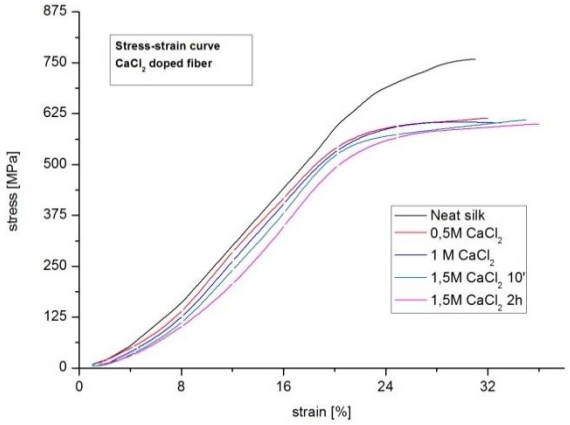

Figure 7. Curva stress vs strain del campione trattato $CaCl_2$

Tutti i campioni dopati presentano un minor carico a rottura ed un elongazione maggiore rispetto alle fibre native, mentre la tenacità è progressivamente maggiore all'aumentare del livello di doping. Il campione trattato con $CaCl_2$ presenta una marcata riduzione di resistenza nel tratto finale del plot stress vs strain: la riduzione di peso considerevole (32,11%) a seguito del trattamento suggerisce la creazione di una struttura microporosa all'interno del matrix e la possibile coalescenza dei pori ad alti livelli di sforzo riduce notevolmente la resistenza. In generale, anche per gli altri campioni dopati la perdita di resistenza è dovuta ad una minore frazione cristallina.

Degradazione termica

La DSC conferma le considerazioni riguardo le alterazioni delle struttura secondaria, mostrando come il picco di degradazione termica dipenda dal doping e dalla concentrazione di dopante. La figura 8 mostra la curva DSC del campione drogato con $CaCl_2$ in cui sono stati evidenziate la temperatura di evaporazione dell'acqua (T_{ev}), che supera i 100°C a causa della presenza degli ioni, la temperatura di indebolimento dei legami secondari delle eliche e delle lamelle (T_h) e la temperatura di degradazione termica della seta (T_d).

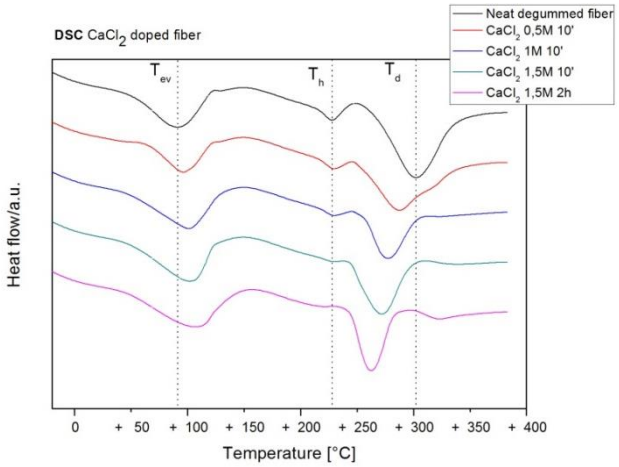

Figure 8. Curva DSC del campione trattato con $CaCl_2$ a diverse concentrazioni; le linee verticali si riferisco alle temperature del campione di seta nativa.

È evidente come la minor frazione cristallina sposti il picco di degradazione termica verso valori più bassi di temperatura ed inoltre il picco T_h risulta meno evidente come ad indicare che parte dei legami secondari vengono distrutti dagli ioni dopanti.

CONCLUSIONI

La comprensione del ruolo della struttura secondaria sulle proprietà della seta è fondamentale per ottenere performances avanzate con i materiali a base seta. Questo studio rivela come sia possibile controllare alcune proprietà come la conduzione ionica, la tenacità e la degradazione termica con diversi agenti dopanti e diverse concentrazioni. Anche se i valori di conduttività non sono ancora confrontabili con quelli raggiunti da polimeri semiconduttori come PANI o PPS:PEDOT essi stabiliscono un buon traguardo; ulteriori sforzi devono essere promossi per ottenere miglioramenti in questo senso.

Fino ad ora sono stati presentati diversi studi sulla funzionalizzazione della fibroina ma pochi di essi si focalizzano sull'uso di essa come elemento conduttivo, con notevoli applicazioni in campi non convenzionali per la seta, come la sensoristica, la microelettronica o la smart texile. Questi risultati suggeriscono che lo iodio rappresenta un ottimo candidato per aumentare le performaces elettroniche della seta.

CONTENTS:

LIST OF ABBREVIATIONS:

SF = SILK FIBROIN

RH= RELATIVE HUMIDITY

SCM= SILK COCOON MEMBRANE

FTIR= FOURIER TRANSFORM INFRA-RED SPECTROSCOPY

DSC = DIFFERENTIAL SCANNING CALORIMETRY

XRD = X-RAY DIFFRACTION

NUS = NATION UNIVERSITY OF SINGAPORE

WECT = WIRE ELECTROCHEMICAL TRANSISTOR

PPY= POLYPIRROLE

Chapter 1:
INTRODUCTION

1.1 SIGNIFICANCE

Silk proteins belong to a class of unique, high molecular weight, block copolymer-like proteins that have found widespread use in biomaterials and regenerative medicine. The useful features of these proteins, including self-assembly, robust mechanical properties, biocompatibility and biodegradability can be enhanced through a variety of chemical modifications.

Efforts were made in modifications of silk backbone; Have been provide chemical handles for the attachment of growth factors, cell binding domains and other polymers to silk, expanding the range of cell and tissue engineering applications attainable (Amanda R. Murphy, 2009).

The ability to further tune the surface chemistry of silk materials is desirable to control the interaction between silk and living systems. Biomaterial surface chemistry is known to influence a variety of cell responses ranging from changes in surface adhesion to activation of biochemical pathways regulating cellular proliferation, differentiation, and survival. The presence of several reactive amino acids in SF allow chemical modification strategies to be utilized to tailor the protein for a desired application.

Besides this, silk fibers and thin film are suitable candidates for many applications, especially in the microelectronics fields: for instance silk thin film have been used as gate dielectric for a flexible organic thin film transistor (H. Wang, 2011) or as substrate for implantable device (Kim D. H. et al. , 2009); moreover silk fibers are suitable candidates for a novel approach to electronic circuits or, if blended with conductive polymer, as electrode material for sensing application (S. Tsukada et al. , 2012). Recently, there have been reports of using silk as a low cost e-paper device, or as a replacement for traditional inorganic oxide layer such as SiO_2 or PMMA. (H. Wang, 2011)

At some point, one must recognize that the silk-based materials could be used for multiple applications in the electronics field, despite their intrinsic nature as insulators. For this reason, a more detailed study of the structure and properties of silk is an important starting point to imagine many implications in this regard.

1.2 HYPOTESIS AND AIMS:

Depending on the application the physical and chemical properties of SF have to be tailored so in this work we present three different modification that will help to achieve some proper properties for potential application of silk material.

Silk materials are natural protein-based materials with an exceptional toughness. In addition to their toughness, silk materials also possess complex physical properties and functions resulting from a particular set of amino-acid arrangement that produces structures with crystalline β-sheets connected by amorphous chains. Extensive studies have been performed to study their structure-function relationship leading to recent advancements in bio-integrated devices. Applications to fields other than textiles and biomedicine, however, have been scarce. Silk biomaterials have the convenience of possessing material attributes that make them ideal constituents of technological devices such as planar microelectronic structures.

Since this material is offered as a prime candidate for engineering applications, it should be a thorough study of the microstructure and the ability to change the properties.

In this dissertation, an investigation of the electronic, mechanical, structural and thermal properties, and role of silk materials in the field of organic materials is presented. The investigation is conducted from an experimental physics point of view where correlations with charge transport mechanisms in disordered, semiconducting, and insulating materials are made when appropriate.

We propose three different modification method to dope silk fibroin in order to study how mechanical, structural, thermal and electric properties can change after the treatment.

A full physic and chemical characterization will be conducted with a particular attention to protein structure and the crystalline fraction content inside the modified silk fibroin (SF); the extent of crystalline part inside silk matrix is a crucial factor that control multiple characteristics from conductivity to degradation behavior and for this reason a correlation between secondary structure and properties is our starting point.

Finally, it is proposed a simple technique to produce a thin biofilm of doped silk that can be used in electronics as a conductive element, exploiting for example, as a core element in miniaturized sensors.

According to the stated objectives, Figure 1 explains a scheme of the thesis.

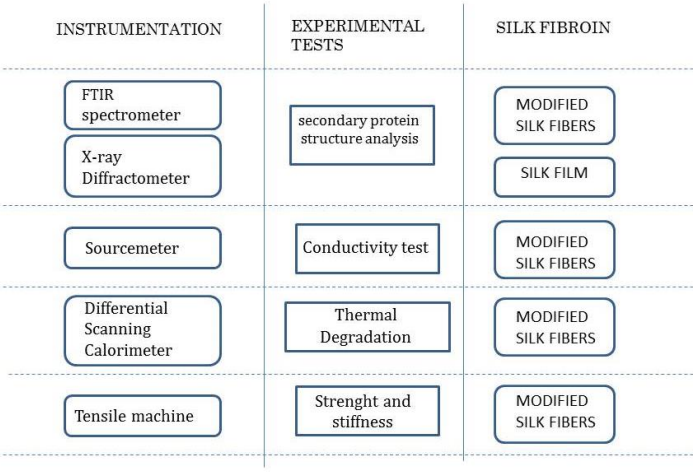

Figure 1: flow diagram describing thesis content

REFERENCES

Amanda R. Murphy and David L. Kaplan. Biomedical applications of chemically-modified silk fibroin. J. Mater. Chem., 2009, 19, 6443–6450

Chung-Hwa Wang, Chao-Ying Hsieh, Chang Hwang. Flexible Organic Thin-Film Transistors with Silk Fibroin as the Gate Dielectric. Advanced Materials Volume 23, Issue 14, pages 1630–1634, April 12, 2011

Dae-Hyeong Kim, Yun-Soung Kim, Jason Amsden, Bruce Panilaitis, David L. Kaplan, Fiorenzo G. Omenetto, Mitchell R. Zakin, and John A. Rogers. Silicon electronics on silk as a path to bioresorbable, implantable devices. Appl Phys Lett. 2009 Sep 28; 95(13)

Tsukada S, Nakashima H, Torimitsu K (2012) Conductive Polymer Combined Silk Fiber Bundle for Bioelectrical Signal Recording. PLoS ONE 7(4): e336. doi:10.1371/journal.pone

Chapter2: THEORETICAL BACKGROUND

2.1 INTRODUCTION TO SILK FIBROIN

Silks are generally defined as protein polymers that are spun into fibers by *Lepidoptera* larvae such as silkworms, spiders, scorpions, mites and flies. Silk was discovered in China in around 2700 B.C. and is traditionally manufactured by sericulture. This ancient art was practiced in China, Korea and Japan since fourth century and in sixth century this technique reached Europe via the Silk Road

Silk is now produced across Asia and Europe, although the main sources are Japan, China and India. It has been of interest for over 5000 years not only for its textile properties of texture, tenacity but also its use in cosmetics creams, lotions, makeup, powders, bath preparations and pharmaceuticals.

Silk fibroin is a potent alternative to other biodegradable biopolymers for bone tissue engineering, because of its tunable architecture and mechanical properties, and its demonstrated ability to support bone formation both in vitro and in vivo; the strength of a biomaterial is very important for the design of scaffolds. They should mimic the mechanical properties of the replacing tissue (V. Kearns, 2008)

Silk is an ideal candidate for biomedical applications because of combined strength and toughness, which is mainly due to its antiparallel β-pleated structure. The most extensively used silk for various applications are those from silkworm *Bombyx mori* and spider silk *Nephila clavipes*. *Bombyx mori* silk is available in abundant amount from the cocoon fibers but it is not equitable to grow spiders in the farm because of their predatory nature. The advances in genetic engineering and biotechnology have allowed the scientists to produce rigenerate spider silk protein in variety of host organisms.

2.1.1 SILKWORM SILK

Silkworm silk is commonly produced from the cocoons of domestic moths, *Bombyx mori*. Silk fibers are 10-20 μm in diameter. Each fiber consists of core protein covered by a coating protein (sericin) that glues core fibers together.

Microfibrils (very fine fibrils by which silk structure is composed) are not circular in cross section but appear triangular as seen in Figure 2.1 (Y. Shen et al., 1998). The core protein

consists of three chains: heavy chain, light chain and a glycoprotein P25: heavy and light chains are connected by disulphide bonds. Light chain is necessary for the secretion of protein from the silk glands. P25 is connected to both heavy and light chains by noncovalent interactions and it is necessary for the assembly of heavy and light chains. Heavy chain is fiber forming protein and its structure determines properties of silk fiber and it is commonly referred as fibroin protein. Electrophoretic analyses of silk cocoons have revealed presence of several minor proteins of unknown function. These low molecular weight proteins are classified as non-structural silk proteins (A. R. Padol et al. , 2012).

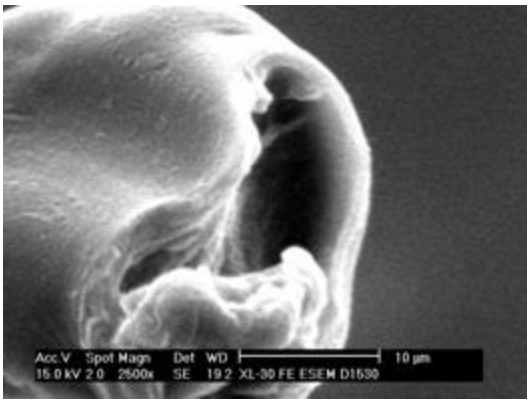

Figure 2.1. Electron microscopic image showing cross section of *Bombyx mori* silk fiber. (Y. Shen, 1998)

2.1.2 SILK PROTEIN STRUCTURE

Silk material is a protein-based polymer. A protein is described by a sequence of molecules called amino acids. Amino acids are classified based on the type of side chains (R groups) that are attached to a certain protein backbone. In Figure 2.1, there is a list of the side chains of amino acids that are present in silk materials. There are many types of protein backbone, but in the case of silk material, it has a protein backbone similar to nylon-6, as shown in Figure 2.1. When multiple backbone molecules are connected, they form a secondary structure.

Several secondary structures commonly found in silk material include β-strand, β-sheet, α-helix, and 31-helix (E. Steven, 2012).

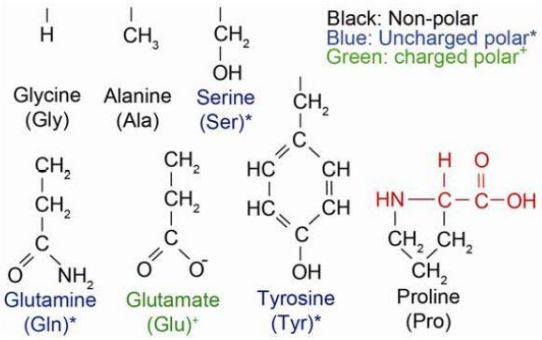

Figure 2.2 Amino acid side chains found in silk materials. The red-labeled structure corresponds to a protein backbone segment (E. Steven, 2012).

When two or more of these β-strands are connected through hydrogen bonding, they form β-sheets. Two kinds of β-sheets are available, parallel or anti-parallel β-sheets. In silk materials, anti-parallel β-sheets are the only available.

The β-sheets can be stacked to form a block co-polymer crystalline, usually contributing to the hardness of the material. On the contrary, the arrangement of a α-helix or 31 helix usually contributes to the flexibility of the material. This arrangement is stabilized by the hydrogen bonding connecting the N-H group of a particular backbone molecule to the C=O group of the forth earlier backbone molecule. Similarly, 31 helix is also stabilized by hydrogen bonding between the N-H and C=O group, except that in this case, each turn of helix is composed only of 3 amino acids (E. Steven, 2012).

2.1.3. BOMBYX MORI FIBROIN SILK PROTEIN STRUCTURE

Similar to the protein structure of spider silk, Bombyx mori cocoon silk also contains amino acids repetitions. There are two main types of proteins present in the cocoon silk, namely the fibroin and sericin. Fibroin is the main protein that corresponds to the internal structure of the silk fiber and sericin is the protein that corresponds to the glue that binds the fibers in forming the cocoon. The fibroin is composed of multiple repeats of GAGAGS (where S is serine,

A is Alanine and G is Glycine) arranged as β-sheets that are connected with minor amount of random amorphous chains.

Because the fibroin is composed mainly of β-sheets, the Bombyx mori silk fibers is more rigid compared to spider silk fibers. The sericin is a highly hydrophilic and water-soluble protein. It is composed mostly of glycine, serine, and aspartic acid. About 25 wt% of sericin is present in a silkworm cocoon.

2.3 HIERARCHICAL STRUCTURE

The unique formation process results into the silk fibers with complex and ingenious hierarchical structures (Figure 2.3). Increasing understanding on the hierarchical structures of silks has been attained with different structural analysis tools. Structural information on the molecular packing and crystallite arrangement has been obtained from X-ray diffraction (XRD). It is shown that the β-nano crystallites in silks consist of anti-parallel β-sheets and lie mainly parallel to the fiber long axis (Figure 2.3a).

Bombyx mori silk has been known to adopt two crystal structures named silk I (α-form, type II β-turn), and silk II (β-form, antiparallel, β-pleated sheet) (Lu et al. ,2 001). Suggested lattice indexes were shown for silk I and II conformation and have been critically compared to the well-known 'crankshaft' model (Lotz and Keith, 1971).

Studies using nuclear magnetic resonance (NMR) were able to identify the amino acid involved in different secondary structure components, and crystallite regions in spider and silkworm silk were found to be in two possible states, highly oriented or poorly oriented (H. Simmons, 1996).

Utilizing Fourier transform infrared spectroscopy (FTIR) and Raman spectroscopy, recent studies have provided us with further knowledge on the percentage of different secondary structure components in silks. In addition, nano-silk fibrils have been revealed by small angle X-ray scattering and atomic force microscopy (Yang Z. et al., 1997).

These studies, combined with numerical simulation, have generated different molecular models for the hierarchical structure of silks. In early semi-crystallite model, silks are considered as composite materials in which β-nano crystallites embed in the amorphous protein matrix (Figure 2.3a). The crystallite regions consist of highly oriented β-nano

crystallites and weakly oriented β-sheets. Different regions play different mechanical roles: The β-nano crystallites are thought to serve as molecule cross-links and provide silks great strength while the non-crystallite regions are responsible for their superb elasticity. Simulation based on this model successfully reproduces the stress-strain curves consistent with experiment. In the "string of beads" model (Figure 2.3b) (Vollrath F. et al. , 2006) the molecular structure in silks is suggested to be a hairpin structure with about six peptides segments per fold, and the changes in the degree of ordered phase in spider silk would affect its final mechanical properties. This behavior can be predicted based on this model using the mean field theory for polymers. The above two models emphasize mainly the hierarchical structure of silks in the molecular scale.

Longer-range organizations, nano-silk fibrils, are observed in both spider silks and silkworm silk.

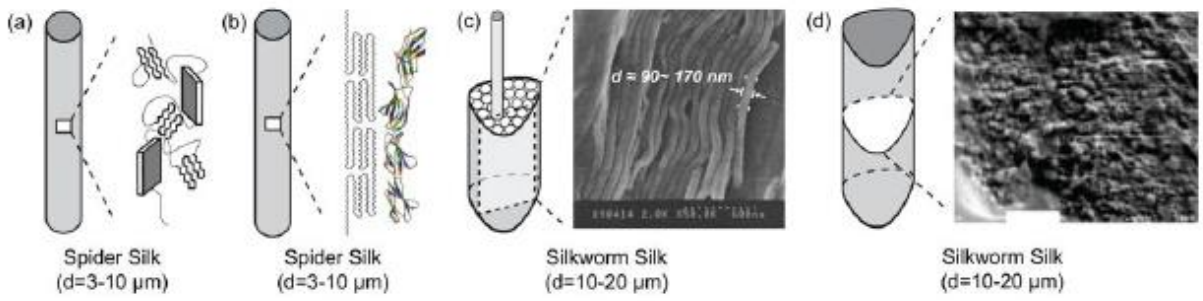

Figure 2.3. Different structural models for silks. (a). Semi-crystallite model for spider dragline silk. Highly oriented (rectangles) and weakly oriented (canted sheet-like structures) crystallite regions are embedded in the non-crystallite matrix (curved lines). (b). String of beads model for spider dragline silk. The molecular structure in silks for "string of beads" model is suggested to be a folded hairpin structure. (c). Fibrillar morphology of peeled B. mori silk. The diameter of the fibrils is around 90~170 nm. (d). Micellar structures observed in fractured surface of silkworm silk fiber. It is thought that fibrillar structure is formed by the coalescence of micelles during shear condition.

It is expected that the mechanical properties of silk fibers will critically depend on the characters of β-sheet crystallites, significant properties include crystallinity, size (aspect ratio, distribution) and dispersion of β-sheet crystallites, the inter-crystallite distance, and the degree of orientation in the silk fiber. The size of β-sheet crystallite in B. Mori silk fiber, determined via quantitative examination of the dark field TEM images, were revealed to be 20

to 170 nm in the axial direction and 1 to 20 nm in the lateral direction (Figure 2.4) and all the crystallites were uniformly distributed in the whole fiber matrix (X. Liu et al.).

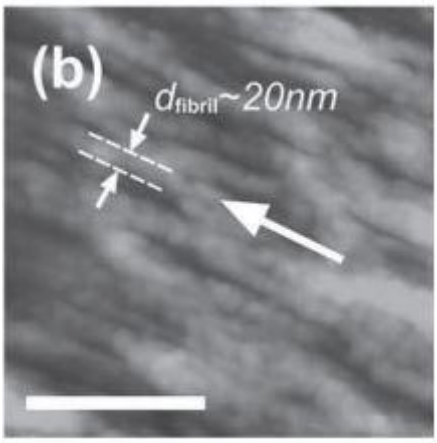

Figure 2.4. The minute fibrils in silkworm B. mori silk as revealed in an AFM image (scale bar: 150 nm). The silk fiber direction is indicated by the arrow. (X. Liu, 2014)

This fibrillar model explains the remarkable properties of silk fibers from another point of view: interaction between the nano-silk fibrils can efficiently dissipate energy and prevent crack propagation, thus enhancing the strength of silks.

The non-crystalline regions are often described as amorphous, poorly orientated, or randomly coiled sections of the peptide. The structural organization in the amorphous phase is not well understood yet. The existence of β-turn or β-spiral and helical conformations has been suggested for amorphous domains (Asakura T. 2002). The molecular chains in the amorphous phase are often considered to be randomly oriented. Studies from Raman (Lefèvre T., 2007) reported that the protein backbones in the amorphous regions of silk fibers are actually not randomly oriented but exhibit certain degree of orientation along the fiber axis, albeit much less oriented than β-sheet crystallites. Meanwhile, the higher level of orientation of the amorphous phase for the spider silks than that for B. Mori silk.

The density of hydrogen bonds in amorphous regions is lower than in β-sheet crystallites (Keten S., 2010). All of the results are excellently consistent with available experiment evidence and may contribute towards an improved understanding of the source of silk's strength and toughness. According to the prevalent characterizations mentioned above, silk fiber is considered a semicrystalline polymer with a hierarchical structure in which highly

oriented β-sheets crystallites connecting with an amorphous matrix are organized in nanofibrils or fibrillar entities (Du N., 2011). However, it has been proposed that there exists a third phase, or interphase consisting of weakly oriented β-sheets regions or oriented amorphous domains in silk (Sirichaisit J., 2003).

2.3 HOW TO INVESTIGATE SILK PROPERTIES

2.3.1 STRUCTURAL CHARACTERIZATION

2.3.1.1 Fourier Transform Infrared Spectroscopy (FTIR)

FTIR is a technique which is applied to obtain the infrared spectrum about the molecular vibrational and rotational information. The principle is that when the bonds between atoms in the molecule stretch and bend, they will absorb the infrared energy and create the infrared spectrum. Since the bonds formed from different atoms have distinct vibration frequencies, the created infrared spectrum can therefore be seen as the fingerprint of the molecules and used for identification and analysis. Comparing to an obsolete dispersive spectrometer, an FTIR spectrometer is able to collect spectral data in a wider range and much shorter time. The core structure of FTIR spectrometer is the interferometer. The interferometer usually employs a beamsplitter to divide the incoming infrared beam into two optical beams: one reflects off a fixed flat mirror, while the other reflects off a moving mirror. The two beams are combined when they transfer back to the beamsplitter before passing through the samples. The two beams have different phase and will interfere with each other. Since the moving mirror keeps changing its position, the resulting combined beam (interferogram) has information of every infrared frequency which is directly corresponding to the position of the moving mirror. In this way, all the frequencies can be measured simultaneously and thus can greatly reduce the time for experiment compared to the dispersive spectrometer. Finally, the measured interferogram will undergo the Fast Fourier transformation (FFT) by the computer to obtain the frequency spectrum which is used for later analysis and identification (Figure 2.5).

Figure 2.6 shows NUS (National University of Singapore) FT-IR Bruker IFS 125HR spectrometer (left) and tight silk fiber sample attached on a gold high reflective substrate (right).

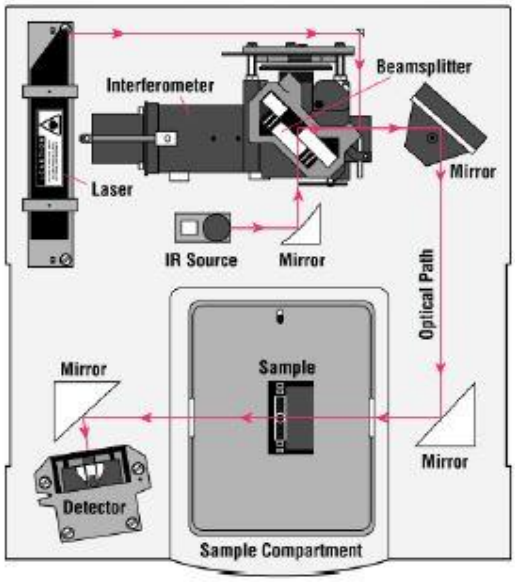

Figure 2.5. Schematic illustration of the FTIR spectrometer

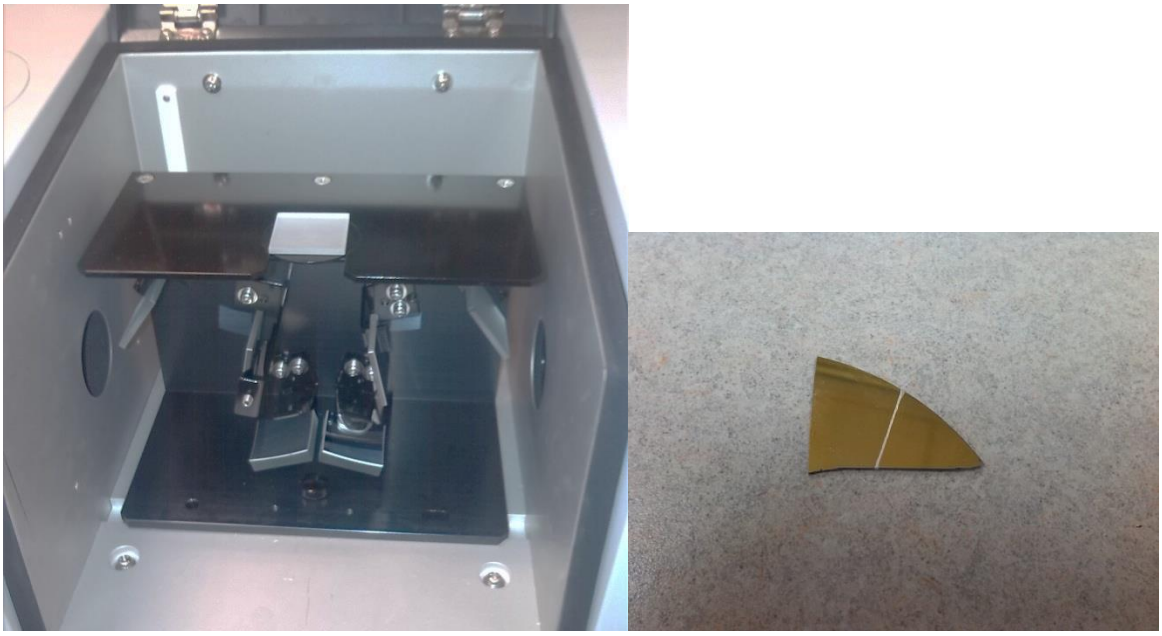

Figure 2.6. NUS (National University of Singapore) FT-IR Bruker IFS 125HR spectrometer (left), tight silk fiber sample attached on a gold high reflective substrate (right)

2.3.1.2 X-Ray Diffraction (XRD)

XRD is a common technique that is used to determine the crystalline structure and the crystallinity in biomarcromolecules or polymers. The crystalline phase in the biomarcromolecules or polymers has distinct Bragg peaks arising from the diffraction of the X-ray. By applying the Scherrer Equation as well as the curve-fitting process to the diffraction spectra, we can obtain the general structural information on the crystalline phase of the biomarcromolecules or polymers, i.e., the unit cell parameters, the crystalline size and the crystallinity and etc.

The basic experimental setup for XRD is shown in Figure 2.6. The rotating anode generates the X-ray beam of a characteristic wavelength which passes through the biomarcromolecules or polymers, the crystalline phase can cause diffraction the X-ray beam and the resulted diffraction profile is then recorded by the CCD (charge-coupled device) detector.

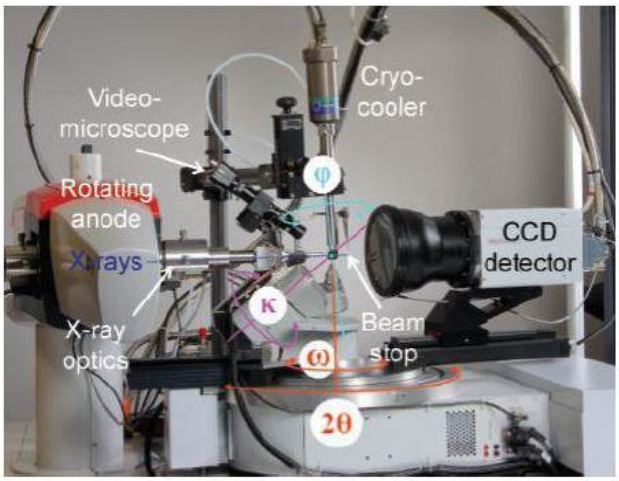

Figure 2.7. Experimental setup of XRD machine

Figure 2.8: Bragg Brentano diffractometer at NUS laboratory (Singapore) (left). Sample preparation before XRD analysis (right).

2.3.2 MECHANICAL CHARACTERIZATION

Mechanical characterization of silk fibers has been performed by means of uniaxial tensile tests. Elastic modulus as well tensile strength can be easily assesses through this technique. Toughness or energy at break has also been estimated.

Mechanical tensile test were performed by a microtensile equipment provided by NUS laboratories. Figure 2.9 shows micro tensile machine used at NUS laboratories (left) and sample preparation before tensile uniaxial test (right).

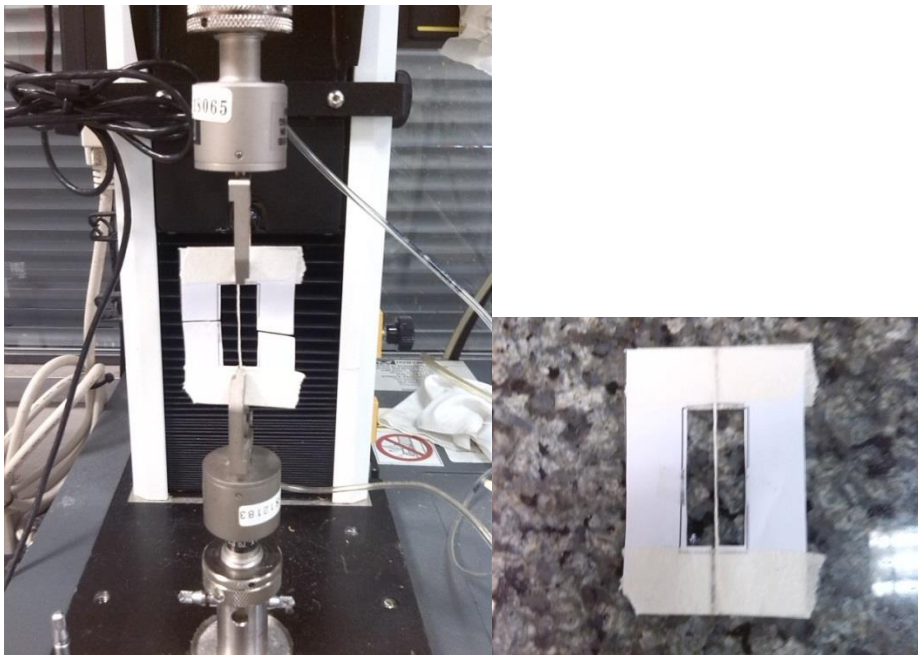

Figure 2.9: Micro tensile machine used at NUS laboratory (Singapore) (left). Sample preparation before uniaxial tensile test (right).

2.3.3 ELECTRICAL CHARACTERIZATION

Electric resistivity (or conductivity) of a fiber can be measured in the most basic scheme using either two or four probe techniques. The electrical response of fibers is strictly dependent on temperature and humidity change, so that several tests were performed with the silk sample inside an humidity chamber.

The resistivity of a material can be obtained by measuring the resistance and physical dimensions of a sample of a proper length l, and a proper cross section. Conductive wires are attached to both ends of the sample. This is called the two-point technique, since wires are attached to the material at two points. A voltage source applies a voltage V across the sample, causing a current I to flow through the sample. (Alternatively, a current source the voltage induced across the sample.) The amount of current I that flows through the sample is measured by the sourcemeter, which is connected in series with the bar and voltage source. The voltage drop across the ammeter should be negligible. An alternative could be four point probe technique but in this work was used two point technique.

All the measurement were conducted in a humidity and temperature chamber in order to measure how this parameter could change the electrical properties in doped silk fibroin.

2.5.4 THERMAL CHARACTERIZATION

Differential scanning calorimetry is a thermoanalytical technique in which the difference in the amount of heat required to increase the temperature of a sample and reference is measured as a function of temperature. Both the sample and reference are maintained at nearly the same temperature throughout the experiment. Generally, the temperature program for a DSC analysis is designed such that the sample holder temperature increases linearly as a function of time. The reference sample should have a well-defined heat capacity over the range of temperatures to be scanned.

DSC is used widely for examining polymeric materials to determine their thermal transitions. The observed thermal transitions can be utilized to compare materials, although the transitions do not uniquely identify composition. The composition of unknown materials may be completed using complementary techniques such as IR spectroscopy. T_m and T_g for most polymers are available from standard compilations, and the method can show polymer degradation by the lowering of the expected melting point, T_m, for example. T_m depends on the molecular weight of the polymer and thermal history, so lower grades may have lower melting points than expected. The percent crystalline content of a polymer can be estimated from the crystallization/melting peaks of the DSC graph as reference heats of fusion can be found in the literature.

2.4 PROPERTIES OF SILK

2.4.1 STRUCTURAL PROPERTIES

Fibroin protein consists of 5263 residues. The primary structure of *Bombyx Mori* silk consists of 12 repetitive regions called crystalline regions and 11 non repetitive interspaced regions called amorphous regions. The composition of various amino acids in fibroin is 45.9% glycine, 30.3% alanine, 12.1% sericine, 5.3% tyrosine, 1.8% valine and 4.7% other remaining amino acids (M. R. Gandhi, 2006).

The crystalline regions make up 94% of the sequence and each repetitive region is an average 413 residues in length. The majority of the repetitive region is made up of hexapeptides repeats. These are GAGAGS, GAGAGY, GAGAGA and GAGYGA (Figure 2.10).

The repeat GAGAGS is the most frequently (70%) occurring hexapeptide repeat sequence. The crystalline repetitive region is responsible for the secondary structure (antiparallel β-pleated sheets) of the protein. Each crystal is on an average made up of 4 individual β strands each 11 amino acids long. The β strands are connected to one another by β-turn made up of GAAS amino acids (see 2.3 section). The amorphous regions consist of 42-43 residues and are linkers between repetitive domains. The primary sequence of heavy chain also contains header (151-residue) and C Terminal (58-residue) sequences.

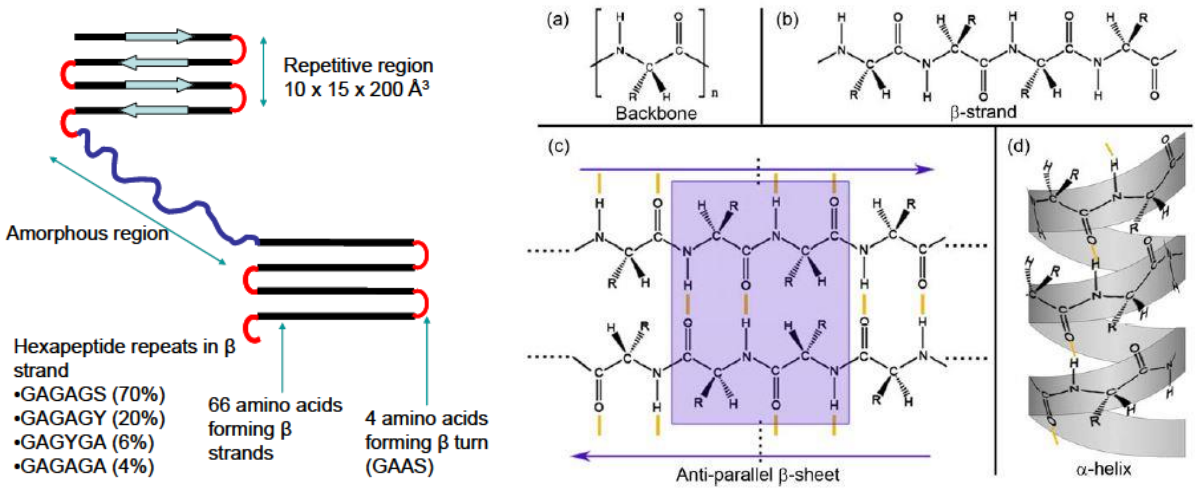

Figure 2.10. The schematic of structure of *Bombyx Mori* silk fibroin protein. The primary structure consists of 12 repetitive regions interspaced by 11 non-repetitive regions. The repetitive region is responsible for the formation of β-sheets crystals of size 10x15x200 Å^3. The non-repetitive region forms the amorphous part of the protein (M. R. Gandhi, 2006).

2.4.2 MECHANICAL PROPERTIES

Silk fibroin is a biomaterial with high elasticity, toughness, crystallinity, strength, and resistance to failure in compression. The semi-crystalline regions are the basis for the protein's elasticity. The basis for silk's unique mechanical properties is the combination of the β-sheet crystals and the inter phase between the crystals and the semi crystalline region.

In general the properties of silk are due to the extensive hydrogen bonding, hydrophobic nature of protein, and significant crystallinity. Silk is insoluble in most solvents, including water, dilute acid or dilute alkaline solutions. The elastic modulus of Bombyx mori silk is 15-17 GPa and has a tensile strength of 610-690 MPa while spider silk has strength as high as 1.75 GPa at a breaking elongation of over 26% (M. R. Gandhi, 2006).

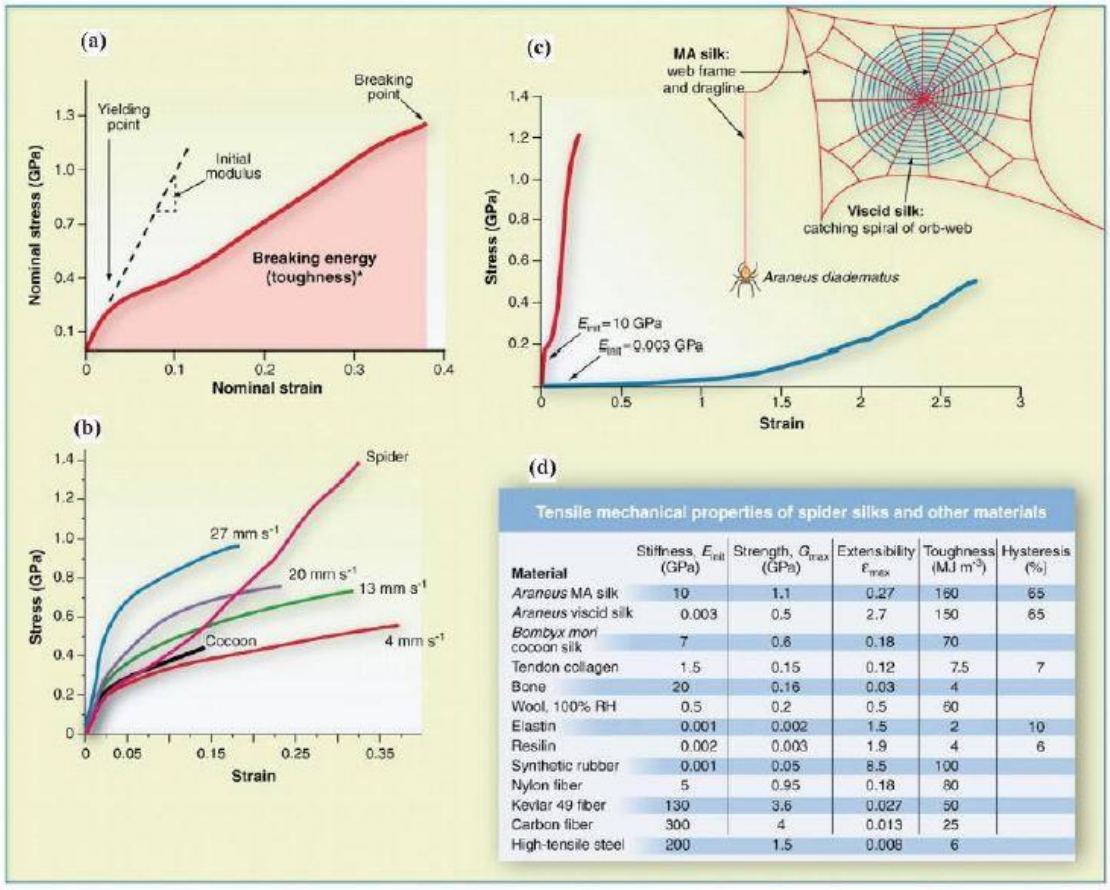

Material	Stiffness, E_{ini} (GPa)	Strength, σ_{max} (GPa)	Extensibility ε_{max}	Toughness (MJ m^{-3})	Hysteresis (%)
Araneus MA silk	10	1.1	0.27	160	65
Araneus viscid silk	0.003	0.5	2.7	150	65
Bombyx mori cocoon silk	7	0.6	0.18	70	
Tendon collagen	1.5	0.15	0.12	7.5	7
Bone	20	0.16	0.03	4	
Wool, 100% RH	0.5	0.2	0.5	60	
Elastin	0.001	0.002	1.5	2	10
Resilin	0.002	0.003	1.9	4	6
Synthetic rubber	0.001	0.05	8.5	100	
Nylon fiber	5	0.95	0.18	80	
Kevlar 49 fiber	130	3.6	0.027	50	
Carbon fiber	300	4	0.013	25	
High-tensile steel	200	1.5	0.008	6	

Figure 2.11. Mechanical properties of silks (a) Typical stress-strain profile of spider dragline silk. The area under the curve shown indicates fiber toughness or the energy taken up by the material before breaking. (b) Comparison of *B. mori* silks drawn at different speeds with *Nephila* spider dragline silk. (c) Stress strain curves for major ampullate (MA) gland silk (red line) and viscid silk (blue line) from the spider *A. diadematus*. (d) Mechanical properties of the dragline silks from spider *A. diadematus* and other materials.

The complex and ingenious design in the hierarchical structures of silks leads to the remarkable properties of silks. The excellent combination of the mechanical strength and elasticity render silks, especially the spider dragline silks, outperform any of the best synthetic fibers available today (Figure 2.11)

Besides, some unique properties are found for the spider dragline silks, i.e. super-contraction, the torsional shape-memory effect, the high energy adsorbent with low impact force as well as the non-linear response to stress (Wu Xiang, 2010).

Chemical modification and atomic layer deposition (ALD), were utilized to infiltrate the zinc, titanium, or aluminum, combined with water into the spider dragline silks. (Lee et al, 2009). This gives rise to 3 times increase of the strength and 5-7 times increase of the toughness

compared to the natural silks. Some researchers have also studied the effect of temperature on the mechanical performances of the spider dragline silks and find out that decreasing the temperature influences the mechanical properties of silks in the similar way as increasing the strain rate, indicating that silks are viscoelastic materials.

2.4.3 ELECTRONIC PROPERTIES

Silk is naturally an insulator in the neat state; Despite this recent works (B. Tulachan et al. 2014) documented the flow of current across silk fibroin and silk membrane, but is not very clear yet the origin of the charge moieties, which resulted in current flow. For the membrane was proposed that the silk fiber with its inner core of fibroin and outergummy layer of sericin is functioning like n and p type semiconductor material (Fig 2.12). Mineral analysis data highlighted the presence of common elements like Mg, P, S, Cl, K and Ca in the silk cap, and was assumed that these minerals are acting as natural dopants in silk-semiconductor material.

It would be interesting to investigate the humidity and temperature dependent electronic properties of silk fibroin in order to figure out the possible origin of the charge carriers within the backbone of the macromolecule and the type of electrical conduction, which might be responsible for triggering current flux.

Recent experiment have observed that, when a silk membrane is doped with common salt solution (1 M NaCl solution), it results in maximum current flux measurement respect to other kind of modification (B. Tulachan et al. 2014).

Further, in the absence of humidity, no significant current was measured across fibrous protein matrix. These observations, slims down the chances of electronic conduction, instead raised the possibility of some form of ionic conduction across the membrane. One of the possibilities could have been that, when silk fibroin is exposed to moisture and water vapor, the water molecules diffuses into its porous matrix, becomes mobile, and interact with the common ion forming elements like Na, K, Cl as well as with the protein matrix and resulting in the generation of charged ionic species, that might generate electricity. The mobility of the water molecules could be further modulated by temperature.

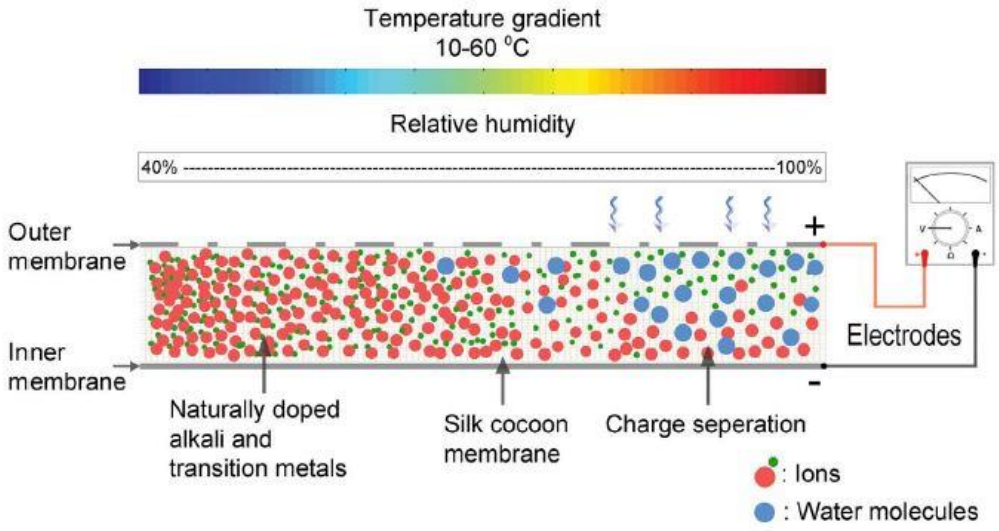

Figure 2.12.The proposed model showing the mechanism of current flow across silk membrane. In the absence of relative humidity (RH), there is hardly any current flow across silk membrane. As surrounding RH and temperature is increased, water molecules get trapped in the pores of silk cocoon membrane (SCM), and interact with the protein backbone and with certain naturally occurring ion forming elements, which possibly causes charge mobilization, resulting in the observed current (B. Tulachan et al. 2014).

2.4.4.THERMAL PROPERTIES AND DEGRADATION BEHAVIOR

Although there has been much research done on the physical properties and degradation behaviour of silk fiber, there still remain some unanswered questions. In particular, the behavior of silk fibers that have been subjected to heat treatment needs to be studied. Thermal properties of *B. Mori* cocoon may be studied by differential scanning calorimetry (DSC), thermogravimetric analysis (TG), differential thermal analysis (DTA), and the inorganic compositions of cocoon ashes using an energy dispersion X-ray fluorescence spectrometer.

Fibroin films were reported to experience more significant degradation than fibers. Methanol treatment is the most used technique to enhance stability and mechanical properties and it may significantly reduce the rate of degradation (S. Prasong, 2010). The potential to manipulate the rate of degradation is important for tissue engineering applications, and control over the physical form and post-treatment of a silk biomaterial may allow tailoring of the degradation; The crystalline, hydrophobic β-sheet domains prevent the penetration of water and proteases resulting in slow biodegradation of silk in vivo.

Moisture exerts a significant, and often deleterious, effect on the physical properties of polymers. Films and fibers of regenerated *Bombyx Mori* silk are strongly affected by absorbed moisture, a phenomenon studied by DSC;

2.5 EXISTING AND POTENTIAL APPLICATIONS

the unique balance of material properties, i.e. good tensile strength, extensibility, and the energy absorbing capability, is the principle driving force behind of continuing interest in silk engineering.

The quality of silk is highly dependent on the species, the living environment, as well as the food the silkworm takes. The spider silk, attributed to its extraordinary mechanical properties, has been more and more attractive for its various potential applications. As widely known, silkworm silk was firstly initiated to for costume industry. The Silkworm silk's absorbency makes it comfortable to wear in warm weather and while active, and its low conductivity keeps warm air close to the skin during cold weather. The costume manufacture family includes the clothing such as shirts, ties, blouses, formal dresses, high fashion clothes, negligees, pajamas, . The silk industry, referring to the aspect of costume manufacture is still flourishing nowadays, and it will continue to be an irreplaceable stay of the social economy in the foreseeable future.

Due to the high strength and extensibility, silks can be made into ropes and cables, which outperform the ones fabricated by nylon. One example is the high extensibility and possibility of encoding saltwater protection into a silk-based fibrous material. Besides, the strength combined with the light weight of silk fibers may arise the substitution of fish net/cable material, as well as a new generation of parachutes, gliders or sailing boats. The dyed silk, which has been demonstrated in conventional textile silk industry though technically it has yet been popularized, has great advantages to other man-made costume materials.

In recent decades, thanks to the development of the degumming technique, the biocompatibility and bio-degradability were recognized of silk fibroin which is the primary component under the sericin coating. Altman *et al.* (F. Altman, 2013) reviewed the bio-medical applications of silk from 1990s onwards. Among those newly developed biomedical applications, one of the most popularized applications is surgical suture. Besides, silk matrices

are now being rediscovered and reconsidered (due to the technique of sericin removal which recovers the biocompatibility of silk) as potentially useful biomaterials for a range of applications in clinical repairs and in vitro as scaffolds for tissue engineering.

High-tech applications of silks do not fully rely on the strength and toughness of silks. For instance, supercontraction is one specific property of spider dragline silk, and this may make impact on sensitive impact systems. The absence of the kink-band structure of silk which leads to a high compressive strength may apply to certain structural components to prevent impact damages.

Function silks are nowadays popularized by coating, depositing or penetrating nano-sized clusters or particles onto the silk/silk fibroin film surface or into their fibrillar structures, such as TiO2, TiO2/Ag and FePt nano-particles. (W. Xiang, 2010).

Lotus effect with super hydrophobicity has been achieved by profileing the silk fibroin film analogous to the lotus leaf. Enhancement of luminescence have been acquired by nano-structured profileing by Ganesh and Zhang (A. Ganesh, 2009), and such dramatic increment of the luminescence density is purely caused by structural reason. In this sense, silk fibroin matrix turns out to be a kind of excellent profileing material for structure induced enhancement of luminescence and structure color.

Besides the uses as a biomaterial, silk fibers or thin film are good candidates in electronic and microelectronic field as well as in photonics; depending on the desidered application, we may change the properties of the silk, in order to achieve the maximum performance we want; for instance the insulator properties are essential if a thin film is used as gate dielectric in OFET, whereas degradation behavior has to be controlled if thin film is used as substrate for implantable and resorbable electrical device. As mentioned before have been used also many strategies to improve conductivity; blending fibers with conductive polymer such us PEDOT:PSS is one of the most used in laboratory, but this blend limits the possibility to use these fibers in biomedical application (C. H. Wang, 2011).

Single-component, metal-free, biocompatible, electromechanical actuator devices were fabricated using a composite material composed of silk fi broin and poly(pyrrole) (PPy). Chemical modification techniques were developed to produce free-standing films with a bilayer-type structure, with unmodifi ed silk on one side and an interpenetrating network of silk and PPy on the other. The Interprenetrating network formed between the silk and PPy prohibits delamination, resulting in a durable and fully biocompatible device (Isabella S. 2014).

Despite this scarce effort have been made to improve electronic properties of silk fibroin and especially regarding the electrical conductivity properties.

Figure 2.13 summarizes some of the possible application starting from wide and versatile structure.

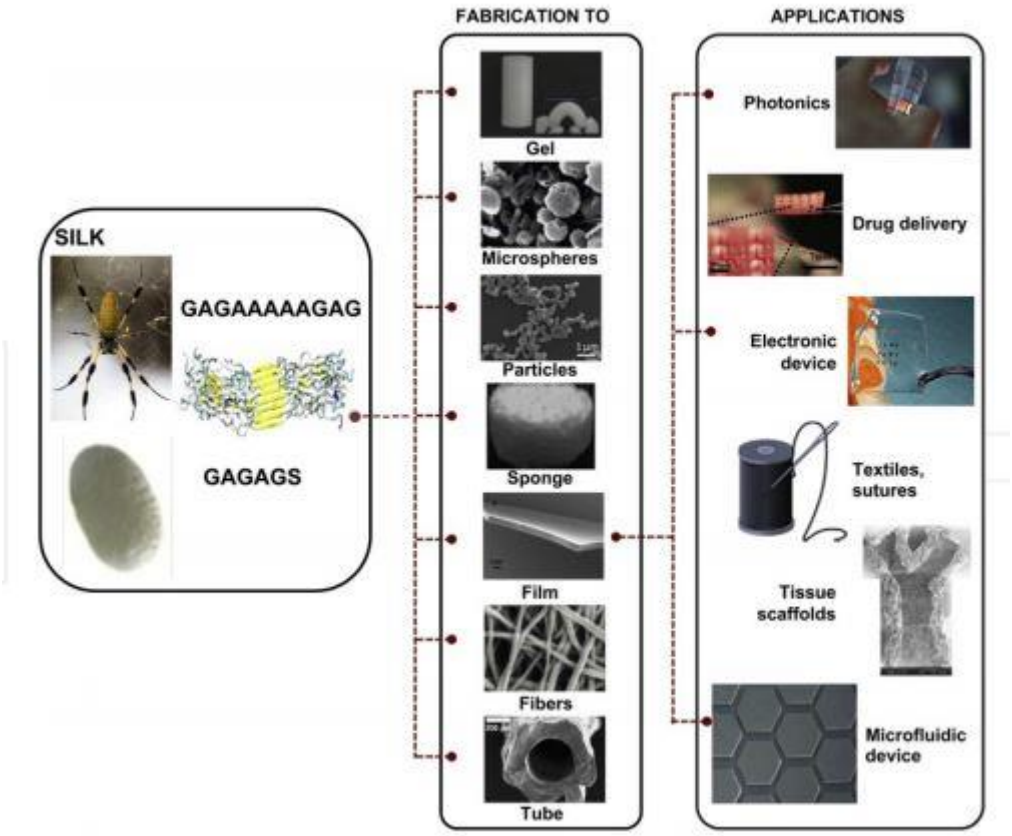

Figure 2.13 Possible structure and technical applications of the silk fibers. The dotted line shows an example of the versatility of silk and the multiple possible applications

REFERENCES

Amol R. Padol, K. Jayakumar, K. Mohan, Manochaya. Natural biomaterial silk and silk proteins: Applications in tissue repair. International Journal of Materials and Biomaterials Applications November 2012.

Asakura T., Yao J. 13C CP/MAS NMR study on structural heterogeneity in Bombyx mori silk fiber and their generation by stretching. Protein Science 2002; 11(11): 2706–2713

Brindan Tulachan, Sunil Kumar Meena, Ratan Kumar Rai, Chandrakant Mallick, Tejas Sanjeev Kusurkar, Arun Kumar Teotia,– "Electricity from the Silk Cocoon Membrane" Scientific Report, 2014.

Du N., Yang Z., Liu X Y., Li Y., Xu H Y. Structural origin of the strain-hardening of spider silk. Advanced Functional Materials 2011; 21(4): 772–778.

Hagn, F., et al., A conserved spider silk domain acts as a molecular switch that controls fiber assembly. Nature, 2010. 465(7295): p. 239-U131.

Isabella S. Romero , Nathan P. Bradshaw , Jesse D. Larson , Sean Y. Severt ,Sandra J. Roberts , Morgan L. Schiller , Janelle M. Leger , and Amanda R. Murphy. Biocompatible Electromechanical Actuators Composedof Silk-Conducting Polymer Composites. Adv. Funct. Mater. 2014, 24, 3866–3873

Keten S., Buehler M J. Atomistic model of the spider silk nanostructure. Applied Physics Letters 2010; 96(15): 153701–153703.

Lefèvre T., Rousseau M E., Pézolet M. Protein secondary structure and orientation in
Lotz, B. & Keith, H. D. Crystal structure of poly(L-Ala-Gly)II. A model for silk. I. (1971) J. Mol. Biol. 61, 201–215.

Milind Ramesh Gandhi. Silk Protein as a Biomaterial for Tissue Engineering Application: Theoretical and Experimental Study, Thesis Submitted to the Faculty of Drexel University. December 2006.

Seung-Mo Lee, Eckhard Pippel, Ulrich Gösele, Christian Dresbach, "Greatly Increased Toughness of Infiltrated Spider Silk" ,Science 24 April 2009: Vol. 324 no. 5926 pp. 488-492
silk as revealed by Raman spectromicroscopy. Biophysical Journal 2007; 92(8): 2885–2895.

Simmons AH1, Michal CA, Jelinski LW. Molecular orientation and two-component nature of the crystalline fraction of spider dragline silk. Science. 1996 Jan 5;271(5245):84-7

Sirichaisit J., Brookes V L., Young R J., Vollrath F. Analysis of structure/property relationships in silkworm (Bombyx mori) and spider dragline (Nephila edulis) silks. Advanced Functional Materials 2011.

Steven, Eden, "Physical Properties Of Organic And Biomaterials: Fundamentals And Applications" (2012). Electronic Theses, Treatises and Dissertations. Paper 5443.

Vollrath F. and Porter D (2006a). V. Kearns, A.C. MacIntosh, A. Crawford and P.V. Hatton. Silk-based Biomaterials for Spider silk as a model biomaterial. Applied Physics A Material science & processing 82(2). 205-212

Wu Xiang "physical mechanism of silk strength and design of ultra-strong silk". Thesis submitted by National University of Singapore (NUS), 2010.

Xinfang Liu and Ke-Qin Zhang, Silk Fiber Silk Fiber — Molecular Formation Mechanism, Structure-Property Relationship and Advanced Applications. http://dx.doi.org/10.5772/57611 chapter 3

Yang, Z., D.T. Grubb, and L.W. Jelinski, Small-angle X-ray scattering of spider dragline silk. Macromolecules, 1997. 30(26): p. 8254-8261.

Yu Shen , Michael A. Johnson , and David C. Martin. Microstructural Characterization of Bombyx mori Silk Fibers. Macromolecules, 1998, 31 (25), pp 8857–8864. November 12, 1998

Chapter3: SAMPLE PREPARATION

3.1 INTRODUCTION

Degummed silk fiber can be used directly for applications such as sutures or ligament engineering, but SF is more commonly used in the regenerated form. Silk fibers can be dissolved at elevated temperatures (60–80 °C) in several aqueous solutions including concentrated lithium bromide, lithium thioisocyanate, or a mixture of $CaCl_2$:water:ethanol (in a 1:8:2 molar ratio) then dialyzed into water to give aqueous silk solutions that can be processed into films, fibers, gels or 3D porous structures (M. K. Sah, 2010).

Either in the native or regenerated form silk fibroin can be modified using different chemical reactions or techniques; Murphy A. R. and Kaplan D. L. have summarized most of them in a review paper and among all the most important are cyanuric chloride-activated coupling, carbodiimide coupling, sulfation of tyrosine, azocompound grafting of tyrosine, polymethacrylate grafting, and other (A. R. Murphy, 2009).

Many of these reactions are specially designed for the purpose biomedical applications such as coatings for 2D-cell cultures or drug delivery. On the contrary modification that we are going to discuss are designed to change properties and structure of the silk fibroin and not to give a specific functionalization.

In this chapter we are going to discuss three different way to modify silk fibers after a proper degumming. Degumming of silk is a well-known treatment achievable in different solutions but with the common aim to remove the sericin coat from the silk surface of fiber; removing the gum improves the sheen, color, hand, and texture of the silk but in particular sericin has been found to illicit inflammatory responses in vivo (D. N. Rockwood et al. , 2013).

3.1 DEGUMMING OF SILK

Degumming is the process of the cleavage of the peptide bond of the sericin by hydrolytic or enzymatic methods, and it is removed by solubilization or dispersion in water. For laboratory purposes are common five method using respectively distilled water, boracic acid–sodium borate buffer, sodium carbonate, urea and succinic acid (M. D. Teli et al., 2011).

In this work we used sodium carbonate (Na_2CO_3) and a surfactant (sodium dodecyl sulfate, SDS) following this procedure: We pre-heated water in a glass beaker using the microwave

and bring the water to boil using a hot plate; We added the weighed sodium carbonate and sodium dodecyl sulfate (0.02 M each) to make a solution, than the silk fibers once the water begins boiling again. We rinsed the degummed silk in water 3-4 times, and finally dried the silk fibers overnight in vacuum. Quantity of removed sericin, expressed in % was obtained using following equation (3.1).

$$S = \frac{B - A}{B} \, x \, 100 \, [\%] \qquad (3.1)$$

where

S - amount of removed sericin [%],
B - mass of fibers before degumming [g].
A - mass of fibers after degumming [g].

In the following table were reported the results after Na_2CO_3/SDS degumming (Table 3.1).

Silk hank n°.	**1**	**2**	**3**	**4**	**5**	**6**	$\overline{X}$
Mass (g)	7,414	7,80	6,881	7,425	6,654	7,558	7,29
Mass after degumming (g)	5,650	5,992	5,315	5,641	5,130	5,784	5,59
Sericin content (%)	23,79	23,20	22,83	24,02	22,89	23,47	23,37

Table 3.1: Total amount of removed sericin from each hank of silk. $\overline{X}$ refers to the average

3.3 SILK FIBER DOPING

Recent studies (A. R. Murphy et al., 2009) have been proposed different physical and chemical method to improve the properties of silk fibers or silk film. The useful features of the proteins,

including self-assembly, robust mechanical properties, biocompatibility and biodegradability can be enhanced through a variety of chemical modifications.

In this work we propose three different modification methods to dope silk fibroin in order to study how mechanical, structural, thermal and electric characteristics can change after the treatment.

3.3.1 IODINE MODIFICATION

The iodine treatment of silk fiber was performed by the following procedure: the degummed fiber was dried in a oven, and the weight was measured in dry condition. Then the fiber hunk was enclosed with an adequate amount of iodine in a glass beaker. After sealing the glass beaker, it was placed in an oven heated at 100 °C, where iodine was vaporized and kept for several periods. After the treatment, the color of fiber turned to dark brown. Finally, the weight of iodinated samples was measured again. The iodine absorption percentage was calculated by measuring the weight change of the fibers before and after the iodine treatment.

To study the effects of I_2 doping on silk fiber, two iodine doping conditions were used, namely light and heavy I_2 doping based on time of exposure.

Lightly I_2 doping was done by placing the neat silk fibers together with solid I_2 chunks for 24 hours at room temperature. For heavy I_2 doping, the silk fiber was further exposed to I_2 vapor at 70 °C for 2 h (total 26 hours). The resulting silk fiber had a permanent deep-brown color.

To monitor the absorption of I_2 vapor were also been done weight measurements during the exposure of the doping agent.

In the Figure 3.1 we can see how iodine changed silk color during the treatment.

Figure 3.1. Silk fiber during iodine vapor treatment. After 3 hours (left), after 5 hours (middle), after 26 hours (24 hours at room T and another 2 hours at 70° inside a woven) (right).

3.3.2 $CaCl_2$ MODIFICATION

The following procedure was used to modify silk fibroin with $CaCl_2$: degummed silk fibers were immersed in 100 mL of a calcium chloride solution ($CaCl_2$/H2O) with different M of $CaCl_2$ (respectively 0,5 M / 1 M / 1,5 M) and left at 70°C for a given time (10 minutes for 0,5 M and 1 M calcium chloride solution, 10 min and 2 hours for 1,5 M solution).
Then, the silk fibers was added to a 5% ethylene diamine tetra-acetic acid solution and heated at 100°C for 5 min to remove remaining calcium ions did not penetrated in the matrix. The collected fibers were washed extensively with deionized water and dried in vacuum at 60 °C for 24 h. The weight loss of sample was calculated according to the difference in weight before and after treatment.

3.3.3 KBr MODIFICATION

Degummed silk fibers were immersed in 100 mL of a potassium bromide solution (KBr/H2O) with different molarity of KBr (respectively 0,5 M / 1 M / 1,5 M) and left at 70°C for a given

time (10 minutes for 0,5 M and 1 M calcium chloride solution, 10 min and 2 hours for 1,5 M solution).

The main difference between the two salts treatments was the weight loss: $CaCl_2$ treated silk fiber presented lager amount of weight loss after the treatment (see 3.3.4 section), on the contrary the appearance of both the hank was the same.

Figure 3.2. Silk hunk rolled to a plastic container during KBr treatment

3.3.4 RESULTS AND DISCUSSION

First considerations we should do after the treatments are related to weight lost or gained: After either calcium and potassium salt treatment we noted a reduction in weight of the silk fiber for all concentration of $CaCl_2$ and KBr used. Figure 3.3 presents weight lost after different time intervals for both salts doped fibers at 1,5M and 2 h of treatment.

We can firstly suppose that a porous, or better micro-porous, structure was formed inside the matrix (this hypothesis will be supported by most of the further characterizations).

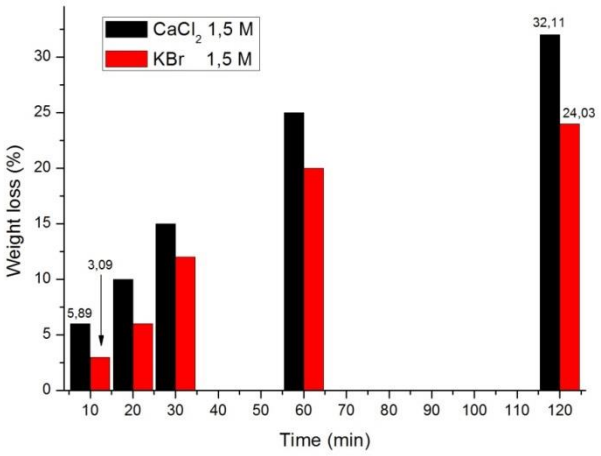

Figure 3.3. Weight loss of 1,5M calcium/potassium salt treated silk fiber

On the contrary after Iodine treatment we noted a sharp weight increase in the firsts 15 hours and then the achievement of a maximum after 24 hours. This suggests us that the absorption of iodine vapor reaches a saturated condition after around 15 hours (Figure 3.4).

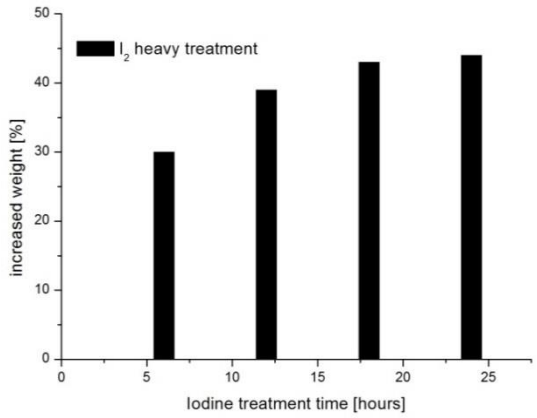

Figure 3.4. Increased weight after heavy iodine treatment

REFERENCES

Danielle N. Rockwood, Rucsanda C. Preda, Tuna Yücel, Xiaoqin Wang, Michael L. Lovett, and David L. Kaplan. Materials Fabrication from *Bombyx mori* Silk Fibroin. NIH public access resources, Oct 2013.

M. K. Sah and K. Pramanik. Regenerated Silk Fibroin from B. mori Silk Cocoon for Tissue Engineering Applications. International Journal of Environmental Science and Development, Vol.1, No.5, December 2010.

Mangesh D. Teli, Vaishali M. Rane. Comparative Study of the Degumming of Mulberry, Muga, Tasar and Ericream Silk. FIBRES & TEXTILES in Eastern Europe 2011, Vol. 19, No. 2 (85).

Chapter 4: CHARACTERIZATION OF MODIFIED SILK FIBROIN

4.1 INTRODUCTION

In this chapter the results of several characterization are presented with the purpose of understanding the impact of the doping agent on the structure of the silk fibroin. In particular we discuss the results obtained with FTIR and XRD for what concerning the structural characterization, uniaxial tensile tests for mechanical characterization, conductivity measurements versus humidity and temperature for electrical characterization, and DSC for thermal and degradation behavior.

As discussed in the previous chapter we disposed of three different doped silk fiber (the numbers into the brackets refer to exposure time to the doping agent) (Table 4.1).

KBr doped	**$CaCl_2$ doped**	**Iodine doped**
KBr 0,5M (10 min)	$CaCl_2$ 0,5M (10 min)	I_2 lightly doped
KBr 1 M (10 min)	$CaCl_2$ 1 M (10 min)	I_2 heavily doped
KBr 1,5 M (10min)	$CaCl_2$ 1,5 M (10min)	
KBr 1,5 M (120min)	$CaCl_2$ 1,5 M (120min)	

Table 4.1. Different doping agent concentration and time of exposure used.

For all the 11 different kinds of doped fiber (11th is neat degummed silk fiber) we prepared a hunk of around 3 g each, starting from six hunks of degummed silk fiber (see section 3.1) to assure that there was enough silk to perform all tests. (for mechanical and electrical measurements have been performed at least 4 measurements).

4.2 STRUCTURAL CHARACTERIZATION

4.2.1 FTIR SPECTROSCOPY

4.2.1.1 INTRODUCTION

The shape of the Amide bands of globular proteins is characteristic of their secondary structure. With a publication by Byler & Susi (Biopolymers 1986 Mar;25(3):469-87) the determination of secondary structures in proteins from FTIR spectra actually started. This had become possible by the availability of high signal-to-noise ratio digitalised spectra obtained by the FTIR spectrometer and by the access to computers and software able to perform many operations on the spectra in a short time.

The concept of band deconvolution is based on the assumption, that a spectrum of single bands (each narrow band is characteristic for a secondary structure) is broadened in the liquid or solid state. Therefore, the bands overlap are not easily distinguished one from the another in the Amide envelope. A curve fitting procedure can be applied to estimate quantitatively the area of each component representing a type of secondary structure. In the pioneering work by Susi & Byler the Amide I was deconvoluted with a Lorentzian line shape function and a resolution enhancement factor of 2.4 was applied. The deconvoluted spectrum was fitted with Gaussian band shapes by an iterative curve fitting procedure. The results were in good agreement with the secondary structure information obtained from X-ray crystallographic structures of the proteins under study (Arrondo J.L. , 1993).

In this work the silk protein conformation and especially secondary structure was determined by FTIR spectroscopy. All the results will be compared with XRD analysis in order to better understand how silk protein can be changed under different treatments.
The spectra were collected using FT-IR Bruker IFS 125HR spectrometer and analyzed using Origin Lab 8.0.

Figure 4.1. shows the whole FTIR spectrum of neat silk fiber after degumming with emphasis on Amide I, II, III and relative wavenumber of interest. Figure 4.2 shows a magnification in the range of 1800-1400 cm^{-1} of the FTIR spectrum of neat silk fiber which includes Amide I and Amide II.

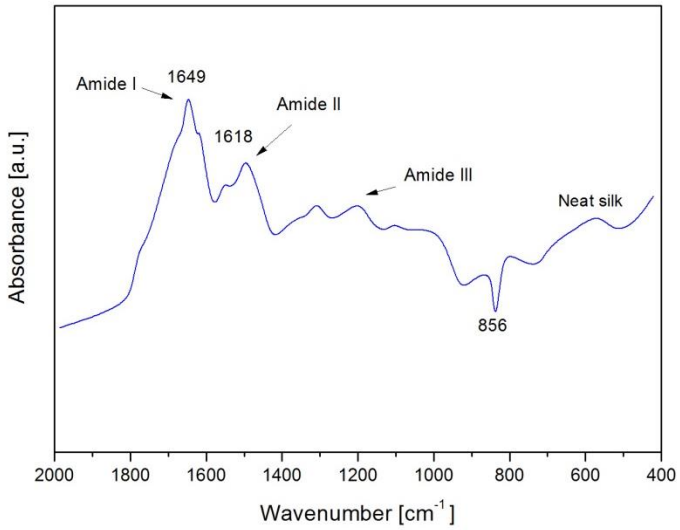

Figure 4.1. Neat silk FTIR spectrum in the range of 2000-400 cm^{-1}

Amide I peak at 1618 cm^{-1} represents antiparallel β-sheet or β-strand configuration (crystalline part), whereas peak at 1648 cm^{-1} can represents either random coil and helical structure (α-helix or 31 helix). At 1680 cm^{-1} is also present a peak attributable to β-turn conformation (related with an inter-main-chain hydrogen bond) (Fig 4.2).

We can find out the β-sheets content (%) in the fiber sample by calculating the areas under the curve of 1618 cm^{-1} and 1648 cm^{-1} peaks: this is the ratio between the area under the peak at 1618 cm^{-1} and the sum of the areas under the peak at 1618 cm^{-1} and 1648 cm^{-1} (eq. 4.2); Since the Amide I signals are partially overlapped, curve fitting and band deconvolution is required to determine a reliable information about sheets content. Hence the areas of selected signals can be obtained and sheets content can be determined through the following equation (4.1)

$$\beta sheet\ (\%) = \frac{Area_{1618}}{(Area_{1618} + Area_{1648})}\ x\ 100 \qquad (4.1)$$

Amide II present two different peaks at around 1552 cm^{-1} and 1496 cm^{-1} that correspond respectively to random coil (RC) and β-sheet.

The same procedure presented above can be used for the Amide II: The area under the peak at 1496 cm^{-1} divided by the sum of the area under the peak at 1552 cm^{-1} and 1496 cm^{-1} give us the percentage of β-sheet in the Amide II (eq. 4.2)

$$\beta sheet\ (\%) = \frac{Area_{1496}}{(Area_{1496} + Area_{1552})}\ x\ 100 \qquad (4.2)$$

Amide III presents two different peaks at around 1230 cm^{-1} attributable to random coil and one at 1280 cm^{-1} attributable to β-sheet.

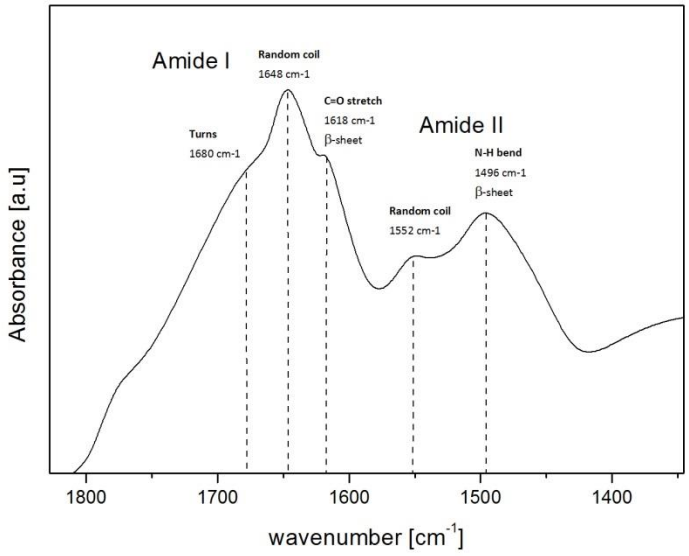

Figure 4.2: FTIR spectrum of neat silk fiber after degumming in the range of 1800-1400 cm^{-1}.

By monitoring the change of the absorbance around these peaks one can understand how the exposure to the doping agent can affect the secondary structure and the percentage of crystallinity in silk fibroin. In the following section are examined the modified sample spectra and has been added the spectrum of the neat profile (Fig 4.1) in order to better visualize the changes.

4.2.1.2 FTIR SPECTRA OF NEAT, LIGHTLY, AND HEAVY I_2-DOPED SILK FIBER.

To confirm and understand the conformational changes caused by the I_2 doping, we obtained the FTIR spectra of neat, lightly, and heavily I_2-doped silk (see Figure). For conformational study, Amide I region (arises from C=O stretching vibrations, 1600-1700 cm^{-1}) and Amide II region (arises from N-H in-plane bend and C-N stretching vibrations, 1500-1600 cm^{-1}) are the focus of study. This is because variations of side chains do not affect the vibrations in Amide I and Amide II regions. Instead, they depend on the arrangement of the protein backbone and the strength of the hydrogen bonding in a particular conformation. For example, multiple bands occur in the Amide I region with different frequencies which depends on the strength of hydrogen bonding in each type of conformations: intermolecular β-strands or β-sheets (1618-1635 cm^{-1}), α-helices (1649-1658 cm^{-1}), and turns (1665-1690 cm^{-1}). Similarly, Amide II region envelopes β-sheets and α-helices bands at around 1496 and 1550 cm^{-1}.

Several observations were made: doping at 70 °C (heavily I_2 doping) caused a major decrease in the content of β-sheets from 59% to 49% (Table 4.3) as indicated by the intensity decrease of the 1497 cm^{-1} peak (in Amide II) and 1618 cm^{-1} (in Amide I) bands. The intensity decrease in the β-sheet bands and the increase in the α- helix bands indicated that some of the β-sheets were destabilized and transformed into α-helices or random coils. The peak at 1649 cm-1 (α-helix) of the neat sample moved to 1658 cm-1 in the heavily iodinated one and this is a clear evidence of this transformation.

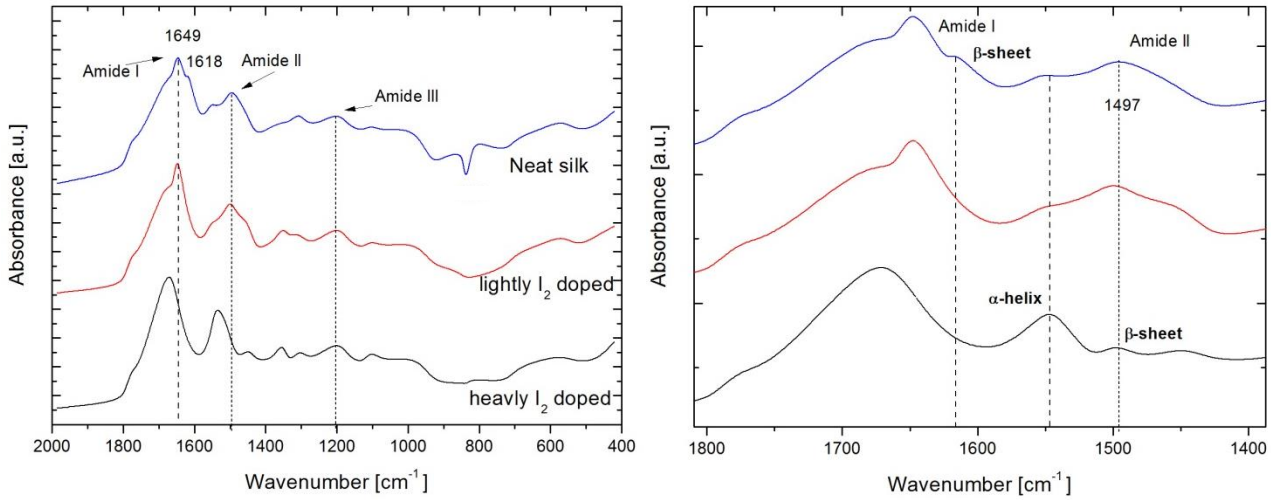

Figure 4.3. FTIR spectrum of iodinated silk fiber. (a) Comparison between neat, lightly and heavy I_2 doped silk fiber in the range of 2000-400 cm^{-1}. (b) Magnification of Amide I and II of neat and I_2 doped silk fibers.

In the following Table we report the obtained values of β-sheet content in neat and iodinated silk fibers based on the equation 4.1 and 4.2.

	β-*sheet Amide I*	β-*sheet Amide II*	β-*sheet Amide III*
Neat silk	59,03%	71,22%	---
Lightly I_2 doped silk	57,34%	70,44%	---
Heavy I_2 doped silk	49,98%	21,22%	---

Table 4.2. β-sheet content in the Amide I and II.

Considering heavily I_2 doped sample, It is likely that at 70 °C, there is a water-induced thermal glass-transition that enables chain mobility. At this temperature the water molecules act as plasticizers for the fiber. Hence, while at room temperature the iodine ions were mainly reaching the outer surface of the silk fibers, doping at 70°C allows diffusion through the intermolecular chains of the amorphous regions and maybe also the β-sheet. I_2 (possibly in multiple forms of anions and molecular iodine) initially trapped within the β-sheets regions made some of the β-sheets unstable, converting part of them into amorphous phases. The

FTIR spectrum point us that hydrogen bonding in the silk structure is partially suppressed by heavy I_2 doping.

No modification occurred in the Amide III part of the spectrum.

4.2.1.3 FTIR SPECTRA OF $CaCl_2$ DOPED SILK FIBER

In this section we discuss the structural changes of $CaCl_2$ doped silk fiber and all the conclusions have been made, even taking into consideration the weight loss after the treatment (Figure 3.3).

As discussed before the silk matrix is composed of crystalline microfibers, among which an amorphous region was present. We suppose that the coordination between the calcium ions and the polar lateral groups in the peptide chain destroyed the secondary bonds between the silk fibroin molecules, which resulted in the swelling and dissolution of the amorphous region; similar conclusion were made in another experiment in which Bombyx mori silks were modified by calcium-salt treatment and subsequent epoxy crosslinking with glycerin triglycidyl (Jianxin He, 2010).

The weight loss after calcium treatment is considerable (2,2% for 0,5M after 10 min; 3,6% for 1M after 10min; 5,89% for 1,5M after 10 min) and this fact suggest the formation of microporous structure within the matrix.

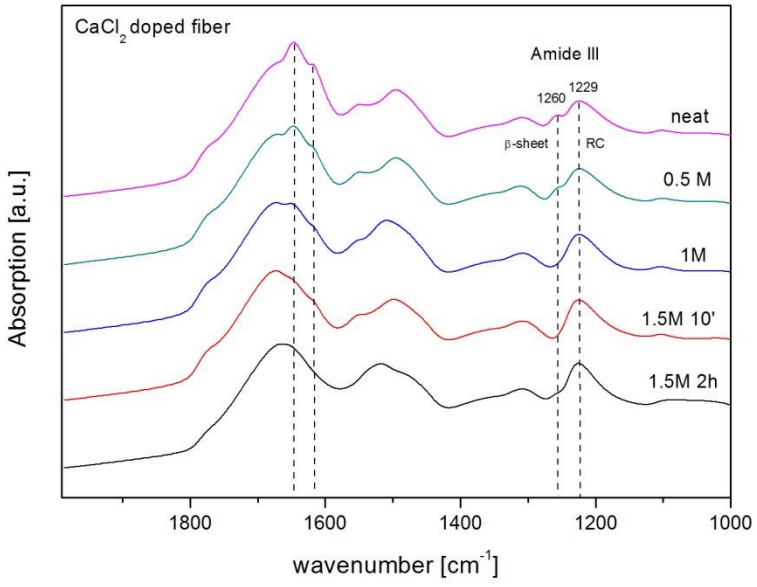

Figure 4.4. FTIR of different doped $CaCl_2$ fiber. Each line represent different concentration of the salt dopant whit the upper one that refers to the neat silk fiber

We can see from the FTIR graph that the peak at 1618 cm^{-1} in the Amide I (β-sheet) progressively decreases passing from neat to heavily doped fiber; even the 1496 cm^{-1} peak in Amide II decreases in intensity and this means that the β-sheet were partially diminished during the treatment. This trend is confirmed by watching the Amide III (C=N stretch): the shoulder peak at 1260 cm^{-1} decreased, whereas the peak at 1229 cm^{-1} increased; the former was assigned to β-sheet, and the latter was assigned to random coil.

In Figure 4.5 we can see the FTIR spectrum between 4000 and 2600 cm^{-1}; at 2965 cm^{-1} is evident an intensity decrease of the peak attributed to C-H stretching vibration and this could be explained by the change around the chain backbone due to salt ions: it is well know that bond vibrational frequencies and intensity can change depending to the environment, and in this case the presence of calcium or chlorine ions possibly caused a decrease of the vibration intensity.

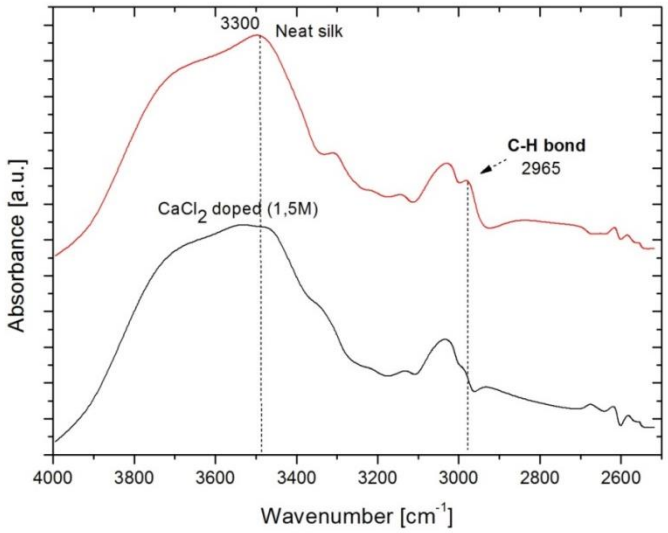

Figure 4.5. 4000-2600 cm^{-1} region of 1,5M $CaCl_2$ doped fiber spectrum: reduction of C-H intensity peak.

4.2.1.4 FTIR SPECTRA OF KBr DOPED SILK FIBER

The weight loss of the silk fiber after KBr treatment is considerably less with respect to calcium salt treatment (24 % for the former and 32 % for the latter, see Figure 9.) , and this point us that the dissolution of the silk matrix in the amorphous region is more difficult in this case (at equal concentration of doping agent); the result is a less porous structure (DSC measurements will confirm this hypothesis); the change in the Amide I is quite similar to the $CaCl_2$ case with the decreasing of the peak assigned to β-sheet; In the Amide II we can also see a slightly increase of the random coil peak at 1552 cm^{-1}.

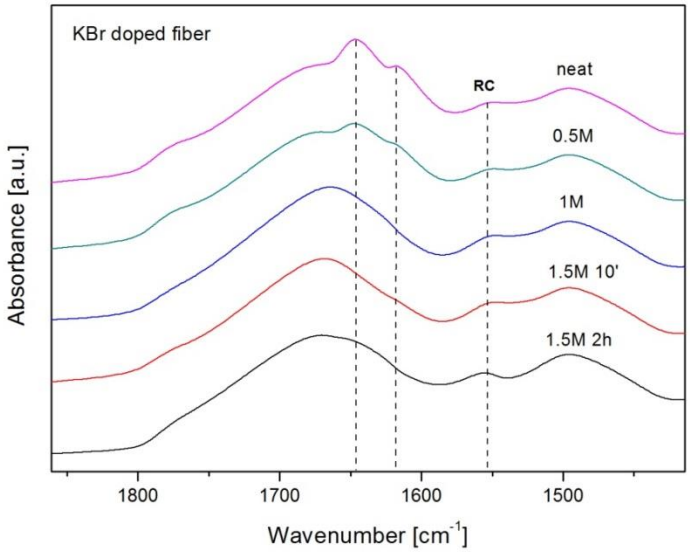

Figure 4.6. FTIR of different doped KBr fiber. Each line represent different concentration of the salt dopant with the upper one that refers to the neat silk fiber.

4.2.1.5 DISCUSSION

Table 4.3 shows a summary of the β-sheet content for each different doped silk fiber sample obtained from equation 4.1 and 4.2.

Neat degummed presents higher percentage of crystallinity and this results will be confirmed in the next section by XRD analysis. Major decreasing in β-sheet contend was measured from

heavily iodinated sample whereas KBr 0,5M treatment maintained highest crystallinity; Data in Table 4.3 show that increase in concentration of doping agent correspond in increasingly lower percentage of crystallinity as well as time of exposure largely affects silk secondary structure. Total β-sheet column refers to the content of β-sheets found after deconvolution of Amide I and Amide II with a common baseline, approximately from 1800 cm^{-1} to 1400 cm^{-1}.

Silk sample	**β-*sheet Amide I***	**β-*sheet Amide II***	**Total β-sheet***
Neat degummed	59,99%	71,22%	65,32%
Lightly I_2	57,53%	70,44%	63,12%
Heavily I_2	49,33%	21,22%	51,34%
$CaCl_2$ 0,5M	58,98%	71,09%	61,87%
$CaCl_2$ 1,0M	57,11%	71,01%	61,62%
$CaCl_2$ 1,5M 10’	53,23%	70,73%	54,99%
$CaCl_2$ 1,5M 2h	50,53%	69,78%	52,65%
KBr 0,5M	58,19%	71,03%	59,88%
KBr 1M	56,29%	71%	57,74%
KBr 1,5M 10’	55,03%	69,09%	56,58%
KBr 1,5M 2h	54,09%	68,87%	55,59%

* Amide I and II were deconvoluted with the same baseline

Table 4.3 antiparallel β-sheet content (%) for all different treated sample.

In Table 4.4, representative results found in literature are summarized; they refer to modification of secondary structure and β-sheet content of silk after a specific treatment or specific preparation techniques. In particular our results are found in good agreement with the work of J. He (J. He et al., 2010) and E. Steven (E. Steven et al., 2011) in which the treatment caused transformation from β-sheet to α-helix structure or random coil (Table 4.3).

On the contrary in the work of X. Chen (X. Chen et al. 2010) the effect of potassium (from KCl) was to increase β-sheet content at difference respect respect to our results with KBr.

Reference	**Experiment**	**Results**
1) Xin Chen et al., 2001	*B mori silk* dissolved with different solvent	LiBr-EtOH dissolved show the most β-sheet conformation
2) Xin Chen et al., 2002	Effect of potassium on silk film	Increasing KCl concentration raises the conformational transition from RC to β-sheet.
3) Jianxin He et al, 2010	Chemical Modification of *BM silk* with calcium salt treatment	modified fibers presented a structure with a lower crystallinity and fewer crystallites.
4) E. Steven, et al. 2011	Effect of iodine treatment on spider silk fibers	Heavy I_2 doping reduces β-sheet peak and increases α-helix one.

Table 4.4. Some similar experiment concerning modification of silk fibroin found in literature.

4.2.2 XRD ANALYSIS

4.2.2.1 INTRODUCTION

X-ray crystallography is a tool used for identifying the atomic and molecular structure of a crystal, in which the crystalline atoms cause a beam of incident X-rays to diffract into many specific directions.

Crystals are regular arrays of atoms, and X-rays can be considered waves of electromagnetic radiation. Atoms scatter X-ray waves, primarily through the atoms' electrons. Just as an ocean wave striking a lighthouse produces secondary circular waves emanating from the lighthouse, so an X-ray striking an electron produces secondary spherical waves emanating from the electron. This phenomenon is known as elastic scattering, and the electron (or lighthouse) is known as the scatterer. A regular array of scatterers produces a regular array of spherical waves. Although these waves cancel one another out in most directions through destructive interference, they add constructively in a few specific directions, determined by Bragg's law:

These specific directions appear as spots on the diffraction profile called reflections. Thus, X-ray diffraction results from an electromagnetic wave (the X-ray) impinging on a regular array of scatterers (the repeating arrangement of atoms within the crystal) (W. H. Bragg, 1913).

X-rays are used to produce the diffraction profile because their wavelength λ is typically the same order of magnitude (1–100 angstroms) as the spacing d between planes in the crystal. In principle, any wave impinging on a regular array of scatterer produces diffraction

An intuitive understanding of X-ray diffraction can be obtained from the Bragg model of diffraction. In this model, a given reflection is associated with a set of evenly spaced sheets running through the crystal, usually passing through the centers of the atoms of the crystal lattice. The orientation of a particular set of sheets is identified by its three Miller indices *(h, k, l)* (N. W. Ashcroft, 1976); Bragg proposed a model in which the incoming X-rays are scattered specularly (mirror-like) from each plane; from that assumption, X-rays scattered from adjacent planes will combine constructively (constructive interference) when the angle θ between the plane and the X-ray results in a path-length difference that is an integer multiple n of the X-ray wavelength λ.

A reflection is said to be indexed when its Miller indices (or, more correctly, its reciprocal lattice vector components) have been identified from the known wavelength and the scattering angle *2θ.*

$$2dsin\theta = n\lambda \qquad (4.3)$$

Such indexing gives the unit-cell parameters, the lengths and angles of the unit-cell, as well as its space group. Since Bragg's law does not interpret the relative intensities of the reflections, however, it is generally inadequate to solve for the arrangement of atoms within the unit-cell; for that, a Fourier transform method must be carried out (J. Jarvis, 1970).

4.2.2.2 SILK SECONDARY STRUCTURE ANALYSIS

The primary sequence plays an important role in defining basic materials. Despite being quite different in their primary structure, B. mori fibroin heavy chain and spider spidroins share fundamental similarities. Both have large central core of repeated modular units, flanked by nonrepetitive amino-(NRN) (Rising A. et al., 2006) and carboxy-(NRC) (Sponner A. et al., 2005) terminal domains. The light chain of B. mori fibroin, has a standard amino acid composition and a nonrepeating sequence. It plays only a marginal role in the fiber (Zhou C. Z. et al., 2001). The organization of the repeating modular units can differ significantly, as seen in the sequences of different protein types. As the major component of B. mori fibroin, the complete amino acid sequence of the B. mori fibroin heavy chain is composed of a highly repetitive (Gly-Ala)n sequence motif and tyrosine-rich domains (Zhou C Z. et al., 2000). The modular units are repeated up to several hundred times in the central core of B. mori fibroin heavy chain and spider spidroins such that they largely determine the macroscopic properties of the fibers. The highly conserved sequence of nonrepetitive amino- and carboxy- terminal domains are essential for fiber formation and expected to be of functional relevance (Askarieh G, et al., 2010).

The primary structural motifs have a preferred secondary structure and give rise to structures higher up the hierarchy. NMR, circular dichroism (CD), IR and Raman spectroscopy were usually used to examine the chemical, conformational, and orientational information of secondary structures for silk proteins (Simmons A. 2001). There are three major conformations of silk proteins: the random coil, the α-helix and the β-sheet (Kaplan D, et al., 1994). Using the approach of Porter, and reducing the complex secondary structure of silk proteins into fractions of ordered and disordered material, they are roughly equivalent to crystalline and non-crystalline phase of silk proteins, respectively (Dekker M. et al., 1995). The solid threads are characteristic of well-oriented β-sheet, the dominant secondary structure in silk fibers (Rousseau M. E. et al., 2004). The first Raman spectrum of B. mori silk fiber has clearly shown the predominance of β-sheet, matching the results previously obtained from other techniques (Kheng S. et al 1989)., The total amount of β-sheet is around 50% for B. mori silk, which matched the proportion of the (Gly-Ala)n motif (Asakura T. et al., 2002) Therefore, it is widely accepted that the B. mori fibroin is composed of a highly repetitive (Gly-Ala)n sequence motif adopting antiparallel β-sheet conformation, namely silk II of the crystalline form. The β-sheet crystallite is the molecular network constructed by crosslinking β-sheet conformation of the molecular structures within several neighboring silk protein molecules. It can be indexed as a monoclinic space group with a rectangular unit cell parameter of a=0.938 nm, b=0.949 nm and c=0.698 nm for B. mori silk (Takahashi Y, 1994). Drummy et al. investigated B. mori silk fiber bundles using wide angle X-ray scattering (WAXS) (Drummy L F. et al., 2003). The amorphous halo was also investigated from the WAXS pattern. The results concluded that silk fiber is made up of crystalline regions and connected by regions of amorphous or non-crystalline regions, each comprising of approximately 50% of the total structure. These features are in agreement with structural model proposed before (Termonia Y., 1994). It is expected that the mechanical properties of silk fibers will critically depend on the characters of β-sheet crystallites, significant properties include crystallinity, size (aspect ratio, distribution) and dispersion of β-sheet crystallites, the intercrystallite distance, and the degree of orientation in the silk fiber. The size of β-sheet crystallite in B. mori silk fiber, determined via quantitative examination of the dark field TEM images, were revealed to be 20 to 170 nm in the axial direction and 1 to 20 nm in the lateral direction. And all the crystallites were uniformly distributed in the whole fiber matrix (Shen Y. et al., 1998). The smaller crystallite sizes, as measured from LVTEM and WAXS images, are a reasonable match to those calculated from Scherrer analysis of x-ray fiber pattern. It has a large distribution of sizes range from only a few nanometers to tens of nanometers in length.

The non-crystalline regions are often described as amorphous, poorly orientated, or randomly coiled sections of the peptide. The structural organization in the amorphous phase is not well understood yet. The existence of β-turn or β-spiral and helical conformations has been suggested for amorphous domains (van Beek J D. et al. 2002) . The stability of these structures is given by the interchain hydrogen bonding. The molecular chains in the amorphous phase are often considered to be randomly oriented. Studies from Raman and SS-NMR reported that the protein backbones in the amorphous regions of silk fibers are not randomly oriented but exhibit certain degree of orientation along the fiber axis, albeit much less oriented than β-sheet crystallites. Meanwhile, the higher level of orientation of the amorphous phase for the spider silks than that for B. mori silk.

XRD analysis was carried out with the aim of reveal some important parameters related to the structural conformation of silk fibroin after the different treatments. In particular the predominance of crystalline or amorphous phase, extrapolated matching each diffraction direction *(hlm)* to the right index between Silk I and Silk II structure was examined: the indexing of Silk I and II X-ray profiles will follow Lotz and Keith, and Warwicker model (Lotz and Keith, 1971) (J.O. Warwicker, 1961).

Changes in the structure of silk fiber were previously determined by NMR, WAXS and FTIR-ATR. Recent studies (D.L. Kaplan 2014) have been identified three silk fibroin conformations by X-ray diffraction, NMR, and infrared spectroscopy: random coil, α-form (silk I, type II β-turn) and β-form (silk II, anti-parallel β-pleated sheet).

It is confirmed that corresponding d-spacings for silk I and II are as follows (in nanometers): 0.98 (II), 0.74 (I), 0.56 (I), 0.48 (II), 0.44 (I), 0.43 (II), 0.41 (I), 0.36 (I), 0.32 (I), 0.28 (I). In these d-spacings, the 0.74 nm peak occurs in a region of scattering space well removed from peaks found in the silk II structure. Therefore, the peak at spacing near 0.72 nm is a strong evidence for silk I structure. (M.A. Johnson, 1999) (D.L. Kaplan, 2014).

it is important to understand how the change from one conformation to another can leads the modification of some properties; we said that the antiparallel β-sheet (Silk II) gives strength and resistance to silk fibroin, while helical conformation (Silk I) confers toughness. For this reason transition from Silk II to Silk I means an increase in toughness and a loss of stiffness.

The following scheme presents the procedure used to distinguish between Silk I and Silk II structure based on the assignation of each peak to a specify crystallographic direction.

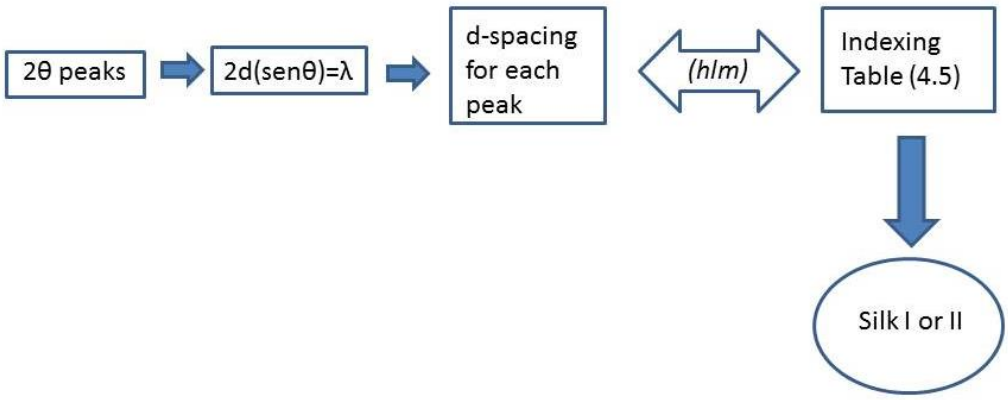

Figure 4.7. Procedure used to distinguish between Silk I and Silk II structure based on the assignation of each peak to a specify crystallographic direction.

Table 4.5 presents the matching between d-spacing (nm), crystallographic direction and diffraction angle (2θ), both for Silk I and Silk II.

Silk I (α-helix)			**Silk II (pleated β-sheet)**		
d-spacing (nm)	**2θ (°)**	***(hlm)***	**d-spacing (nm)**	**2θ (°)**	***(hlm)***
0,74	11,81	0 1 3	0,98	8,02	1 0 0
0,56	15,62	0 2 3	0,48	18,24	2 0 0 / 1 1 3
0,44	19,91	2 1 0	0,43	20,38	1 2 0
0,41	21,38	2 2 0			
0,36	24,4	2 2 3			
0,32	24,73	2 0 6			
0,28	28,34	0 5 3			

Table 4.5. matching between d-spacing (nm), crystallographic direction and diffraction angle (2θ), both for Silk I and Silk II (M.A Johnson, 1999), (D.L.Kaplan, 2014).

Diffraction profile of silk fiber samples was initially fitted by different function e.g. Gaussian, Lorentian, Voigt; after an accurate analysis we finally choose a Gaussian curve fitting thanks to high flexibility and simplicity in the parameter adjustments. As we will see in the following section each diffraction profile is characterized by several overlapping peaks and the intensity is a linear combination of individual components. Peak deconvolution was applied to each plot after defined a curved baseline to the profile.

Silk II structure percentage (X_c) was calculated after deconvolution using the following formula (4.4).

$$X_c[\%] = \left[1 - \frac{S_I}{S_I + S_{II}}\right] x\ 100 \qquad (4.4)$$

Where S_I is the Silk I integrated area (that corresponds to the sum of the areas under Silk I peaks) and S_{II} is the Silk II integrated area (that correspond to the sum of the areas under Silk II peaks). After having assigned conformation (Silk I or II) to each overlapped peak, it was performed a Gaussian curve fitting and subsequently integrated areas were calculated.

Figure 4.8 summarizes few steps used in order to calculate Silk II fraction after curve fitting and deconvolution of peaks; first graph from left presents not manipulated raw data; graph in the middle presents selection of peaks of interest and tracing of raw data with multiple points curve; last figure in the right presents deconvolution of peaks with Gaussian curve.

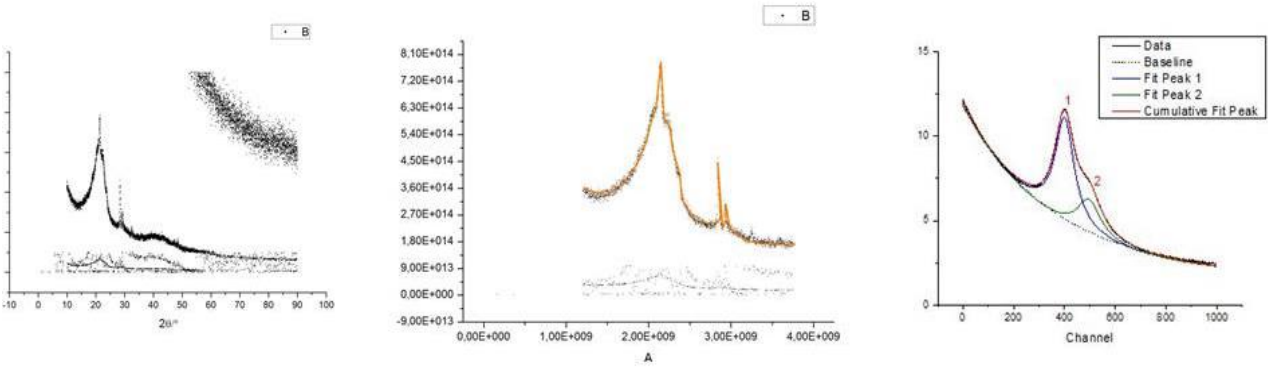

Figure 4.8. First graph from left presents raw data not manipulated; graph in the middle presents selection of peaks of interest and tracing of raw data with multiple points curve; last figure in the right presents deconvolution of peaks with Gaussian curve.

The portion of β-sheet crystallites is quantified by X_c parameter, which can be calculated from the experiment data. The crystallinity of the *Bombyx Mori* silk is about 50%.

The crystallites play a key role in determining the mechanical properties of silk. β-sheet crystallites act as the interlocking to transfer the load between the partially extended macromolecular chains, enabling the uniaxial extension of the amorphous matrix till the rupture of the crystallites. In general, the mechanical properties of silks are determined by the hierarchical structures at all levels; toughness of silk is attributed to its nano-fibrillar structures with their strong inter-fibrillar interactions, as well as the fine channels described for probable energy dissipation. The strength of silk is attributed to the presence of the compacted β-sheet structures which bind molecules with the "inter/intra-molecular junctions". Reducing the crystallite size and increasing their alignment along the fiber axis have been adopted to increase the mechanical strength and toughness of silks (D. Saravanan, 2006).

The size of crystallites in each dimension can be extracted by the radial integration of intensity as a function of azimuth angle along the equator and meridian of the XRD profile.

crystallite size in one direction was calculated based on the peak width approach: the peak width varies with 2θ as cosθ following Sherrer equation:

$$L = \frac{0.89\lambda}{FWHM cos\theta} \qquad (4.5)$$

Where K is the Sherrer constant, L is the crystallite size and FWHM is the Full Width at Half Maximum the width of the diffraction peak, in radians, at a height half-way between baseline and the peak maximum. In our case we have used K=0,89 (Jianxin He, 2009).

The following scheme (Figure 4.9) shows the procedure used to calculate Silk II fraction and crystallite dimension; Obviously in the calculation of crystallite dimension, FWHM is related only to Silk II structure peaks.

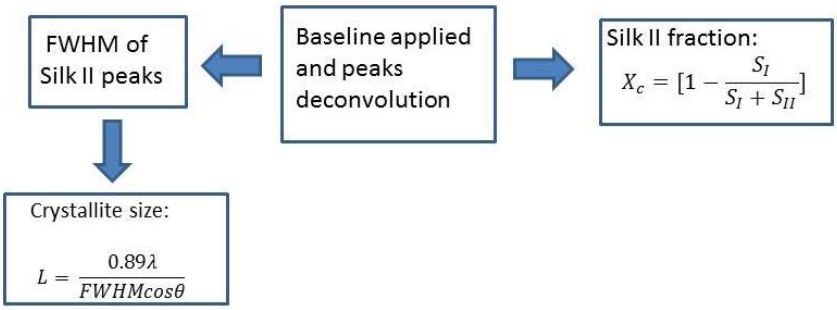

Fig 4.9. Steps used to calculate Silk II fraction and crystallite dimension after peaks deconvolution.

In our experiment X-ray diffraction was recorded at room temperature from 5° to 90° at a scanning speed of 0.02/s with a Rigaku-D/Max-2550PC diffractometer (Tissue Repair Lab, NUS Singapore) with Ni-filtered Cu Ka radiation at a wavelength of 0,1371 nm. The operating voltage and current were 40 kV and 30 mA, respectively.

4.2.2.3 NEAT SILK FIBER DIFFRACTOGRAM

In Figure 4.10 we can see the diffraction profile of neat silk fiber after degumming; dots lines present different 2θ angle where we expected to find Silk I or Silk II structure peaks: Silk II

peaks taken into consideration are those for 2θ =18,24° and 2θ =20,38° whereas all the others are related to Silk I structure.

Before every diffraction profile interpretation we should consider that peak profile is a convolution of the profiles from several contributions, such as temperature factor, microstrain (lattice distorsion, dislocation), instrumental profile, crystallite size, sample preparation etc. We must expect that for every crystallographic direction the peak obtained is overlapped with the close others.
In our case the peak at 20,38° was attributed to Silk II structure but it undergo the contribution of the peak at 19,91° (Silk I). An opposite situation can be observed for lower diffraction angles; the 0.74 nm peak occurs in a region of scattering space well removed from peaks found in the silk II structure. Therefore, the peak at spacing near 0.74 nm is a strong evidence for silk I structure.

As we expected after FTIR analysis, neat silk fiber presents very marked Silk II peaks, and compared with the others doped fiber samples (see 4.2.2.4 section) it shows highest Silk II fraction (Table 4.6). Largest peak occurs at around 2θ=20° and it is the sum of three close reflections; Silk I peak at d=0.74 nm (11,81°) is well defined as we expected and the calculated Silk II fraction for this sample is 53,33%. (eq. 4.4).

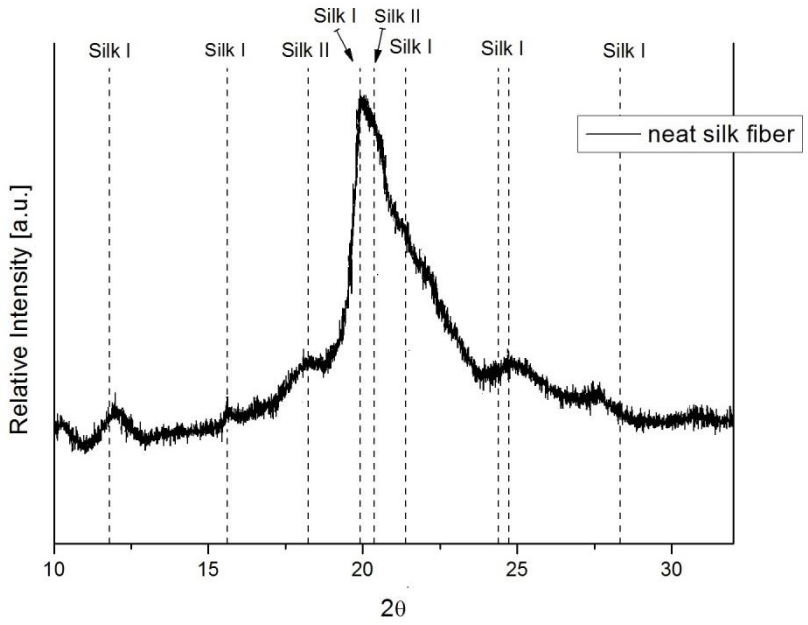

Figure 4.10. Diffraction profile of neat silk fiber after degumming. Dots lines present different 2θ angle where we expect to find Silk I or Silk II structure peaks (Kaplan, 2014).

As we will see in the following section, almost all the peaks attributed to Silk II and I will decrease in intensity as indication of partially degradation of β-sheet and α-helix and partially transformation in random coil amorphous structure.

4.2.2.4 MODIFIED SILK FIBER DIFFRACTION PROFILE

In this section we interpret diffraction profiles of modified silk fiber; only highest doped fiber were studied (heavily I_2, $CaCl_2$ 1,5M, KBr 1,5M doped fiber); at the end of the section are reported all the results for Silk II fraction (X_c) and crystallite size in the direction of fiber axis obtained with the method described in the 4.2.2.2 section. We should remember that the different silk fibroin conformation are random coil, α-form (silk I, type II β-turn) and β-form (silk II, anti-parallel β-pleated sheet), just to remember that the increment or decrement of peak intensity is related to random coil formation.

Passing from neat silk fiber to iodinated one we note firstly that Silk II peaks (red dot vertical lines) reduced in intensity as indication that I_2 (possibly in multiple forms of anions and molecular iodine) initially trapped within the β-sheets regions made some of the β-sheets unstable, converting part of them into amorphous phases. It is probable that these β-sheets were converted to random coil and not to α-form due to the fact that Silk I peaks decrease in intensity as well, but not disappear at all (see peak at d = 0,74 nm, 2θ= 11,81°). Also at 2θ = 24,4° and 24,73° (both Silk I) we do not see a substantial decrease in peak intensity and it means that iodine ions mainly degrades β-sheets instead of α-helices. For heavily I_2 treated sample was found 47,98% of silk II fraction and a crystallite size of 3,11 nm.

In the case of $CaCl_2$ modified sample on the contrary almost all the peaks related to α-form decrease in intensity (2θ= 11,81°, 15,62° , 21,38° , 24,4° , 24,73°) and this is due to the destruction of secondary H-bond by the calcium ions. Indeed we have supposed that part of the secondary bond are hydrogen bond among the α-helices and the calcium ions partially coordinates with lateral groups of the backbone, destroying this bonds.

A similar diffraction profile is seen for KBr doped fiber but the differences in the peaks at 2θ = 11,81° and 21,38° respect to $CaCl_2$ ones, point that destruction of secondary bonds is less likely in this case; random coil secondary structure is the results of this transformation in both salt doped samples.

As we see from Fig 4.11 the main convoluted peak at around 2θ=20° is considerably smaller for $CaCl_2$ and KBr samples and it is also due to the decreasing of Silk II peak at 2θ=18,24°; despite this, the reduction of this Silk II peak is higher in the iodine treated sample.

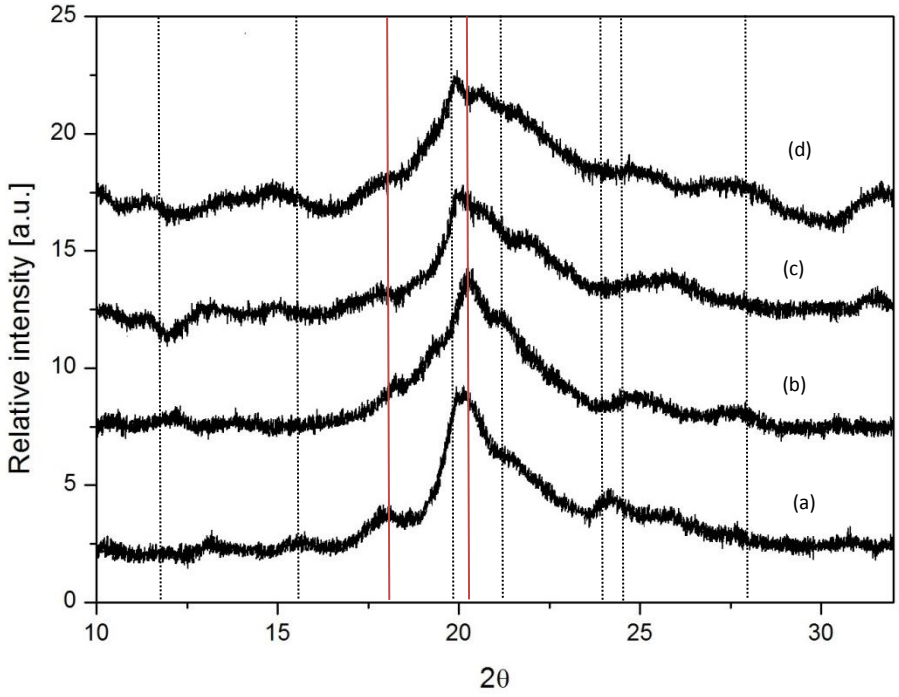

Figure 4.11. XRD Diffraction profile of modified silk fibers, respectively neat degummed (a) heavily I_2 doped (b), 1,5M $CaCl_2$ 2h doped (c) and 1,5M KBr 2h doped (d). Red vertical lines are related to Silk II structure diffraction angles.

4.2.2.5 SILK II FRACTION (X_C) AND CRYSTALLITE SIZE

The diffraction profile of silk fibers was fitted by the Gaussian function and ranged from 10 to 35 of the corresponding Bragg angle (2θ reflection angle). Baseline and deconvolution of diffraction profile was applied (Origin Lab 8.0 software) and using equations 4.4 and 4.5 an estimation of Silk II fraction (X_c) and crystallite size in the direction of fiber axis has been given. Table 4.6 reports results for all the doped samples;

It is important to note that to higher crystallinity corresponds higher crystallite dimension (nm) and this fact can be used to tailor mechanical performances of silk material; reducing the crystallite size and increasing their alignment along the fiber axis can be adopted to increase the mechanical strength and toughness of silks.

Silk sample	Silk II fraction (%)	crystallite size (nm)
Neat degummed	53,33	3,68
Heavily I_2	47,98	3,11
$CaCl_2$ 1,5M 2h	49,97	3,27
KBr 1,5M 2h	51,24	3,52

Table 4.6: Silk II fraction and crystallite size of different treated silk fibers.

4.2.2.6 DISCUSSION

We have seen that a combination of FTIR and XRD can be used to predict structural modification in semi crystalline material like silk fibroin; XRD analysis has confirmed some of the conclusions and hypothesis done after FTIR tests. In general iodine and salt doping have partially destabilized antiparallel β-sheets and in the case of $CaCl_2$ and KBr it was assumed that free ions coordinates with long chains destroying part of secondary bonds.

Many of the conclusions just made concerning the structure of silk fibroin will be the starting point to justify mechanical and electrical behavior or will be further proof to confirm and strengthen the conclusions just made.

4.4 ELECTRICAL CHARACTERIZATION

4.4.1 INTRODUCTION:

Silk structure in dry state is naturally an insulator; it is well know that the conductivity of some polymers is the result of several processes; conducting polymers have backbones of contiguous sp^2 hybridized carbon centers. One valence electron on each center resides in a p_z orbital, which is orthogonal to the other three sigma-bonds. All the p_z orbitals combine with each other to a molecule wide delocalized set of orbitals. Undoped conjugated polymers state are semiconductors or insulators. In such compounds, the energy gap can be > 2 eV, which is too large for thermally activated conduction. Therefore undoped conjugated polymer such us polythiophenes, polyacetilenes only have a low electrical conductivity of around 10^{-10} to 10^{-8} S/cm. Even at a very low level of doping (< 1%), electrical conductivity increases several orders of magnitude up to values of around 0.1 S/cm (A. K. Bakhshi, 2011). Some of this conducting polymer are on the basis of organic electronics.

Despite this great achievements in semiconducting polymers, scarce efforts were made for making silk fibroin conductive; recent experiment (B. Tulachan, 2013) have observed that, when a silk membrane was doped with common salt solution (1 M NaCl solution), it resulted in maximum current flux measurement respect to other kind of modification. Further, in the absence of humidity, no significant current was measured across fibrous protein matrix.

Conductive polymers (polypyrrole, polyaniline or poly3,4-ethylene-dioxythiophene)/silk fibroin composite fibers were fabricated successfully and expediently by in situ polymerization without any modification of silk fibroin surface; the conductivity reached is althougt less respect the conjugated polymer like PEDOT/PSS blend (Y. Xia et al., 2014).

Conductive, biocompatible and mechanically robust materials for use in bioelectrical applications have been developed using a new strategy to selectively incorporate poly(pyrrole) (Ppy) into constructs made from silk fibroin (Romero I. S., 2014). It was demonstrated that covalent attachment of negatively charged, hydrophilic sulfonic acid groups to the silk protein can selectively promote pyrrole absorption and polymerization within the modified films to form a conductive, interpenetrating network of Ppy and silk that is incapable of delamination. To further increase the conductivity and long-term stability of the Ppy network, a variety of small molecule sulfonic acid dopants were utilized and the properties of these silk-conducting polymer composites were monitored over time. Using this

strategy, have been produced mechanically robust polymer electrodes in a variety of geometries with stable electrochemical performance and sheet resistivity on the order of 102 Ω/sq (conductivity ~1 S/cm).

The electrical resistivity (or conductivity) of a fiber can be measured in the most basic scheme by means of simple resistance probe. Both two probe and four probe variants are often utilized when measuring the resistivity of a material sample. In the former method a uniform current density is applied across the specimen sandwiched between two electrodes located on parallel faces and measure the potential drop across the latter electrodes.

The two probe method is highly sensitive to the contact resistance at the current injection electrodes because the measured potential difference includes the potential drop across the electrode and its interfaces. As noted using the resistance measured between two electrodes, the resistivity can be measured when the material specimen has a simple geometry of known dimensions (S. Rebouillat, 2011); the four probe method provides results which are more reliable because it is not sensitive to contact resistance issues. In the four probe method, one pair of probes is used for the current injection at a pair of electrodes while the other pair is used for voltage measurements on a different set of electrodes.

The resistance is determined using Ohm's law and the resistivity can be calculated if the applied current is uniform and the specimen dimensions are known: the expression of resistivity in terms of geometrical factors is the following (eq. 4.8).

$$\rho = \frac{RA}{L} = \frac{\pi d^2 R}{4L} \qquad (4.8)$$

Where A is the transversal cross section, d is the diameter L is the length of the specimen and R is the resistance (V=IR).

These approaches for measuring the resistivity are well suited for simple block-like specimens subjected to uniform currents, where the electrodes cover the entire sides of the specimen. The measurement of resistivity in conductive polymer composites has got quite sophisticated.

4.4.2 EXPERIMENTAL SETUP AND ERROR SOURCES

For our experimental setup silk fibers were connected in two-terminal conductivity configuration using carbon paste (Sigma Aldrich). For these high resistance samples (R $>10^7\Omega$), electrical conductivity measurements were performed with an electrometer (Keysight B2900A series; broad voltage (210 V) and current (3 A DC and 10.5 A pulsed) sourcing capability, with high precision (minimum 10 fA/100 nV sourcing and measuring resolution) in two-terminal configuration inside a shielded box.
Electrometer was chosen due to its very high internal resistance relative to the sample under test. In this case, it is very important to perform background leakage current check before characterizing the sample. Furthermore, it is very important to allow enough time for the discharge of any stray capacitance present in the system before recording the current values during each measurement.

For humidity dependent conductivity measurement, the sample was mounted in two-terminal configurations inside a humidity chamber (Figure 4.19) that was also equipped with a pressure-independent humidity sensor. The sample and humidity sensor were mounted side-by-side in the middle chamber. The left chamber was connected to the water reservoir, and the right chamber was connected to a vacuum pump. By turning the regulators in each chamber, it was possible to control the relative humidity (*RH*) level at a desired rate; for example, closing the left valve and opening the right valve would decrease the *RH*.

In our work we have assumed that the silk fiber transversal section was circular (eq. 4.6) even recent SEM measurements (Y. Shen, 1998) have revealed that it is usual triangular: with this assumption, in the calculation of the conductivity we have to taking into account also the error on the fiber section besides the standard deviation derived from the empirical formula used to calculate the diameter.
It was very important to allow enough time for the discharge of any parasitic capacitance present in the system before recording the resistance values during each measurement. We made four measurements for each test.

4.4.3 I-V CURVE

In this section we evaluated the current response to voltage applied in order to confirm the Ohm's law. 4 different tests were performed for each doped sample (with respectively 4 different fibers from the same doped tow).

As expected, the spider silk fiber is highly insulating. The current value (I) of the silk fiber at ambient condition (50% RH, 25 °C) is in the order of few tens of nanoampere as seen from the current-voltage plot (Figure 4.17). A slight non-linearity in the lower voltage region from 0 to 10V was observed; an increase of flowing current was detected in the silk fiber at 60 °C with a more linear response (blue line Figure 4.17). It is clear at the beginning that we are dealing with ionic and temperature activated conductivity.

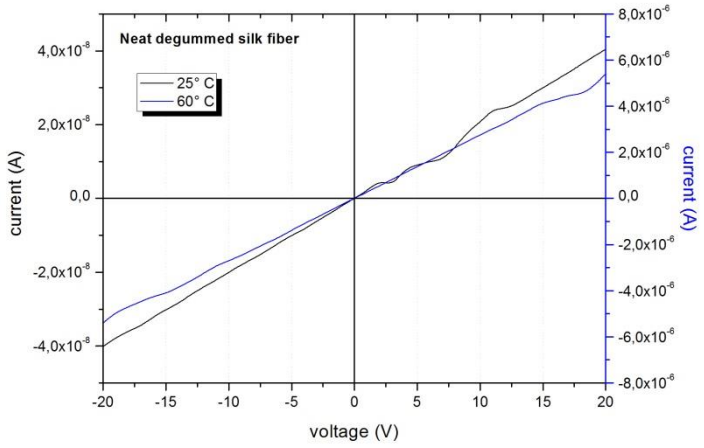

Figure 4.17. I-V plot of neat degummed silk fiber at 25° (black line) and 60° degree (blue line).

The following graphs (Figure 4.18) refer to I-V curve of the doped silk fibers at ambient condition (50% RH and 25 °C). We note that a slight increase of current response is obtained with doped silk fiber, with a maximum value of around 1,5± 0,03 $x10^{-5}$ A for heavily iodine doped sample; $CaCl_2$ 1,5M sample reaches a current value of 1,4±0,01 $x10^{-5}$ A, whereas KBr 1,5M one 1,1±0,02 $x10^{-5}$ A at 20V applied voltage.

In the following section we will see how temperature and humidity modulates the resistivity of the material, thereby regulating the current flux across silk fiber matrix. No response was

observed when I-V studies were conducted in the absence of humidity (10^{-9} A). This is due to a very high resistance of silk, thus behaving more like an insulator, in a dry condition.

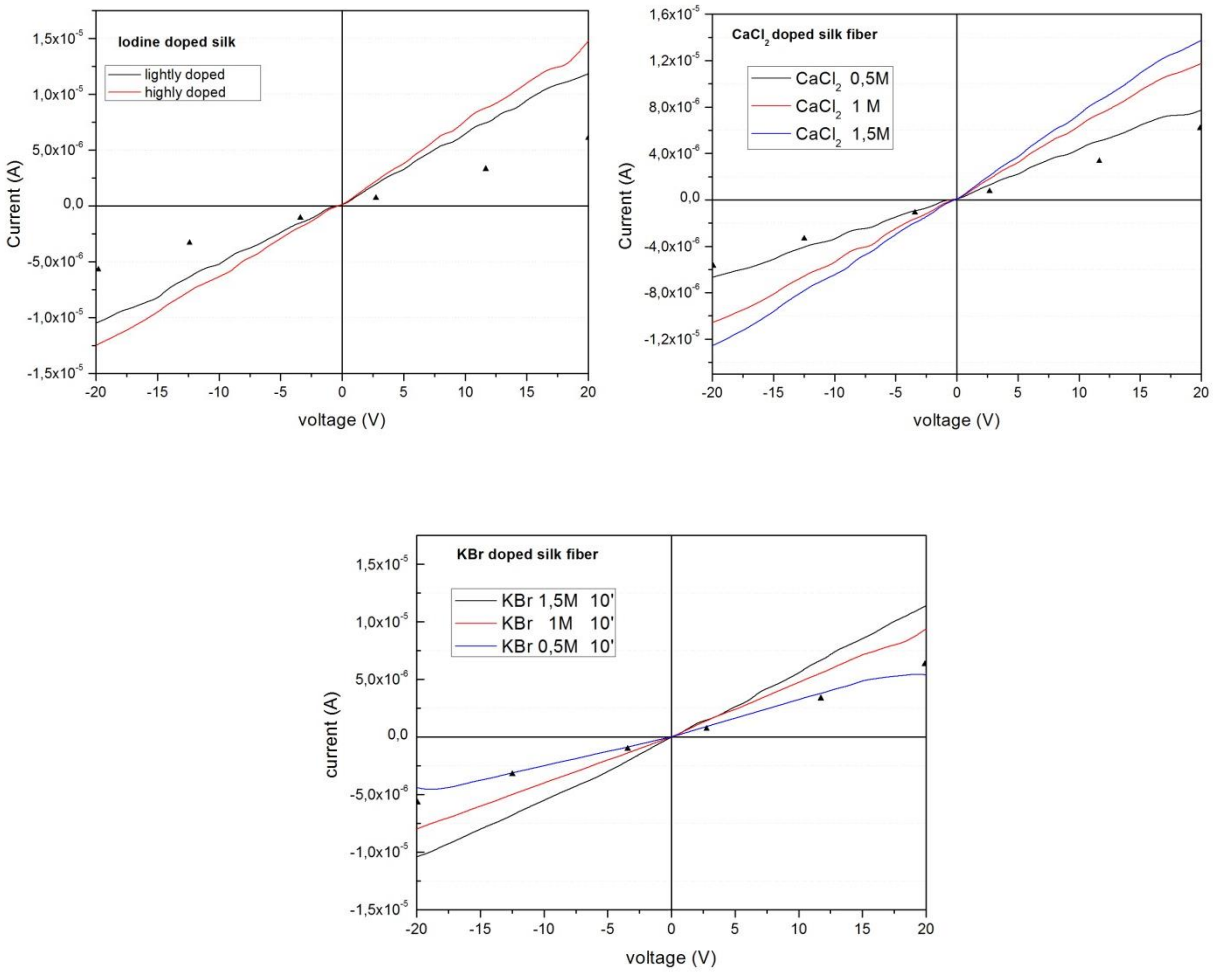

Figure 4.18. I-V plot of doped silk fibers at different concentration of doping agent. Top left: heavilyy and lightly iodine doped. Top right: $CaCl_2$ doped sample. Down: KBr doped sample. Scatter points (triangles) refer to neat sample values from I-V plot in Fig. 4.17 at 25°C.

4.4.4 TEMPERATURE AND HUMIDITY RESPONSE

To achieve reasonable current value through the silk fiber we can modulate the humidity and the temperature. For humidity and temperature dependent electrical response, the sample was mounted in two-terminal configurations inside a control environment chamber (Figure 4.19) that was also equipped with a pressure-independent humidity sensor. The sample and humidity sensor were mounted side-by-side in the middle chamber. The left chamber was connected to the water reservoir, and the right chamber was connected to a vacuum pump. By turning the regulators in each chamber, it was possible to control the relative humidity (*RH*) level at a desired rate; for example, closing the left valve and opening the right valve would decrease the *RH.*

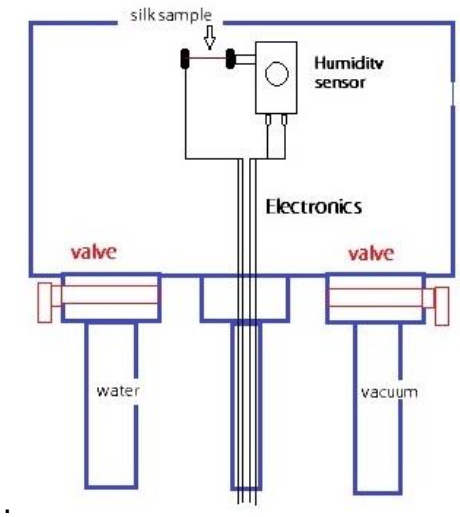

Figure 4.19: scheme of the humidity chamber

We have evaluated the temperature and humidity electrical response of each different doped silk fiber (I-T graph are obtained at 50% of relative humidity), and we try to speculate the most probable current flowing mechanism through silk matrix.

The first graph (Figure 4.20, left) is referred to electrical response for degummed silk fiber by changing the temperature at a fixed humidity, whereas the second is referred to the

conductivity versus the relative humidity extracted by the current values obtained from the electrometer using the well know geometrical factor (eq 4.8); no current is detected until reaching 20 °C, where is present a sharp increase of current and a further slight increase is in the 30-50 temperature range, after a relatively steady state condition; from 45 to 60 degree is present a very low increase of current and the maximum value at 60°C is 9,3±0,4 x10^{-7} A.

In the second graph (Figure 4.20, right) we can see that the dependence of the conductivity with RH is exponential only after around 55% of relative humidity and the values are more or less similar both for 10 and 20 Volt applied. The conductivity reaches 1,1±0,2 x10^{-6} S/cm at RH=70% whereas very low value of current has been detected for low relative humidity range (10 to 40 %).

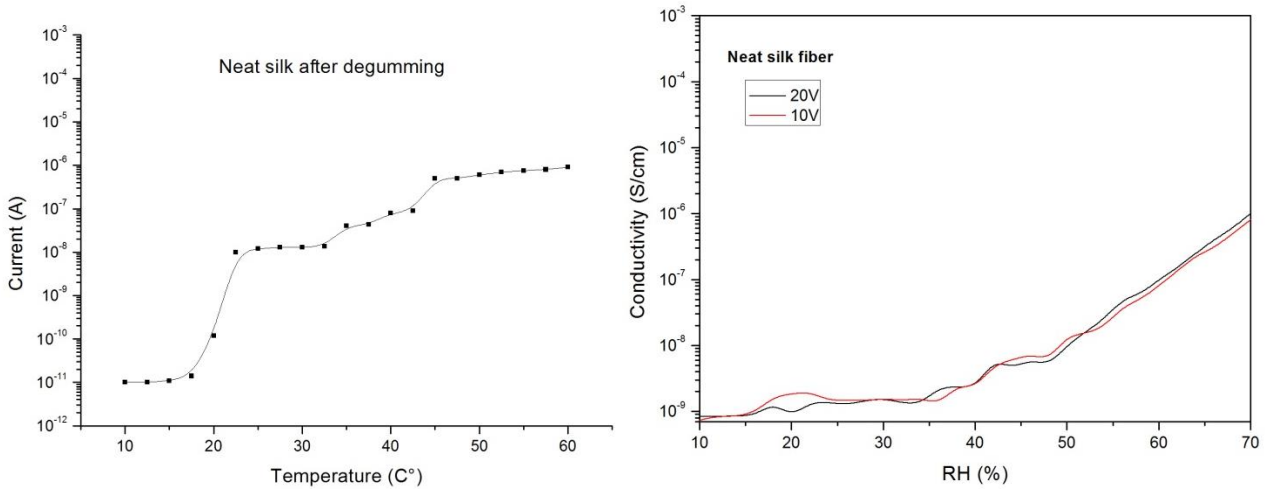

Figure 4.20. Left: current response of neat silk fiber against temperature variation from 10 to 60 Celsius degree at fixed RH value. Right: conductivity against relative humidity from 10 to 70% at a fixed temperature value.

From figure 4.19 (I-V characteristic of neat silk fiber) we note that the increase of current still remain in the same order of magnitude inside the range of voltage considered. The main increase is seen for the change of temperature and relative humidity.

The first assumption is that electrolytes present in the water may combine chemically with the long chain molecules, but they are capable of easy dissociation and this dissociation depends on the temperature; silk can be regarded as ion-exchanging material.

These results are in good agreement with a work by E. Steven,. (E. Steven et al., 2011) in which current flowing in silk matrix presents an humidity activated behavior and it was also proposed the following relationship for the conductivity dependence with RH (eq. 4.9).

$$\sigma = \sigma_0 e^{(0,23RH)} \qquad (4.9)$$

Where σ_0 is the conductivity at RH=0% and RH is the relative humidity.

The first sharp increase of current at around 20°C is probably related to the detachment of ion charged carriers (H^+, OH^- or electrolytes such as Na^+ K^+ Cl^-) from the chain molecule and this initial detachment triggers the current flow through the matrix; the second low increase is probably related to temperature activated diffusion of the ions, that need energy to overcome the resistance of the matrix ; we may also assume that β-sheet are further hindrance to the diffusion of charge carriers, so that fixed the other parameters, the higher is the β-sheet content, the higher is the resistance to diffusion.

It is assumed that the sites where ions are held in loose chemical combination (or adsorbed strongly) are periodically arranged in a regular profile but this is valid only for the amorphous zone within the matrix. These sites are considered to be places where the energy of dissociation into ions is less than that for the dissociation of adsorbed water into H_3O^+ and OH^- . Finally, it is assumed that these sites may have a longer repeat period than the primary structure of the substance; they may reflect the presence of a secondary structure formed during the growth of the material;

In Figure 4.21 we can see that the electrical response of iodine vapor doped silk fiber is higher respect to the neat silk one (the maximum current value at fixed RH at 60°C is 1,01±0,4x10^{-5} A for heavily doped sample, and the conductivity reaches 1,01±0,3 x10^{-3} S/cm at RH=70%

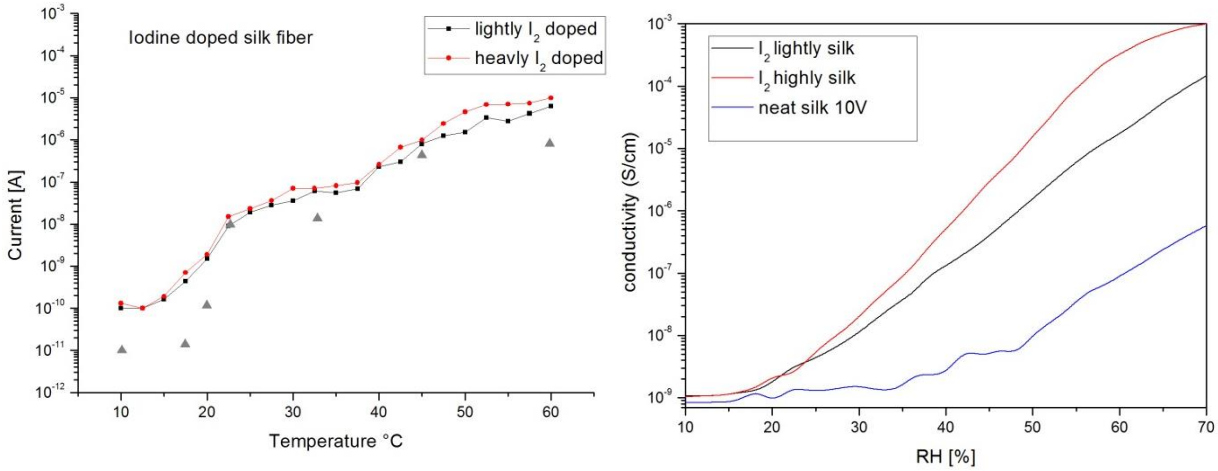

Figure 4.21. Left: current response of iodinated silk fiber against temperature at fixed room RH value (scatter triangles refer to neat sample values) . Right: conductivity against relative humidity from 10 to 70% at fixed temperature value; blue line refers to neat sample response.

By comparing the curves of iodine and neat silk fiber few main differences are clear: For the iodine doped fiber the minimum current detected (at 10-15 °C) is one order of magnitude higher respect to non-treated silk one and this is due to the presence of iodine ions or molecules in the amorphous zone that act as a charge carriers; furthermore the maximum current achievable is around one order of magnitude higher respect to neat fiber. From I vs T curve it is also noticeable an earlier increment of current with increasing temperature: in the iodine fiber it starts flowing at around 15 °C whereas in the neat one at around 20°C.

The conductivity curves confirm this early activation: at RH=30% conductivity value is one order of magnitude higher and the increase stars at around 20% instead of 35% of relative humidity.

We have said that when the fiber is humidified, the water molecules percolates into the fibrous matrix and interacts with the charged ions like Na^+, K^+, Cl^- and may results in the formation of ionic charge carriers. In this case iodine (in form of ion or molecule) water complexes form and diffuse through the matrix and generation of electricity is seen.

The generated current is thermo-electric in nature, since it changes with temperature. At the molecular level, rising temperature increases the thermal motion of the water molecules surrounding the protein, as well as leads to motion of the protein side chains. These molecular motions could results in some form of charge generation by rearranging the hydrogen bond network and by supporting diffusivity.

We can also state that the presence of crystalline structure avoid this ionic-like conductivity by the fact that water can't percolate inside the β-sheet and increase the amount of charge carriers; in the other side the movement of charge carriers is obstructed by crystalline phases: this statement is confirmed by the difference in conductivity between highly and lightly iodinated silk fiber remembering that in the former case the amount of β-sheet is higher respect to latter case so that the diffusion of charge carriers is more difficult.

Moreover in the structural analysis of iodine doped fiber we have seen that it is likely that at high temperature, there is a water-induced thermal glass-transition that enables chain mobility. At this temperature the water molecules act as plasticizers for the fiber and we have also seen that the treatment with iodine partially transformed the β-sheet into amorphous region as confirmed by XRD spectra; the crystalline phase is less in iodine treated samples respect to neat one and this could enhance the conductivity.

In Figure 4.22 we can see I vs T and conductivity vs RH both for $CaCl_2$ and KBr samples. The arrow points the increase in conductivity by increasing doping agent concentration.

For both salt doped sample the increase in current flowing by increasing temperature is not that substantial as in the case of iodine treated sample and even the conductivity reaches values around one order of magnitude lower respect to the iodine silk; nevertheless both maximum current and conductivity are around two order of magnitude higher respect to neat sample and this is a further proof of ions or molecules diffusion trough the silk matrix.

We can state also that water is capable to form complexes with this free ions and the amount of water control the amount of possible complexes formation; this statement is justified by the enanchment of conductivity by increasing RH.

Moreover, temperature can triggers current flowing by providing enough energy to this complexes and the lower crystallinity obtained after the doping contribute to facilitate the movement.

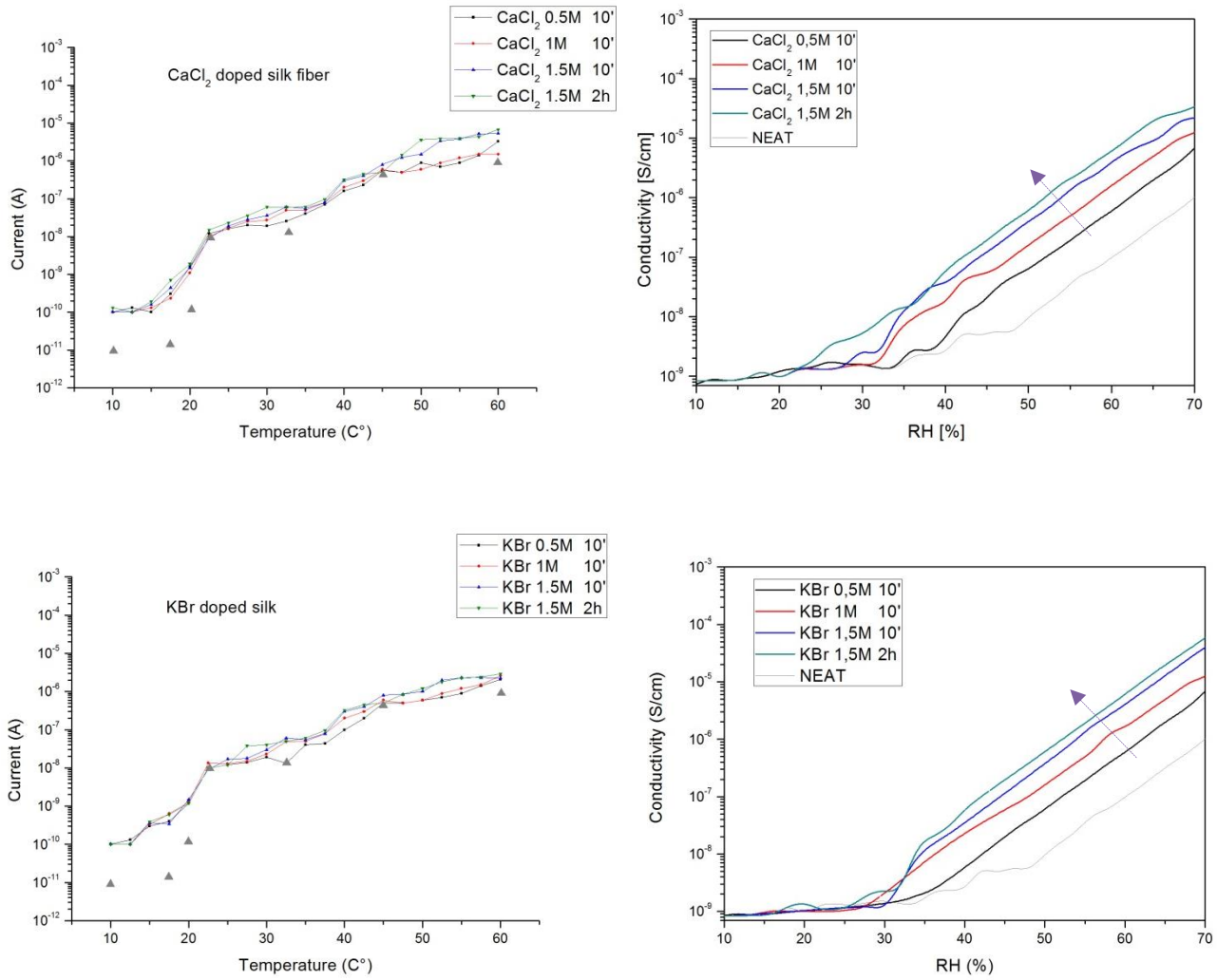

Figure 4.22: First two graphs above represent I vs T and conductivity vs humidity for $CaCl_2$ doped silk fibers; Second two graphs below represent same dependences for KBr doped silk fibers. Green triangles refer to neat sample current against temperature; Green curves refer to neat sample conductivity against RH. Arrows indicate increase of conductivity with doping agent concentration.

4.4.5 DISCUSSION

We have seen how doping silk fibroin can enanche current flowing trough the matrix of a naturally insulator material. Less amount and lower size of crystallites can contribute to facilitate the movement of the formed complexes but despite this, seems like in dry condition is impossible to see an appreciable value of current flowing.

We can say that with a proper modification we can start thinking to use silk in bioelectronic field thanks to his biocompatibility, his outstanding mechanical properties and possible ability in current flowing.

The use of organic polymers for electronic functions is mainly motivated by the low-end applications, where low cost rather than advanced performance is a driving force. Materials and processing methods must allow for cheap production. Printing of electronics using inkjets or classical printing methods has considerable potential to deliver this. Another technology that has been around for millennia is weaving using fibres. Integration of electronic functions within fabrics, with production methods fully compatible with textiles, is therefore of current interest, to enhance performance and extend functions of textiles.

For example, standard polymer field-effect transistors require well defined insulator thickness and high voltage, so they have limited suitability for electronic textiles. In a work by M. Hamedi (M. Hamedi, 2007) was presented a novel approach through the construction of wire electrochemical transistor (WECT) devices, and was shown that textile monofilaments with 10–100 μm diameters can be coated with continuous thin films of the conducting polythiophene poly(3,4-ethylenedioxythiophene), and used to create microscale WECTs on single fibers (H. Hamedi, 2007); we can imagine that by creating conductive fiber we can avoid this coating and create a conducting textile capable to be, for example, a platform for sensing application.

4.3 MECHANICAL CHARACTERIZATION

4.3.1 INTRODUCTION

As mentioned in previous chapters, spider and silkworm silk, known as a kind of lithe and light weighted biomaterial, protein fiber has become one of the most versatile materials due to its extraordinary strength and toughness against stretching, superior to most synthetic high-performance fibers (P. M. Cunniff et al., 1994).

In general, the mechanical properties of silks are determined by the hierarchical structures at all levels. The toughness of silk is attributed to its nano-fibrillar structures with their strong inter-fibrillar interactions, as well as the fine channels described for probable energy dissipation. The strength of silk is attributed to the presence of the compacted β-sheet structures which bind molecules with the "inter/intra-molecular junctions". Reducing the crystallite size and increasing their alignment along the fiber axis have been adopted to increase the mechanical strength and toughness of silks (W. Xiang, 2010).

Mechanical material properties of silk fiber were established by interpreting data from the tensile testing apparatus. In this section we discuss the results coming from tensile uniaxial tests.

Mechanical tests were carried on Instron Tester 5900 provided by NUS Tissue repair Lab.

The silk fibers were first fixed onto a paper frame using double sided tape. Then the paper frame was clamped onto the Micro Tester; the paper frame was cut off before the mechanical test. The force resolution is 0.5% of indicated load, the position resolution is 0.02 μm, and strain rate is 50% per minute; the whole tests were performed at 23 °C and the RH is 60%. The length of each sample was 3±0,1 cm.

4.3.2 FIBER DIAMETER DISTRIBUTION

Silk diameter is the major source of uncertainty in the calculation of the strength, modulus and energy to break. Silk fiber is composed by microfibrils which are not circular in cross section but appear triangular as seen in Figure 2.1 (Y. Shen et al., 1998). One can make a direct

measurement of fiber diameter by means of an optical or scanning electron microscope; there is an ASTM standard to this purpose (Standard Specification for Glass Fiber Strands. Active Standard ASTM D578 / D578M. Book of Standards Volume: 07.01. ASTM).

The main problem with direct measurement is that fiber diameter may not be uniform along the length. An indirect method that gives an average fiber diameter is to weigh a known length of fiber and use the following simple relationship (S. Rebouillat, 2011):

$$d = \sqrt{\frac{4w}{\pi \rho L n}} \qquad (4.6)$$

where w denotes the mass of the fiber sample, ρ represents the density of the fiber, L denote the fiber length and n is the number of filaments per tow.

Often fibers have an irregular cross-section: the above method will give an equivalent diameter of a fiber having an irregular cross-section. After calculating the average diameter we could estimate the transversal cross section.

The mean diameter of 11 samples was 31 ±4 μm per strand. The mean transversal cross-section was $7{,}54 \times 10^3$ μm^2 with a standard deviation of $0{,}2 \times 10^3$ μm^2

4.3.3 NEAT SILK STRESS-STRAIN CURVE

First of all we have obtained the Force versus Elongation plot for neat silk fiber after degumming and we used the simply formula P=F/A to calculate stress-strain plot, where A is the mean transversal section of the fiber. All the results we discuss in this section are the average of 4 different tests up to break on each fiber. Figure 17 shows force (N) versus elongation ($L-L_0/L_0$) plot (left) and stress (MPa) versus strain (%) (right) for neat silk fiber after degumming.

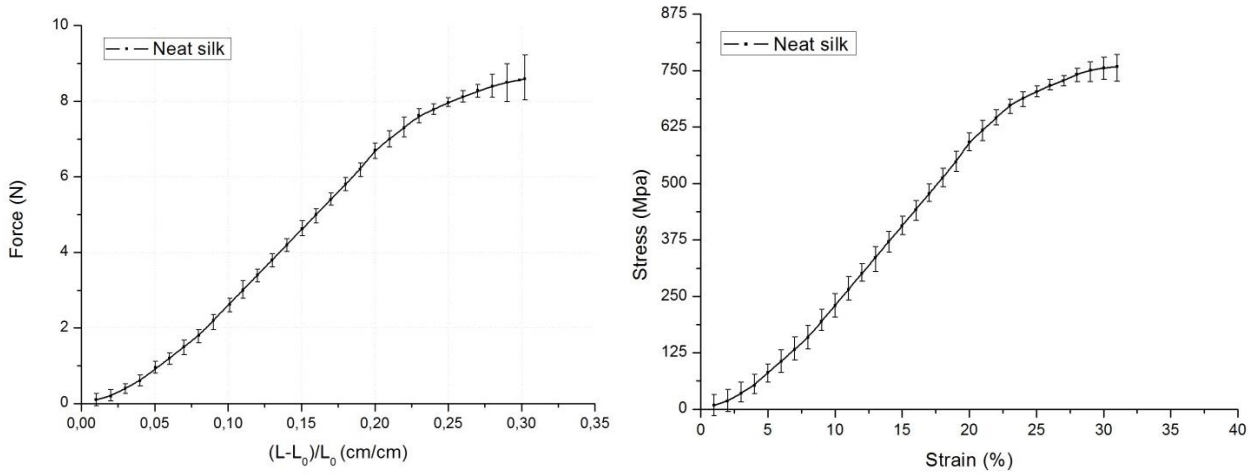

Figure 4.12: Force vs elongation (left), stress vs strain (right) for neat silk fiber after degumming

From the stress strain plot we can calculate several parameters such us initial and post elastic modulus: the initial modulus is taken at 4% of strain whereas the post modulus at 17%; the ratio of post to initial modulus is around 2,8-2,9.

Ultimate tensile strength (breaking stress) is taken before the breaking of the sample, as well as breaking strain; toughness K (kJ/m^3) is the energy of mechanical deformation prior to fiber breaking (eq. 4.7):

$$K = \int_0^{\epsilon_f} \sigma d\varepsilon \qquad (4.7)$$

The elastic region is stiffer than the plastic region, but the elongation is far greater in the plastic zone: it is likely that after yield point in the microstructure the α-helices have extended past their elastic limit and are moving (sliding mechanism) along each other. The β-sheets add resistance to the tensile force applied, much like a dislocation would in a solid.

From Figure 17 we can see that the stress-strain curve of the neat silk fiber assumes a sigmoidal shape similar to that of an elastomer, demonstrating a well balance of strength and elongation (around 0,759 GPa at 30% of strain). In general this stress-strain curve is characterized by three distinct regions: Region I (0-6%) is typical of all silk-like fibers and is characterized by a high initial modulus of around 0,88 GPa and corresponds to the initial

alignment of polymer long chain (Figure 18). All the energy during this phase is spent to untangle long chain themselves from each other.

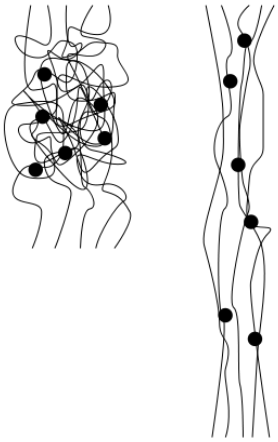

Figure 4.13: Region I: Alignment of long polymer chain after initial force applied. Circles indicate crystallites

After this initial alignment of the long chain, silk fiber experiences an elastic region, Region II (6 - 20%) where it reaches a maximum modulus of around 2,45 GPa at 17% of strain; after yield point, in the Region III (20-30%) exhibits a gradual reduction of modulus until reaching failure strength of around 759 MPa. The point in which the initial chain alignment is almost completed, so the point of the curve in which the fibers start experiencing the elastic region occurs at around 4-6% of strain; we suppose it likely depends on the strength and the amount of secondary bond between long chain as we will discuss in the next sections.

4.3.4 I_2 DOPED STRESS-STRAIN CURVE

We now present the results concerning iodine doped silk fiber, taking into account that each curve in the stress-strain plot is the results of 4 tests up to breaking. (error bars are not shown for clarity).

Some considerations will be made taking into account the results from the structural analysis, which will also help to explain the behavior of fiber under mechanical test.

From Figure 4.13 we can easly note that the iodine treated silk fiber is more ductile respect to untreated one: it presents lower breaking strenght (750±345 MPa) and higher breaking strain (35,06±3,43 %); this is actually valid both for lightly and heavily doped fiber but with some differences: Region I of lightly doped sample is very similar to untreated one (curves are overlapped) whereas heavily doped sample required more energy to align long chains (Fig. 4.13). Post E is almost the same for all samples whereas maximum higher breaking strain is 36,99±3,59 % (heavily I_2 sample).

We can see from table 4.7 that the heavily iodine sample shows the higher toughness respect to all each other (44,04±14,23 kJ/m^3).

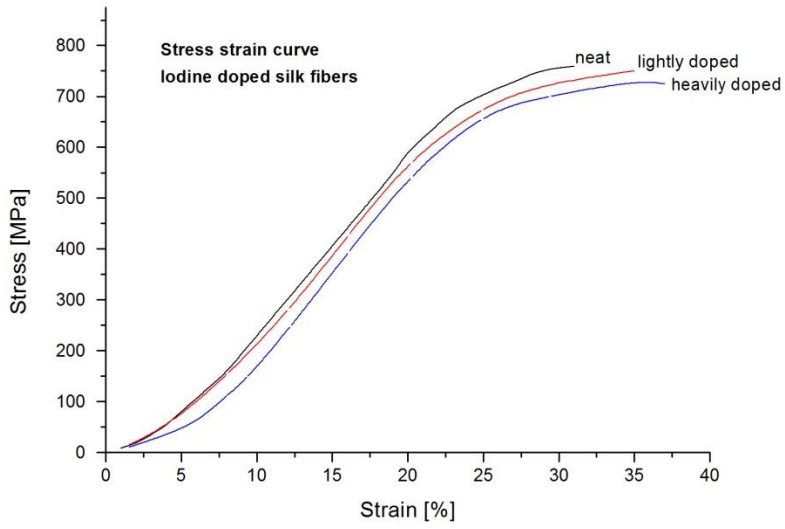

Figure 4.13: Iodine doped silk fiber stress-strain curves

By the results of FTIR analysis we have assumed that iodine ions infiltrate within antiparallel β-sheet, breaking some of the H-bond and partially transform this β-sheets into α-helix or random coil; We also have assumed that this mechanism is more likely in the heavily doped silk fiber caused by larger temperature induced diffusion of the ions. So that we can explain the lower stiffness of I_2 doped sample due to the lower content of the crystalline stiff phase within the silk matrix and also due to the lower amount of secondary bonds among the chains. It is also clear that the lower slope in the region I for heavily doped fiber is caused by the movement of the long peptide chains that is not inhibited by the crystalline domains partially

dissolved during the doping: they act like the dislocation in a metal: lower is the amount and the size of the crystallites, easier is the movement and the reorganization of long chains; this explanation could justify lower initial modulus.

4.3.5 $CaCl_2$ DOPED STRESS-STRAIN CURVE

Stress-strain curves of calcium chloride doped fiber presents several particularities (Fig 4.14): we note a substantial reduction of the slope in the Region III for each doped sample respect to untreated one; moreover the higher is the concentration of the doping agent the higher is the breaking strain and the lower is the breaking stress. This substantial reduction of stiffness could be caused by some different factors: One is the reduction of secondary bond between long chain caused by salt ions as discussed previously, and also the reduction of crystalline stiff component within the matrix. But we think the most important factor that determined the loss of stiffness is the microporous structure created after the treatment; we can assume that in the final part of the test (high applied force) part of the nano fibrils (nm in diameter) have broken, creating large "pores" that weaken the internal structure and eventually coalesce together; this coalescence causes a reduction of transversal section like happen in a metal and is well known that in this condition the Young modulus decrease and the slope of the curve decrease as well (this is valid for all concentration).
Seems that the porosity affects mostly the region III respect to the region I, which however present a reduction in stiffness; in the elastic region the Young modulus is almost the same or slightly lower: it is however complicated to define the exact point in which the alignment occurs and concludes; the elastic region starts at around 8% of strain and for 1,5M $CaCl_2$ 2h sample after 10%. The flattening in the region III is likely caused by the coalescence of pores and the breaking strain is increasingly higher as the concentration increase; nevertheless the toughness is lower respect to the neat sample and only for 1,5M $CaCl_2$ 2h sample it reaches a slightly higher value (Table 4.7).

In general, breaking stress has been decreased of around 20% respect to neat sample and the most likely cause is the formation of microporous structure (and pores coalescence) induced by salt treatment.

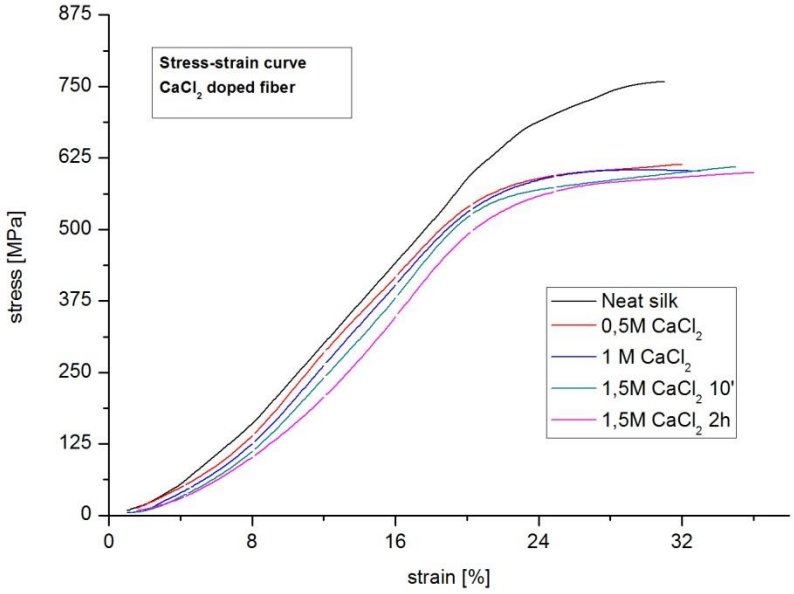

Figure 4.14: $CaCl_2$ doped silk fiber stress-strain curves

4.3.6 KBR DOPED STRESS-STRAIN CURVE

The general profile of the KBr doped silk fiber is similar to the untreated one especially in the region I and II (Figure 4.15).

As we discussed in previous section the weight loss of the silk fiber after KBr treatment is considerably less respect to calcium salt treatment (24% for the former and 32% for the latter) , and this point us that the dissolution of the silk matrix in the amorphous region is more difficult in this case (at equal concentration of doping agent); a further proof of this statement is revealed by the lower flattening of the KBr doped fiber curves in Figure 4.15. Seems that the lower (but present) microporosity has not affected so much the stiffness of the matrix. It is still present an increase of breaking strain so the toughness is also increased for all the treated sample (Table 4.7).

We can state in this case that coalescence of the pores is not likely until the breaking of the sample even if the modification of the structure in terms of degradation of crystallite and hydrogen bonds has been occurred.

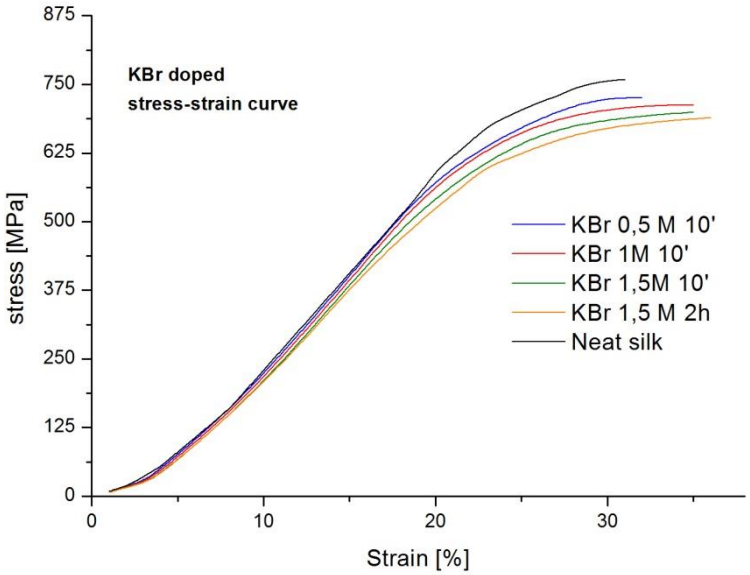

Figure 4.15: KBr doped silk fibers stress-strain curves

4.3.7 DISCUSSION

We can state that crystallites play a key role in determining the mechanical properties of silk. β-sheet crystallites act as the interlocking to transfer the load between the partially extended macromolecular chains, enabling the uniaxial extension of the amorphous matrix till the rupture of the crystallites themselves or the fully alignment of long chains; the existence and the amount of the β-crystallites plays an important role in the occurrence of the yield point of silkworm silk, whereas the work-toughness region of silk was attributed to the partial dissolution of small-sized β-sheets into the matrix and the coalescence of pores.

In Figure 4.16 have been plotted all treated sample at low level of doping to make a comparison with neat silk one: we can see that calcium salt treated sample experienced the lowest breaking stress whereas lightly iodine doped one shows higher breaking strain and toughness.

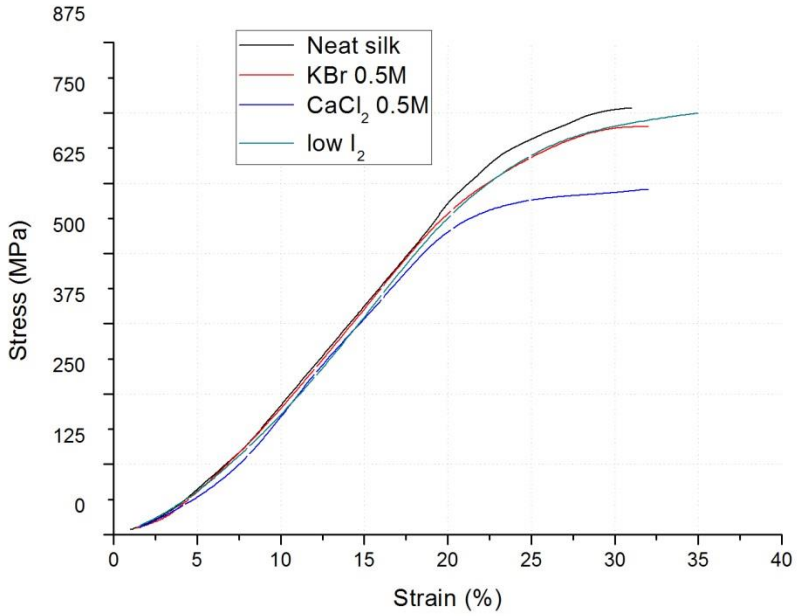

Figure 4.16: Stress vs strain curves comparison between different doped fibers

In the following table (Table 4.7) are summarized the results from stress-strain curve, in particular the initial modulus (taken at 4% of strain), post modulus (taken at 17% of strain), breaking stress and strain and toughness.

Silk sample	Initial E* (GPa)	Post E** (GPa)	Breaking stress (MPa)	Breaking strain (%)	Toughness (kJ/m³)
Neat degummed	0,88±0,31	2,46±0,99	759±300	31,01±3,31	32±10,50
lightly I_2	0,87±0,34	2,45±0,67	750±345	35,06±3,43	41,5±15,54
heavily I_2	0,53±0,34	2,45±0,66	727±398	36,99±3,59	44,04±14,23
$CaCl_2$ 0.5M 10'	0,51±0,21	2,44±0,98	615±356	31,96±2,97	22,27±15,18
$CaCl_2$ 1M 10'	0,50±0,23	2,43±0,69	602±344	33,01±3,48	25,05±11,35
$CaCl_2$ 1.5M 10'	0,48±0,23	2,45±0,67	610±323	34,91±3,20	30,51±14,76
KBr 0.5M 10'	0,83±0,32	2,45±0,89	759±234	31,89±3,20	33,56±12,33
KBr 1M 10'	0,80±0,53	2,43±0,70	728±301	32,95±3,11	35,06±23,93
KBr 1.5M 10'	0,72±0,32	2,41±0,69	700±322	34,9±3,61	35,32±11,65
KBr 1.5M 2h	0,70±0,42	2,38±0,73	690±343	35,88±3,43	35,97±25,87

* initial E is taken at 4% of strain[%] **post E is taken at 17,5% of strain[%]

Table 4.7. Results of uniaxial tensile test concerning Initial and Post E (GPa), Breaking stress (MPa), Breaking strain (%) and Toughness (kJ/m^3) of different treated silk fiber.

With the purpose to validate mechanical analysis the two-sample *t*-test (Snedecor and Cochran, *Statistical Methods*, 1989) was used to determine if two population means are equal; a common application in engineering is for example to test if a new process or treatment is superior to a current process or treatment.

The test statistic in the t-test is known as the t-statistic. The t-test looks at the t-statistic, t-distribution and degrees of freedom to determine a p value (probability) that can be used to determine whether the population means differ.

A two-sample t test compares the mean of a single column of numbers against a hypothetical mean that you provide. The P value answers this question: what is the chance of randomly selecting N data points and finding a mean as far (or further) from the hypothetical value as observed here? If the P value is large, the data do not give you any reason to conclude that the

population mean differs from the hypothetical value you entered. This is not the same as saying that the true mean equals the hypothetical value. You just don't have evidence of a difference. If the p value is small (in this work $p<0,05$), then it is unlikely that the discrepancy you observed between sample mean and hypothetical mean is due to a coincidence arising from random sampling. You can reject the idea that the difference is a coincidence, and conclude instead that the population has a mean different than the hypothetical value you entered; the difference is statistically significant.

In this work were compared two by two each curve obtained from the average value of 4 different test for each sample. Starting from “zero hypothesis” (does the difference is due to a coincidence?) tests revealed in the case of calcium salt doped fibers the zero Hp is rejected if they are compared to the neat sample (Fig. 4.17).

4.5 THERMAL CHARACTERIZATION

4.5.1 INTRODUCTION

Thermal degradation is a molecular degradation process which results from overheating; at high temperatures the components of the long chain backbone of the polymer start to separate (molecular scission) and react with one another to change the properties of the polymer.

The glass–liquid transition is the reversible transition in amorphous materials (or in amorphous regions within semicrystalline materials) from a hard and relatively brittle state into a molten or rubber-like state; many polymers lack well-defined crystalline state and easily form glasses, even upon very slow cooling or compression (Debenedetti P. G, 2001).

Thermal properties of Bombyx Mori silk fiber may be studied by DSC (differential scanning calorimetry), TGA (termo gravimetric analysis) or DTA (differential thermal analysis); the crystalline, hydrophobic β-sheet domains prevent the penetration of humidity resulting in slow degradation of silk under temperature increasing.

Several studies confirmed that many factors can control the degradation behavior of silk material: for instance degradation peak shift under humidity absorption has been studied with DSC (N. Agarwal et al., 1996). Moisture absorption can also affect glass transition: trends in T_g with water uptake correspond reasonably well to predictions of a classical thermodynamic theory, indicating that the plasticization effect of moisture on the combined silk-water system can be satisfactorily explained from macroscopic properties of the constituents without any reference to specific interactions). The moisture-induced decrease of T_g is completely reversible.

In a recent work (X. Hu et al., 2007) it was demonstrated that silk fibroin chains and their intermolecular bound water are treated in total as a polymer–water system, and this system can gain the mobility and experience the transition to the rubbery state uniquely. In the glassy state, all water molecules participate in four hydrogen bonds (two as donor and two as acceptor) with the silk fibroin chains and are held relatively static. As water is heated, the increased thermal energy of water causes the hydrogen bonds to break. In this way, the intermolecular bound water molecules that remain in the film provide additional free volume for the polymer chains to experience a lowered glass transition. Bound water in the silk film acts as a plasticizer, and a lower glass transition of the silk–water system is observed. As

temperature increases above the lower glass transition, all bound water eventually leaves the silk, and the free volume and the silk mobility are reduced. This allows the upper glass transition of the dried silk to be observed

Glass transition temperature of untreated domestic silk B. Mori silk fibroin was observed at 172°C (S. Nakamura, 1985) and was confirmed by other recent experiments (M. Li, 1999). Study by Nakamura confirms that glass transition temperature can shift up to 202°C with a methanol treatment; the rise of the glass transition temperatures of silk fibroins was attributed to the increase in the crystallinity which restricts molecular motions in the amorphous region.

We reasonably supposed that a treatment with a doping agent can also affect the degradation behavior of silk matrix and starting from results of structural characterization, we have performed differential scanning calorimetry analysis.

For our experiments we used a Perkin Elmer DSC7 machine with a scanning rate of 10K/min from -10°C to 400°C; samples with masses of about 5 mg each were encapsulated in Al pans with a special instrument. The DSC machine was calibrated for empty cell baseline, and with aluminum for heat flow and temperature. Al reference standard was used for calibration of the heat capacity through a run method.

4.5.2 NEAT SILK DSC CURVE BEFORE AND AFTER DEGUMMING

Figure 4.23 shows the two DSC curve from non-degummed and degummed neat silk fiber and this two preliminary tests were made to better understand the significance of each peak during the heating process.

During the heating scan both samples first show a bound water evaporation region (T_w) in the range of 40–100 °C; in this region is present a peak (68°C for non-degummed sample and 90°C for degummed one) that was attributed to water evaporation (with evaporation temperature

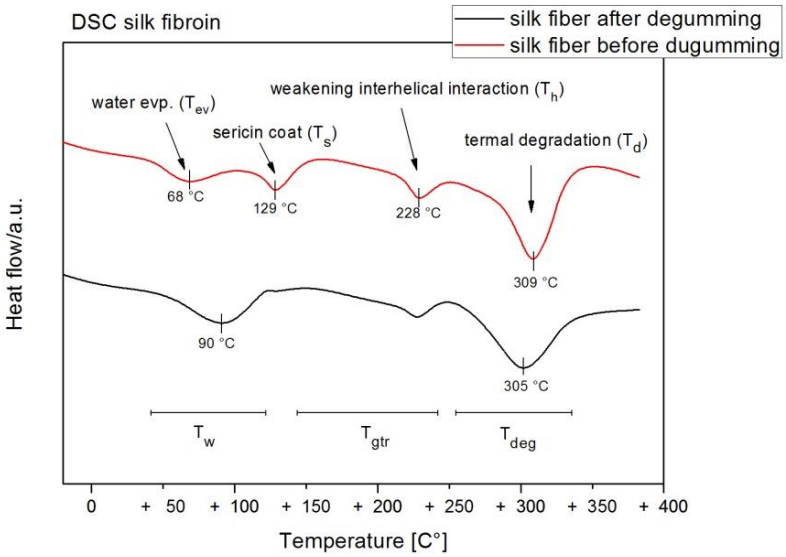

Figure 4.23. Comparison of DSC curve between non-degummed and degummed neat fiber. T_w is the region in which bounded water evaporation occurs, T_{gtr} region is where glass transition and weakening of inter-helical interaction occur, whereas in T_{deg} region degradation occurs.

indicated as T_{ev}). This significant peak is mainly affected from sericin coat gum and its capacity to moisture retention; this protective layer controls humidity absorption and in nature, this advantage could help silk cocoon to exchange water molecules easily with different atmospheres, while the fibers are rigid enough to protect the wild silkworm cocoons in an extreme wild environment. Water evaporation peak of degummed sample is probably larger because after sericin coat removal the fiber matrix absorbs more humidity from the environment so that the water amount inside the matrix is larger.

The second peak is present only on the non–degummed sample at around 130°C and it is clearly related to the degradation of the sericin gum coat; if we note in the degummed sample curve this peak is not completely disappeared but it is very small, almost imperceptible. This means that a very small fraction of sericin is still present in the degummed sample.

In the range of 150 to 250 °C (T_{gtr} region) glass transition and weakening of inter-helical interaction occur: DSC curve of non-degummed silk exhibits a relatively small endothermic peak at 228°C (T_h) before degradation, and it probably corresponds to the weakening of inter-helical interactions. This will be more clear subsequently by watching DSC of doped sample in which the treatment will clearly affect the dimension of this peak. The only difference in the neat fiber after degumming curve is that this peak is slightly smaller respect to the former one

and it is due to the degumming treatment process that enabled chain mobility breaking a small percentage of secondary bonds.

After the glass transition, all samples thermally degraded in the range of 250 to 350 °C (T_{deg} region) with the degradation temperature indicated with T_d. This peak is largely affected by the secondary structure and the crystallinity of the silk fibroin. We can clearly state that the most affecting parameter is the β-sheet content; larger is the amount (higher is the crystallinity) harder is the thermally induced degradation, and the peak moves to higher temperature value. Also the microporosity, the lack of secondary bond, the presence of sericin coat can affect this peak.

In the graph of neat silk this peak is shifted of only 4 °C and this indicates that the structure has not been changed so much after degumming; however we can justify this shift with the reasons discussed before: higher amount of secondary bonds in non-degummed sample but the same crystallinity. The sericin coat doesn't help non-degummed fiber stability because its degradation occurred at lower temperature.

In this work a particular attention was given to glass transition: T_g is the temperature at which amorphous or semi-crystalline polymers are converted from a brittle, glasslike form to a rubbery, flexible form.

This is not a true phase transition but one that involves a change in the local degrees of freedom. Above the glass transition temperature certain segmental motions of the polymer are comparatively unhindered by the interaction with neighboring chains. Below the glass transition temperature, such motions are hindered greatly, and the relaxation times associated with such hindered motions are usually long compared to the duration of the experiment.

The operative definition of glass transition temperature is that at this temperature, or within a few degrees, the specific heat, the coefficient of thermal expansion, the free volume, and the dielectric constant (in the case of a polar polymer) all change rapidly.

Since the mechanical behavior of polymers changes markedly at the glass transition temperature, it is an important characteristic of every polymer. In the DSC experiment, T_g is manifested by a change in the base line, indicating a change in the heat capacity of the polymer; no enthalpy is associated with such transition (for which reason it is also called a second order transition); therefore, the effect in a DSC curve is difficult to be detected and very sensitive instruments are required.

In our DSC curve we tried to detect T_g even if for certain aspects was complicated to extract an accurate temperature value. We started from the assumption that glass transition occur obliviously prior to thermal degradation and prior to weakening of secondary bonds among long chains.
Our detection procedure is based on the work from David Norman (D. Norman et al., 2011) and Samantha Mazzi (S. Mazzi et al., 2014) and a practical explanation is presented in the next section (Figure 4.25).

4.5.3 I_2 TREATED SILK FIBER DSC CURVE

Iodine treatment largely affected the structure of silk matrix and this is visible by the DSC curve, comparing neat and lightly/heavily doped silk fiber. We can see firstly (Figure 4.25) that the water evaporation temperature is slightly shifted to higher T and the endothermic peak of heavily doped silk fiber is a little larger with respect to the lightly doped one. This could be attributed to a more water retention after the treatment due to slightly higher percentage of amorphous phase (it is more likely that water from humidity percolate into amorphous region instead of hydrophobic β-sheets); the content of humidity within the silk matrix depend only on the amorphous phase.
The peak related to the weakening of inter-helical interaction is still present in the lightly doped samples but disappears in the heavily doped one and this indicates lack of high amount of secondary bonds in the second case.
Figure 4.25 (right) shows how to extract T_g value based on the baseline change: it is however complicated to apply the same procedure for neat silk sample whose T_g was determined in the range of 180-190 °C (higher respect to data in literature, see section 4.5.1).
By the fact that part of the secondary bonds were suppressed by the iodine ions or molecules, as well as some of β-sheets were transformed, is understandable that in the heavily doped silk fiber glass transition occur at lower temperature: chains mobility was increased and this helps the matrix to turn on rubber-like state with considerably less amount of energy, so at lower temperature. Also for lightly iodine doped sample T_g was found at lower temperature as in the previous case

Degradation peak is shifted to lower temperature value only for heaviliy doped sample: degradation itself starts earlier and while T_d of neat and lightly sample is 305°C, for heavily doped it is shifted to 287°C. This result is in agreement with the previous results (structural and mechanic) that suggested lower percentage of crystalline phase.

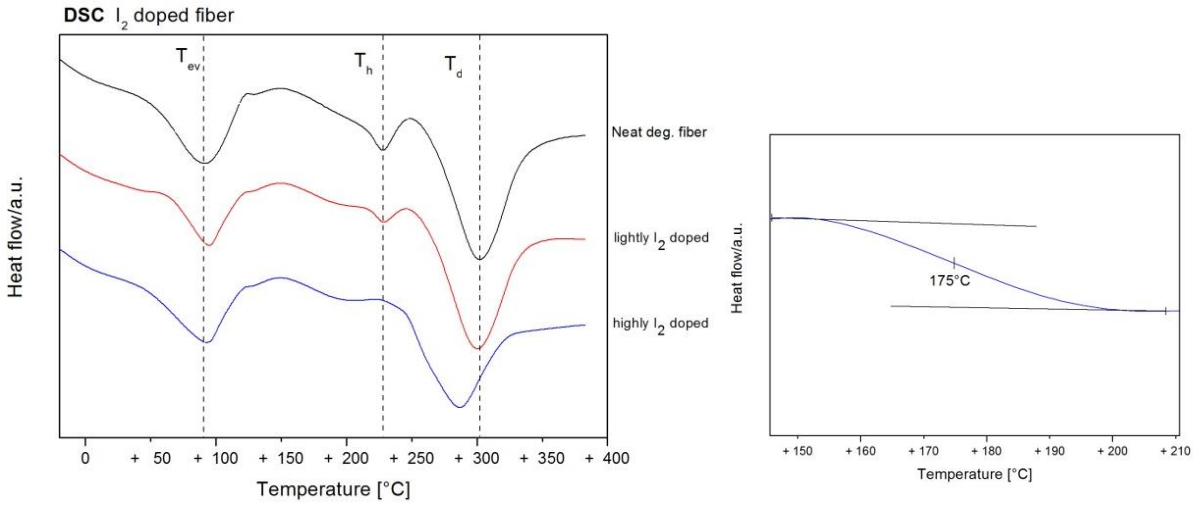

Figure 4.25. DSC curves for iodinated silk fibers (left). Identification of Tg (175°C) for heavily iodinated silk sample (right).

4.5.4 $CaCl_2$ TREATED SILK FIBER DSC CURVE

Figure 4.26 shows DSC curves for $CaCl_2$ doped silk samples; dot vertical lines refer to T_{ev}, T_h and T_d of neat sample.

Water evaporation peak is shifted toward increasingly higher temperature values as doping concentration increase and it is a clear sign of higher water retention in the microporous structure of salt doped silk; moreover the degradation of hydrophobic β-sheets after treatment on behalf of random coil amorphous structure further promotes this retention.

Passing from neat to highly doped sample we note the disappearance of the endothermic peak at 228 °C attributed to weakening of inter-helical secondary bonds and this is in agreement to

the considerations regarding calcium ions that coordinate with polar group of polymer blackbone, destroyng part of secondary bonds.

Degradation peak is increasingly shifted toward lower temperature and it is increasingly smaller as indication of less amount of crystalline phase.

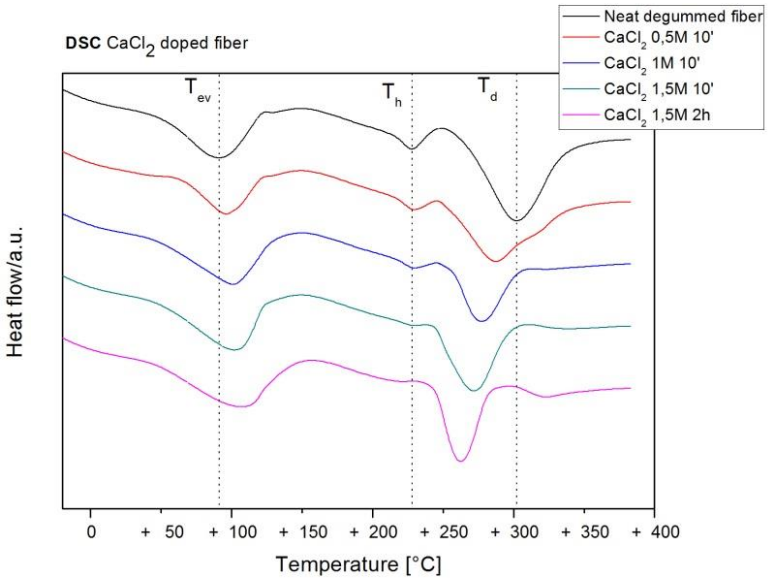

Figure 4.26. DSC curves of $CaCl_2$ doped silk fibers at different doping concentration; vertical line are related to founded temperatures of neat degummed silk fiber.

Unfortunately it is very difficult to find graphically an accurate value of glass transition temperature in this case: only for $CaCl_2$ 1,5M 2h we found T_g=184,8 ° C as shown in Figure 4.27. This is a strange result be based on the consideration made on ions effect in the silk matrix; we expected the the coordination of ions with lateral group of long-chain and the suppression of secondary bonds would help chain flow and consequently glass transition would occur at lower T as in the previous case of iodine; in general we can not assure accurate comparison with neat sample due to the difficult detection of T_g from the graph.

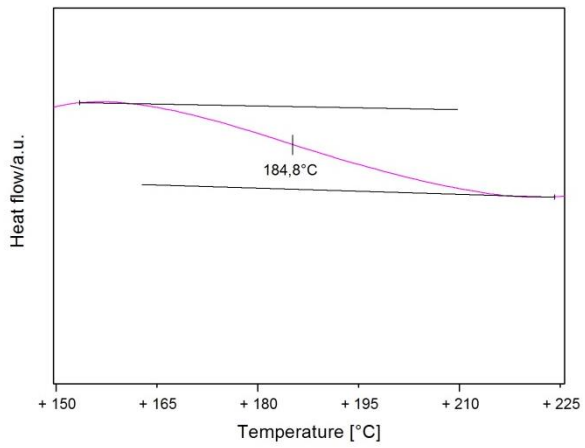

Figure 4.27: Identification of Tg (184,8 °C) for $CaCl_2$ 1,5M 2h silk sample.

4.5.5 KBr TREATED SILK FIBER DSC CURVE

DSC Kbr treated curves present some similarities with the $CaCl_2$ ones: peak of water retention shifted toward higher temperature values but not so well marked as in the previous case; in fact we stated that microporous structure in this case is less predominant so the water retention is lower; we have also noted that in the case of KBr 1,5M 2h sample this peak remains at the same temperature as in the neat case and it is present a second small peak at around 130°C; for some reason bound water found some difficulties to evaporate at lower temperature and a second evaporation peak indicates complete evaporation.

Passing from neat to highly doped sample we note againd the disappearance of the endothermic peak at 228 °C attributed to weakening of inter-helical secondary bonnds.

As expected also the degradation peak shifted to lower temperature as indication of less crystalline content but in this case are reached higher temperature respect to calcium salt doped samples.

All the results regarding KBr treated samples are in good accordance with previous consideration; we can say that KBr for some aspect has similar but less marked effects respect to $CaCl_2$ on silk structure

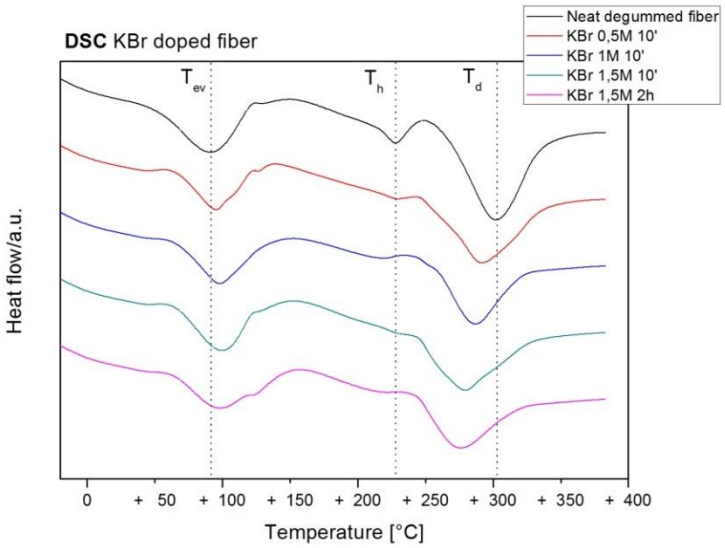

Figure 4.27. DSC curves of KBr doped silk fibers at different doping concentration; vertical line are related to founded temperatures of neat degummed silk fiber.

4.5.6 DISCUSSION

Despite the difficulties in the detection of the glass transition temperature, thermal analysis gave us important evidences useful to confirm the previous considerations on the structure of the silk and its modification.

The change of the peak of thermal degradation in terms of temperature revealed that the content of the crystalline phase is less in the samples treated with iodine and salts, simply because the degradation of the amorphous phase takes place more easily in terms of thermal energy, and then at lower temperature.

Two other peaks relating respectively to the retention of water and the weakening of secondary bonds undergone substantial changes after treatment with iodine and salts, particularly the greater retention of water by the samples treated with salts has further confirmed the presence of the microporous structure suggested previously.

Further efforts should be made to optimize the procedure aimed at identicare the glass transition temperature, simply for the fact that the DSC analysis, maybe combined TGA analysis has proved to be a good tool for characterization of polymers.

REFERENCES

Arrondo J.L, Muga A, Castresana J, Goni FM. Quantitative studies of the structure of proteins in solution by Fourier-transform infrared spectroscopy. Prog Biophys Mol Biol. 1993;59(1):23-56.

Asakura T., Yao J. 13C CP/MAS NMR study on structural heterogeneity in Bombyx mori silk fiber and their generation by stretching. Protein Science 2002; 11(11): 2706– 2713.

Askarieh G., Hedhammar M., Nordling K., Saenz A., Casals C., Rising A., Johansson J., Knight S D. Self-assembly of spider silk proteins is controlled by a pH-sensitive relay. Nature 2010; 465(13): 236–238.

Bragg, W.H.; Bragg, W.L. (1913). "The Reflexion of X-rays by Crystals". Proc R. Soc. Lond. A 88 (605): 428–38

Brindan Tulachan, Sunil Kumar Meena, Ratan Kumar Rai, Chandrakant Mallick, Tejas Sanjeev Kusurkar, Arun Kumar Teotia, Niroj Kumar Sethy, Kalpana Bhargava, Shantanu Bhattacharya, Ashok Kumar, Raj Kishore Sharma, Neeraj Sinha, Sushil Kumar Singh & Mainak Das. Electricity from the Silk Cocoon Membrane. Scientific Reports 4, Article number: 5434. Sept. 2013

Chaoyang Jiang, Xianyan Wang, Ray Gunawidjaja, Yen-Hsi Lin, Maneesh K. Gupta, David L. Kaplan, Rajesh R. Naik, Vladimir V. Tsukruk. Mechanical Properties of Robust Ultrathin Silk Fibroin Film. Adv. Funct. Mater. 2007, 17, 2229–2237

David Norman, Peng Ye. Detecting Weak Glass Transition(Tg) in Polymers by HyperDSC. Thermal Analysis, Application note from PerkinElmer, Inc. Shelton, CT 06484 USA (2011)

David T. Grubb and Lynn W. Jelinski. Fiber Morphology of Spider Silk: The Effects of Tensile Deformation. Macromolecules 1997, 30, 2860-2867

Debenedetti, P. G.; Stillinger (2001). "Supercooled liquids and the glass transition". Nature 410 (6825): 259–267.

Dekker M. In: Porter D. (ed.) Group interaction modeling of polymer properties. New York. 1995. P499.

Drummy L F., Farmer B L., Naik R R. Correlation of the β-sheet crystal size in silk fibers with the protein amino acid sequence. Soft Matter 2007; 3(7): 877–882.

E. Steven, et al. Physical Characterization of Functionalized Spider Silk: Electronic and Sensing Properties. Sci. Technol. Adv. Mater 12, 055002 (2011).

Hao Zhang, Ling-ling Li, Fang-yin Dai, Hao-hao Zhang, Bing Ni, Wei Zhou, Xia Yang and Yu-zhang Wu. Preparation and characterization of silk fibroin as a biomaterial with potential for drug delivery. Journal of Translational Medicine 2012, 10:117

Hiroyuki Saitoha, Ken-ichi Ohshimaa, Kozo Tsubouchib, Yoko Takasub, Hiromi Yamadad. X-ray structural study of noncrystalline regenerated Bombyx mori silk fibroin. International Journal of Biological Macromolecules 34 (2004) 259–265

J.O. Warwicker. Comparative studies of fibroins V. X-ray examination of chemically resistant fractions of some silk fibroins. Biochimica et Biophysica Acta Volume 52, Issue 2, 16 September 1961, Pages 319–328

Jarvis J.A.J., Kilbourn B.T., Owston P.G. (1970). "A re-determination of the crystal and molecular structure of Zeise's salt, $KPtCl_3.C_2H_4.H_2O$. A correction". Acta Crystallographica B 26 (6): 876.

Jianxin He, Guoxin Jia, Shizhong Cui Shanyuan Wang, Yaying Gao. Chemical Modification of Bombyx mori Silk with Calcium-Salt Treatment and Subsequent Glycerin Triglycidyl Ether Crosslinking. Journal ofAppliedPolymer Science,Vol. 118, 3260–3268 (2010)

K. Bakhshi, Avneet Kaur, Vinita Arora. Molecular engineering of novel low bang gap conducting polymers. Indian journal of Chemistry. Vol 51A, Jan-Feb 2012, pp 57-68

Kaplan D.; Adams W W., Farmer B., Viney C., editors. Silk polymers: materials science and biotechnology. American Chemical Society Symposium Series 1994.

Lotz, B. & Keith, H. D. Crystal structure of poly(L-Ala-Gly)II. A model for silk. I. (1971) J. Mol. Biol. 61, 201–215.

M. G. Dobb, R. D. B. Fraser, and T. P. Macrae. The fine structure of silk fibroin. The journal of cell biology - volume 3, 1967

Mahiar Hamedi, Robert Forchheimer and Olle Ingana. Towards woven logic from organic electronic fibres. Published online in Nature materials Vol 6 May 2007.

Michael Antony Johnson, thesis dissertation of title: Characterization, Processing and Modeling of Silk and Silk-like Polymers. University of Michigan 1993

Mingzhong Li, Shenzhou Lu, Zhengyu Wu. Study on porous Silk fibroin materials. Fine structure of freeze dried silk fibroin. Journal of Applied Science, Vol. 79, 2185-2191 (2001)

N. Agarwal, D. A. Hoagland, R. J. Farris. 1997 Effect of Moisture Absorption on the Thermal Properties of Bombyx mori Silk Fibroin Films. Appl Polym Sci 63: 401–410, 1997

N. Du, X. -Y. Liu, J. Narayanan, L. Li, M. L. M. Lim, and D. Li. Bioprospecting finds the toughest biological material: extraordinary silk from a giant riverine orb spider. Biol. J. 91,4528(2006).

Neil W. Ashcroft and N. David Mermin, Solid State Physics (Harcourt: New York, 1976).

P. M. Cunniff , S. A. Fossey, M. A. Auerbach, J. W. Song, D. L. Kaplan, W. W. Adams, R. K. Eby, D. Mahoney and D. L. Vezie, Mechanical and thermal properties of dragline silk from the spider Nephila clavipes. Polym. Adv. Technol. 5, 401(1994).

Porter D., Vollrath F., Shao Z. Predicting the mechanical properties of spider silk as a model nanostructured polymer. The European Physical Journal E 2005; 16(2): 196-206

Qiang Lua, Xiao Hua, Xiaoqin Wanga, Jonathan A. Klugea, Shenzhou Lua,b, Peggy Cebec, and David L. Kaplan. Water-Insoluble Silk Films with Silk I Structure. Acta Biomater. 2010 April ; 6(4): 1380–1387

Rising A., Hjälm G., Engström W., Johansson J. N-terminal nonrepetitive domain common to dragline, flagelliform, and cylindriform spider silk proteins. Biomacromolecules 2006; 7(11): 3120–3124

Rising A., Hjälm G., Engström W., Johansson J. N-terminal nonrepetitive domain common to dragline, flagelliform, and cylindriform spider silk proteins. Biomacromolecules 2006; 7(11): 3120–3124.

Romero Isabella S., "Silk fibroin-based conducting polymer composite electrodes and their use as electromechanical actuators" (2013). WWU Masters Thesis Collection. Paper 280.

Rousseau M E., Lefèvre T., Beaulieu L., Asakura L., Pézolet M. Study of protein con-formation and orientation in silkworm and spider silk fibers using Raman microspectroscopy. Biomacromolecules 2004; 5(6): 2247–2257.

Samantha Mazzi, Emma Zulker, Justin Buchicchio, Breijha Anderson, Xiao Hu. Comparative thermal analysis of Eri, Mori, Muga, and Tussar silk cocoons and fibroin fibers. J Therm. Anal. Calorim. (2014) 116:1337–1343

Serge Rebouillat, Michael E.G. Lyons. Measuring the Electrical Conductivity of Single Fibres. Int. J. Electrochem. Sci., 6 (2011) 5731 - 5740

Shen Y., Johnson M A., Martin D C. Microstructural characterization of Bombyx mori silk fibers. Macromolecules 1998; 31(25): 8857–8864.

Simmons A H., Michal C A., Jelinski L W. Molecular orientation and two-component nature of the crystalline fraction of spider dragline silk. Science 1996; 271(5245): 84–87.

Simmons A., Ray E., Jelinski L. W. Solid-state 13C NMR of Nephila clavipes dragline silk establishes structure and identity of crystalline regions. Macromolecules 1994; 27(18): 5235–5237.

Sponner A., Vater W., Rommerskirch W., Vollrath F., Unger E., Grosse F., Weisshart K. The conserved C-termini contribute to the properties of spider silk fibroins. Biochemical and Biophysical Research Communications 2005; 338(2): 897–902.

Standard Specification for Glass Fiber Strands. Active Standard ASTM D578 / D578M. Book of Standards Volume: 07.01.

Steven Eden, Physical Properties Of Organic And Biomaterials: Fundamentals And Applications (2012). Electronic Theses, Treatises and Dissertations. Paper 5443.

Takahashi Y. Crystal structure of silk of Bombyx mori. In: Kaplan D.; Adams W W., Farmer B., Viney C. (eds.) Silk polymers: materials science and biotechnology. American Chemical Society Symposium Series 1994. 544: P168–175.

Termonia Y. Molecular modeling of spider silk elasticity. Macromolecules 1994; 27(25): 7378–7381.

Tetsuo Asakura, Yasumoto Nakazawa, Erika Ohnishi, and Fumika Moro. Evidence from ^{13}C solid-state NMR spectroscopy for a lamella structure in an alanine–glycine copolypeptide: A model for the crystalline domain of Bombyx mori silk fiber.Protein Sci. 2005 Oct; 14(10): 2654–2657.

Tuna Yucel , Peggy Cebe , and David L. Kaplan. Structural Origins of Silk Piezoelectricity. Adv. Funct. Mater. 2011, XX, 1–7

van Beek J D., Hess S., Vollrath F., Meier B H. The molecular structure of spider dragline silk: Folding and orientation of the protein backbone. Proceedings of the National Academy of Science of the United States of America 2002; 99(16): 10266–10271.

Wu Xiang “physical mechanism of silk strength and design of ultra-strong silk”. Thesis submitted by National University of Singapore (NUS), 2010.

Xiangyu Huang, Suna Fan, Alhadi Ibrahim Mohammed Altayp, Yaopeng Zhang, Huili Shao, Xuechao Hu, Minkai Xie, and Yuemin Xu. Tunable Structures and Properties of Electrospun Regenerated Silk Fibroin Mats Annealed in Water Vapor at Different Times and Temperatures. Journal of Nanomaterials Volume 2014, Article ID 682563.

Xiao Hua, David Kaplan , Peggy Cebea. Effect of water on the thermal properties of silk fibroin. Thermochimica Acta 461 (2007) 137–144

Xin Chen. David P. Knight, Zhengzhong Shao, and Fritz Vollrath. Conformation Transition in Silk Protein Films Monitored by Time-Resolved Fourier Transform Infrared Spectroscopy: Effect of Potassium Ions on Nephila Spidroin. Biochemistry 2002, 41, 14944-14950

Yasuo Saegusa, Shigenoa Kamura, Yoshio Yamaguchi. Physical Properties and Structure of Silk. Glass Transition Temperature of Wild Silk Fibroins. Journal of Applied Polymer Science, Vol. 31, 955-956 (1986).

Youyi Xia, Yun Lu. Fabrication and properties of conductive conjugated polymers/silk fibroin composite fibers. Journal of Applied Polymer Science 08/2014; 132(4).

Yu Shen , Michael A. Johnson , and David C. Martin. Microstructural Characterization of Bombyx mori Silk Fibers. Macromolecules, 1998, 31 (25), pp 8857–8864. November 12, 1998

Zheng S., Li G., Yao W., Yu T. Raman spectroscopic investigation of the denaturation process of silk fibroin. Applied Spectroscopy 1989; 43(7): 1269–1272.

Zhou C Z., Confalonieri F., Jacquet M., Perasso R., Li Z G., Janin J. Silk fibroin: structural implications of a remarkable amino acid sequence. Proteins: Structure, Function, and Genetics 2001; 44(2): 119–122.

Zhou C Z., Confalonieri F., Medina N., Zivanovic Y., Esnault C., Yang T., Jacquet M., Janin J., Duguet M., Perasso R., Li Z G. Fine organization of Bombyx mori fibroin heavy chain gene. Nucleic Acid Research 2000; 28(12): 2413–2419.

Chapter 5: REGENERATED SILK FIBROIN BIOFILM

5.1 INTRODUCTION

Iodine is one of five non-metallic elements called halogens. Halogens readily share electrons in covalent bonds with other atoms to complete an octet of electrons in their valence shell. Of the many modification techniques for polymers, iodine treatment causes antibacterial properties (M. M. R. Khan, 2006). For example, iodinated cadexomer, a polysaccharide including iodine, is applied to a pharmaceutical material as a wound healing medicine, due to its high antibacterial activity (H. Akiyama, 2014). Iodine molecules can form complexes with many kinds of polymers such as nylon 6 (A. Kawaguchi, 1992) starch (A. Cesaro, 2002), poly(vinyl alcohol) (J. H. Yeum, 2004), and chitosan (H. Yajima, 2004), etc.

M. M. R. Khan previously reported (M. M. R. Khan, 2006) that iodine treatment has greatly influenced the molecular structure and properties of different kind of both silkworm and spider silk fibroin; in particular the absorption of polyiodide ions being almost limited to the amorphous region for SF. The XRD measurements showed an ambiguous crystalline pattern of silk II and a decrease in the degree of crystallite orientation after the iodine treatment. Moreover the iodine components chiefly enter the amorphous region, and the amorphous chains are relaxed; this introduces the decrease in the crystallite orientation. In addition, a new reflection has been observed by iodination in the meridional direction, and this may show a mesophase consisting of a bundle of β-conformation chains.

In the next sections we present a simply method to obtain a iodinated SF biofilm and we will perform, only partially, structural secondary structure analysis with XRD. Regenerated silk fibroin implies degumming, dissolution process and dyalisis with a proper membrane of cellulose; evaporation technique using UV lamp will be used to obtain thin biofilm after solution casting into glass plate; finally, potential application not only in the bioengineering field will be proposed.

5.2 SILK FILK PREPARATION

5.2.1 DEGUMMING

Respect to fibers, in this case slightly different degumming process was used to prepare silk: silk cocoons were added in 0.1M sodium carbonate Na_2CO_3 solution 1g/100ml w/v and stirred on the hot plate at 75°C. Degumming process carried out through three sessions of time, three hours per each session, and then the produced degummed silk is washed with pure water. Finally, degummed silk fibroin dried for several hours in laboratory at room temperature

Figure 5.1 Silk immediately after degumming (left), dried silk (right)

5.2.2 DISSOLUTION PROCESS

The dissolution process used for dissolving the silk fibroin to have an aqueous form of silk fibroin, the benefit of this process is to break the long polypeptide chains into shorter chains lengths. This process prepared by blending silk fibroin with n_{C2H5OH}:n_{H2O}:n_{CaCl2} (2:8:1) molar ratio at 75°C with continuous stirring until the complete dissolution. After that the electrolyte solution with silk fibroin protein has been obtained.

5.2.3 DYALISIS

After dissolution process which an aqueous electrolyte solution produced with silk fibroin, the dialysis process started. The need of dialyses process was to remove the ions to get pure silk fibroin solution. The dialyses process done by pouring the aqueous electrolyte solution into a carboxymethyl cellulose semipermeable membrane tube (Sigma Aldrich) and putting the membrane in the large beaker 5 liters in volume filled with distilled water. According to the membrane properties the ions will diffuse through the membrane to the water. This process repeated six times with different periods of time (1, 3, 6, 9, 12 hours) with continuous stirring, after that the pure aqueous silk fibroin formation obtained, now the silk fibroin ready to using it in the biofilm preparations and other applications.

Figure 5.2 Dialysis of the aqueous silk fibroin with distilled water.

5.2.4 BLEND AND BIOFILM PREPARATION

Firstly, a 1.42 M iodine-potassium iodide (I_2-KI) aqueous solution was prepared in a tube and kept for about 13 h at room temperature with gentle stirring to dissolve iodine into potassium iodide properly.

The solutions of SF and I_2-KI (w/w 90/10) were mixed for 15 minutes with stirring at 80° C. This solution was casted on glass plates at room temperature for 5 days. After drying, these biofilms were carefully removed from glass plates, and were stored in a desiccator for further use. For comparison was also prepared a neat silk film with the same procedure.

By blending 3ml of silk fibroin solution with the cross linker $C_7N_{10}H_2O_2$ (*N*,*N*′ Methylenebis(acrylamide), linear Formula $(H_2C{=}CHCONH)_2CH_2$ by Sigma Aldrich)

the blended solution were poured over a piece of glass and was deposited under UV wave in dark chamber and UV irradiation started. The process has been continuing until the biofilm formed.

5.3 SILK BIOFILM STRUCTURAL ANALYSIS

After drying, free standing iodine treated biofilm was accurately powdered in order to perform XRD analysis and making some comparison with a neat silk film (SF/I_2-KI w/w 100/0). Figure 5.3 shows comparison between neat and iodinated XRD profile: We immediately note a substantial difference respect what happened with the I_2 treated fiber; here Silk II peaks increased so much and seems that the main peak at 2θ=19,91° attributed to Silk I highly decrease in intensity. This was unpredictable after XRD analysis for fibers, but the reason should be sought in the silk fibroin regeneration process.

Several different solvent system was commonly used to dissolve Bombyx Mori to prepare regenerated silk membrane and fibers and different behavior have been noticed in the modification of structure; formation and spatial organization of β-sheet after dissolution and dyalisis is influenced by many factor, like temperature, solvent, humidity, etc. Obviously iodine influence has a great importance in terms of SF forming β-sheet and molecular motion.

Probably β-sheet formation in iodinated treated film has to be attributed to ability of absorbed polyiodide ions I_3^- and I_5^- to weaken hydrogen bonds between long peptide chains in

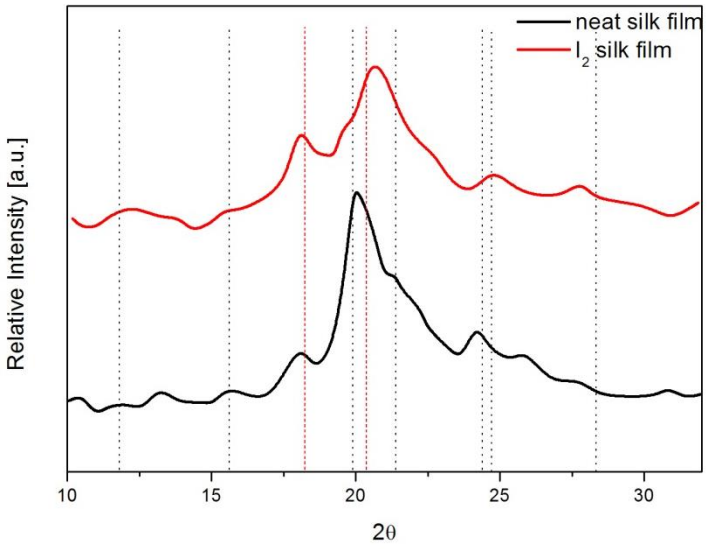

Figure 5.3: Neat silk film XRD profile (black line) and iodinated silk film one (red line). Dot vertical lines refer to Silk II structure diffraction angles.

order to facilitate molecular motion and antiparallel β-sheets formation at the expense to α-helix; after crystallite formation probably iodine component promotes intermolecular crosslinking and inhibit melt flow.

Thus regeneration of silk fibroin with iodine seems to promote crystalline Silk II phase respect to Silk I, which instead is more present into neat sample, and this evidence could be exploited to increase mechanical properties for example; on the contrary we can imagine that there are not necessary conditions for an increase in the conductivity due to scarce mobility of ions in this high crystalline film.

5.4 POTENTIAL APPLICATION

Silk thin film interest is growing due to large possibility of structure modification and possible applications achievable. Recent interest in microelectronics has been gained by silk film even though studies in this direction are yet scarce.

Up to now, most used strategy to make silk conductive is to blend it with conductive polymers or create composite with conductive material for example a flexible graphene silk composite film electrodes was created by B. Liang (B. Liang, et al., 2014) recently.

For this purpose it is necessary to control biocompatibility in relation with the added material especially when the silk film would be used for bioresorvable or epidermic devices; in this optic a iodine modified film is still biocompatible and will present a certain value of conductivity, at least much higher (not compared with conductive polymers) respect to neat silk;

REFERENCES

Cesàro and D. A. Brant. Biological Applications of Atomic Force Microscopy. Updated on January 14, 2003 Biopolymers, 16, 983 (1997).

H. Akiyama, T. Oono, M. Saito, and K. Iwatsuki, J. Assessment of cadexomer iodine against Staphylococcus aureus biofilm in vivo and in vitro using confocal laser scanning microscopy. The Journal of Dermatology, Volume 31, Issue 7, pages 529–534, July 2004

H. Yajima, M. Morita, M. Hashimoto, H. Sashiwa, T. Complex Formation of Chitosan with Iodine and Its Structure and Spectroscopic Properties—Molecular Assembly and Thermal Hysteresis Behavior. Kikuchi, and T. Ishii, Int. J. Thermophys., 22, 1265 (2001).

J. H. Yeum, J. W. Kwak, S. S. Han, S. S. Kim, B. C. Ji, S. K. Noh, and W. S. Lyoo, J. Electrospinning fabrication and characterization of poly(vinyl alcohol)/waterborne polyurethane nanofiber membranes in aqueous solution Appl. Polym. Sci., 94, 1435 (2004).

Kawaguchi. Structure of nylon 6/iodine complex. 5: variation of intercalation in complexes induced by humidification Polymer, 33, 3981 (1992). Dermatol., 31, 529 (2004).

M. M. R. Khan, Y. Gotoh, M. Miura, H. Morikawa, and M. Nagura, J. Influence of an iodine treatment on the structure and physical properties of Bombyx mori silk fibroin fiber Polym. Sci. Part-B: Polym. Phys., 44, 3418 (2006).

Md. Majibur Rahman Khan, Yasuo Gotoh, Hideaki Morikawa, and Mikihiko Miura. Structural and Physical Properties of Antheraea pernyi Silk Fibroin Fiber Treated with I2-KI Aqueous Solution. Fibers and Polymers 2006, Vol.7, No.4, 333-338 333

Chapter 6: CONCLUSION AND FUTURE DEVELOPMENT

We have seen how it is possible to change structure and properties of silk with different doping agent like iodine, $CaCl_2$ and KBr and we have investigated and proposed possible interaction between ions and silk matrix.

We started from a close look to Bombyx mori silk structure with a particular attention to secondary structure and possible conformation. We have proposed three kind of doping with the intent to understand and possibly tailor structural and electrical properties in order to exploit different forms of silk in various unconventional field for silk-based material like microelectronics, optics or stretchable/flexible electronic.

The three kind of doping we studied, have had in some ways a similar effect on the secondary structure of silk fibers: iodine ions have had the main effect of infiltrate between β-sheet and destroy the secondary bonds between them; a considerable amount of these crystallites have been degraded and transformed in random coil or α-helix with a substantial effect on the mechanical and electrical properties of the fibers themselves. Fibers treated with iodine are more flexible and have lower values of breaking stress and higher values of breaking strain; the structural analysis by FTIR and XRD revealed in fact a lower crystalline component in terms of quantity and size of the crystallites, which perform the function of providing stiffness and strength to the fiber under tensile force; conductivity resulted increased thanks to the absence of the same crystallites which prevent the diffusion of the charge carriers. Iodine-water complexes have been formed into the matrix and a considerable amount of ionic current have been observed under RH and T increase. Thermal analysis with DSC had further confirm considerations about crystalline fraction, showing anticipated (lower T) degradation peaks respect the non-doped fiber.

Fibers treated with KBr and $CaCl_2$ show a microporous structure, as confirmed by the weight loss as a result of doping: also in this case part of the crystallites are degraded and transformed into amorphous structure; probably K^+ and Ca^+ ions coordinate with polar lateral groups of the macro-molecules, destroying the secondary bonds between them and sheets. Mechanical and electrical properties have been modified consequently and seemed microporous structure mainly affect the ability of support high stress value, especially in the case of $CaCl_2$ treated samples; moreover the introduction of calcium and other ions helped to enhance conductivity to higher values but not as higher respect to iodine treated sample.

Finally it was proposed a simple method to form a thin film starting from a KI/I_2 and SF blend solution and was studied secondary structure by XRD: the effect of iodine was to promote the crystallite formation acting as a crosslinker during long chain organization.

Studies on silk started many years ago and have been achieved today considerable. Some applications of silk as biomaterial were widely studied and showed excellent performance: to name a few, two-dimensional films and coatings, micro-patterning and microfluidics, three-dimensional cellular substrata, implant applications, delivery vehicles, scaffolds etc. In addition to the incredible applications in tissue engineering and in biomedical field is thought to expand the use of this fantastic material to other fields such as photonics, optics and microelectronics.

Until now there have been many studies concerning the functionalization of silk, but have never been focused to use it as a conductive element, for example in the field of sensors or smart textile; some studies demonstrated the use of thin films of silk as gate dielectric in OFET while some researchers thought of developing silk-based electrodes; these and a few other examples do not exhaust the prospects for the use of this material, consequently the development and implementation of electronic-based silk is desirable and highly auspicable.